# Adjoint Modelling for Assimilation and Diagnosis on Climate Timescales

## Dissertation

zur Erlangung des Doktorgrades der Naturwissenschaften
im Department Geowissenschaften
der Universität Hamburg

vorgelegt von
Simon Blessing
aus
Koblenz

Hamburg
2008

Als Dissertation angenommen vom Department Geowissenschaften der Universität Hamburg

Auf Grund der Gutachten von .....
und .....

Hamburg, den .....
(Datum der vorläufigen Bescheinigung)

Prof. Dr. Kay-Christian Emeis
Leiter des Department Geowissenschaften

# Zusammenfassung

Die Erforschung des Klimawandels erfordert sowohl zuverlässige Modelle, als auch ein prinzipielles Verständnis der atmosphärischen Dynamik und ihrer Interaktion mit anderen Komponenten des Klimasystems. Beide Aspekte hängen über Sensitivitäten zusammen. Dieses Sensitivitäten bezüglich Rand-, Anfangs- und Parameterwerten lassen sich auf kurzen Zeitskalen mit adjungierten Modellen effizient bestimmen. Für die Anpassung gekoppelter Klimamodelle an ein vorgegebenes Klima, sei es zur Verifikation oder als Szenario, und für das erfassen klimarelevanter dynamischer Zusammenhänge, müssen Sensitivitäten bestimmt werden, die über einen bestimmte Wettersituation hinaus, d.h. auf längeren Zeitskalen, Gültigkeit besitzen.

In dieser Arbeit wird das Potential der adjungierten Methode für Anwendungen in der Klimamodellierung untersucht. Dies erfolgt zum einen im Hinblick auf die Entwicklung eines gekoppelten Assimilationssystems, zum anderen mit dem Ziel, Sensitivitäten in der Diagnostik zum Verständnis der dynamischen Abhängigkeiten innerhalb und zwischen den Klimasubsystemen einzusetzen.

Es wird gezeigt, daß die adjungierten Gradienten in der atmosphärischen Komponente eines solchen Systems, bei der gewählten relativ groben Modellauflösung von ca. 5°, geeignet sind, für Zeiträume jenseits von 30 Tagen die Sensitivitäten zu beschreiben. In einem Anwendungsbeispiel wird unter Einsatz einer Gradienten-Mittelungsmethode ein komplexes Parameterfeld bestimmt, so daß das Modell ein vorgegebenes Klima reproduziert.

Für das zweite Entwicklungsziel wird das adjungierte Atmosphärenmodell zur Bestimmung des optimalen Antriebs für den beobachteten Trend auf der nördlichen Halbkugel im Winter der NCEP[1]-Reanalysedaten in der zweiten Hälfte des 20. Jahrhunderts verwendet. Dabei dient das adjungierte Modell allein zur Diagnostik; die Dynamik des untersuchten Klimas wird vollständig von den Reanalysedaten vorgegeben. Auf diese Weise wird bei der Diagnose dynamischer Wirkungsketten die Daten um das dynamische Vorwissen aus den adjungierten Modellgleichungen ergänzt. Das hierzu entwickelte Programmpaket deckt zahlreiche Bedürfnisse für die Berechnung von Sensitivitäten durch weitgehend flexible Wahl der Zielfunktion durch Projektion auf verschiedene atmosphärischer Felder ab. Die Bestimmung von Sensitivitäten bezüglich isentroper potentieller Vorticity stellt dabei den aktuellen Entwicklungshöhepunkt dar.

Damit sind zum einen erste Schritte in Richtung eines anvisierten gekoppelten Ozean-Atmosphäre Assimilationssystems für Klimastudien getan, mit dem es möglich werden könnte z.B. Paläodaten zu assimilieren. Zum anderen ist die Anwendbarkeit von adjungierten Modellen für die Aufklärung klimarelevanter dynamischer Mechanismen gezeigt.

[1]National Center for Environmental Prediction

# Abstract

Studying climate change requires reliable models alongside with a principal understanding of atmospheric dynamics and its interaction with other components of the climate system. Both aspects are linked by sensitivities. These sensitivities with respect to boundary, initial, and parameter values can efficiently be calculated with adjoint models, on short time scales. Both, for the adaption of coupled climate models to a prescribed climate, be it for verification or as a scenario, and for the comprehension of climate related dynamical interactions, sensitivities are required which are valid beyond an individual weather condition, *i.e.* for longer time scales.

This study investigates the potential of adjoint methods for climate modelling. This is done with the aim of a coupled assimilation system in mind, but also with the idea to use sensitivities for diagnostic purposes to aid understanding of dynamical dependencies within and between components of the climate system.

We show that adjoint gradients in the atmospheric component of such a system at the chosen relatively coarse resolution of about 5° are able to describe the model sensitivities for integration times beyond 30 days. In an example application a complex parameter field is determined using an averaging method for the gradients, such that the model reproduces a given climate.

For the second goal of development the adjoint atmospheric model is used to determine the optimal forcing for the observed northern hemisphere trend in NCEP[2] winter data of the second half of the $20^{th}$ century. Here, the adjoint model serves solely diagnostic purposes; the dynamics of the climate under investigation is completely determined by the re-analysis data. Thus the data is enhanced by the dynamical knowledge from the adjoint model equations in the investigation of dynamical causalities. The program package developed for this purpose covers numerous eventual requirements for sensitivity calculations by its high flexibility in the choice of the target function through projection of various atmospheric fields. The computation of sensitivities with respect to isentropic potential vorticity is the current highlight of this development.

With this, first steps towards a planned coupled ocean-atmosphere assimilation system for climate studies are done, which could, for instance, make it possible to assimilate paleo-data, and, as a second line of development, the applicability of adjoint models is demonstrated for the investigation of climate-related dynamical mechanisms.

[2]National Center for Environmental Prediction

Überholen ohne Einzuholen.

# Contents


**1 Adjoint theory** **3**
- 1.1 Definition of the adjoint . . . 3
- 1.2 Sensitivity . . . 4
  - 1.2.1 Example for sensitivity: heat exchange . . . 4
  - 1.2.2 Sensitivities and nonlinearity: the Lorenz-'63 -model . . . 5
- 1.3 Stability . . . 7
  - 1.3.1 Normal modes . . . 7
  - 1.3.2 Local growth properties . . . 8
  - 1.3.3 Singular Value Decomposition of the Propagator . . . 8
  - 1.3.4 Inverse and adjoint propagator . . . 9
- 1.4 Climate sensitivities . . . 9
  - 1.4.1 Dependence of sensitivities on the integration period . . . 10
  - 1.4.2 Finding optimal parameters - climate tuning . . . 12
- 1.5 Summary . . . 18

**2 PUMA and its adjoint** **21**
- 2.1 The PUMA model . . . 21
  - 2.1.1 Model equations . . . 22
  - 2.1.2 Parameterisations . . . 23
- 2.2 The adjoint of the atmospheric model . . . 23
  - 2.2.1 Alterations and special directives . . . 24
  - 2.2.2 Reference trajectory handling . . . 24
  - 2.2.3 Customisation . . . 24
- 2.3 Testing of the adjoint model . . . 28

**3 Sensitivities in an atmospheric GCM** **31**
- 3.1 Sensitivities to an initial state . . . 31
- 3.2 Sensitivity of the model climate to a parameter . . . 32
  - 3.2.1 Introduction . . . 32
  - 3.2.2 Model and Parameters . . . 35
  - 3.2.3 Finite Difference Tests . . . 38
  - 3.2.4 Parameter Estimation . . . 38
  - 3.2.5 Conclusions . . . 46

3.3 Assimilation of a model climate . . . . . 50
3.3.1 Aims and Methods . . . . . 50
3.3.2 Single storm track climate (control run) . . . . . 52
3.3.3 Cost function properties . . . . . 52
3.3.4 Forcing reconstruction . . . . . 54
3.3.5 Results and Discussion . . . . . 54

**4 Interpreting the atmospheric circulation trend during the last half of the 20th century 57**
4.1 Introduction . . . . . 58
4.2 Description of the adjoint model . . . . . 61
4.2.1 Relationship of sensitivities and optimal forcing . . . . . 65
4.2.2 Geopotential height as target pattern . . . . . 66
4.2.3 Sensitivity Averaging . . . . . 66
4.3 Results . . . . . 67
4.3.1 The forcing sensitivities . . . . . 67
4.3.2 Forward runs using a linear model . . . . . 74
4.3.3 Forward runs using a nonlinear model . . . . . 76
4.3.4 Forcing restricted to parts of the model domain . . . . . 80
4.4 Summary and discussion . . . . . 81

**5 Overall summary and outlook 85**
5.1 Summary . . . . . 85
5.2 Future improvements and outlook . . . . . 87

**Acknowledgements 89**

**A Sensitivity to Potential Vorticity 91**
A.1 Purpose . . . . . 91
A.2 Formalism . . . . . 92
A.3 Balance conditions . . . . . 94

**B The adjoint modelling environment 97**
B.1 Reference trajectory . . . . . 97
B.2 Adjoint Preprocessing . . . . . 99
B.3 Adjoint integration . . . . . 101
B.4 Adjoint Postprocessing . . . . . 102
B.5 Computational details . . . . . 104

**Literature 107**

**Index 119**

# Introduction

Adjoint meteorological models are well established for applications on short timescales, for instance in the context of numerical weather prediction (assimilation, ensemble generation). Mathematically they are an efficient tool to compute gradients across a model, basically being the transpose of the Jacobian matrix. Adjoint methods have been used in meteorology as early as 1965 for the estimation of forecast error growth in a highly truncated spectral two layer model by Lorenz (1965). His *error matrix* and its transpose are the tangent-linear and adjoint model. Marchuk (1974) makes explicit use of adjoint techniques in the theoretical treatment of weather forecasting problems. These applications are still restricted to analytical models and small numerical applications. Penenko and Obraztsov (1976) apply them to data assimilation, while Cacuci (1981a,b) introduces a general sensitivity theory for nonlinear systems and such, according to Zupanski (1995), initiates adjoint sensitivity studies in meteorology and climatology. The methodology presumably has its origin in optimal control problems (*e.g.* Lions, 1971) like rocket trajectories and nuclear chain reactions. Adjoint models are furthermore indispensable in one of the two main competing algorithms for the creation of ensembles for weather forecasts, namely the SVD-technique applied at ECMWF (*e.g.* Buizza et al., 1993). Further meteorological applications include optimal excitation problems, model tuning and source detection in Euclidian tracer models. For an overview of adjoint applications in earth system modelling see Giering et al. (2003).

When moving to longer timescales principal restrictions complicate the application. The non-linear nature of the modelled processes inflicts a timescale onto the adjoint applications after which the obtained gradients become degenerate (Lea et al., 2000). This study explores methods to mitigate the effect and investigates the applicability of an adjoint atmospheric model (**P**ortable **U**niversity **M**odel of the **A**tmopshere, `PUMA`, Fraedrich et al., 1998, 2005c) to climate related problems. The theoretical background for the adjoint is given in chapter 1, and the problem of adjoint gradients for long lead-times is introduced in section 1.4 along with possible solutions. `PUMA` and its adjoint are introduced in chapter 2. Chapter 3 explores the theory in the context of `PUMA`. While section 3.2 focuses on the gradient of a model climate with respect to three different central model parameters (published as Kaminski et al., 2007), section 3.3 presents a successful

climate assimilation in an idealised setting (published in Blessing et al., 2004). Both parts are encouraging feasibility studies for a Climate Prediction Data Assimilation System (CPDAS).

The linearisation involved in the creation of the tangent-linear and adjoint model creates another potential for the adjoint method. By using realisations from far more complex models as reference trajectory, their climate can be studied within the framework of the adjoint `PUMA` dynamical core. This perspective for diagnosis of dynamical processes and dependencies is explored in chapter 4 at the example of the northern hemisphere atmospheric trend over the winters 1948/49 to 1998/1999 in NCEP reanalysis data (published as Blessing et al., 2008). Several theories (introduced in section 4.1) are trying to identify sources of persistent changes in the atmospheric circulation of the northern hemisphere. With the adjoint technique we present a tool for the exploration of such problems, which has as its only paradigms, apart from the above considerations, the dynamic knowledge from the model equations and the data.

The appendices mostly document the extensive technical developments which were prerequisite for the investigations. Looking at a full set of sensitivities with respect to diagnostic variables, or, as in chapter 4, their forcings, one may wonder how to combine all this information into maps of one measure. Appendix A shows how isentropic potential vorticity can be used for the latter purpose, yielding one sensitivity measure to look at instead of many. The straightforward way would be to construct the adjoint of a potential vorticity inversion. Here, a more implicit way, based on an algorithm proposed by Arbogast (1998) is presented. Finally, appendix B offers a manual to the software which was developed along with the adjoint `PUMA`, and which was used to produce the results of section 4.

# Chapter 1

# Adjoint theory

## 1.1 Definition of the adjoint

The adjoint operator $L^\star$ for a given linear operator $L$ with scalar product $(\cdot, \cdot)$ is defined by

$$(L^\star x, y) = (x, Ly). \tag{1.1}$$

Formally adjoint boundary conditions are part of the definition of the adjoint, basically describing the space $S^\star$ on which $L^\star$ operates and fulfils the above equation. For most adjoint operators used in this work the domains of $L$ and $L^\star$ are identical with cyclic boundary conditions. For the sums used in the numerical calculations of the scalar product this translates to summation over the same gridpoints. In the remaining cases the domain of $L^\star$ is obvious from the nature of the physical problem. Moreover, the adjoint of the numerical implementation of the tangent-linear was generally used, rather than implementing the numerical approximation of the adjoint equations. Therefore the adjoint and tangent-linear model fulfil the above relationship to machine precision (see section 2.3). Vertical derivatives, for instance, do not require equal values of $x$ at the endpoints of the summation under this approach, as it would be necessary for the formal adjoint $-\partial/\partial\sigma$ of $\partial/\partial\sigma$.

The creation of the linear and adjoint codes follows the principles described in Giering and Kaminski (1998) or Appendix B of Kalnay (2003). This means linearising every relevant line of model code according to the chain rule of differentiation and providing the necessary reference values. The adjoint is then the transpose of this, which means each line of differentiated code is converted into the adjoint statement(s) individually and the order is reversed, since for the transpose of a chain of operators the following holds: $(\mathbf{A}\,\mathbf{B}\,\mathbf{C})^T = \mathbf{C}^T\,\mathbf{B}^T\,\mathbf{A}^T$.
The tangent-linear model describes the first order approximation of the growth of errors in the full model. It is the Jacobian matrix combined out of the Jacobian matrices of the chain of operators representing the full model. The errors or perturbations can theoretically extract infinite amounts of energy from the reference

trajectory (or forecast) without feeding back on it and without saturating. The model is linear despite the fact that the reference trajectory is time varying as prescribed in the course of linearisation, ideally by an integration of the fully nonlinear model.

## 1.2 Sensitivity

### 1.2.1 Example for sensitivity: heat exchange

In order to illustrate the concept of an adjoint model let us turn to the example of a very simple physical model. It consists of two coupled reservoirs with equal heat capacity which exchange heat by conduction with a constant transfer coefficient $[c] = 1/\mathrm{s}$. Their temperatures $T_1$ and $T_2$, forming the vector $\boldsymbol{T}$, are consequently determined by:

$$\dot{\boldsymbol{T}} = \mathbf{A}\boldsymbol{T}, \text{ with } \mathbf{A} = \frac{1}{2}\begin{pmatrix} -c & c \\ c & -c \end{pmatrix}. \tag{1.2}$$

The propagator matrix $\mathbf{R}_{t_1}^{t_2}$ results from integration:

$$\mathbf{R}_{t_1}^{t_2} = \exp\left(\int_{t_1}^{t_2} \mathbf{A}dt\right) \tag{1.3}$$

$$= \frac{1}{2}\begin{pmatrix} 1+\mathrm{e}^{-c(t_2-t_1)} & 1-\mathrm{e}^{-c(t_2-t_1)} \\ 1-\mathrm{e}^{-c(t_2-t_1)} & 1+\mathrm{e}^{-c(t_2-t_1)} \end{pmatrix}. \tag{1.4}$$

$$\tag{1.5}$$

By definition the tangent-linear propagator is composed of the derivatives of the model result with respect to the initial conditions:

$$\left(\mathbf{R}_{t_1}^{t_2}\right)_{ij} = \left(\frac{\partial T_i(t_2)}{\partial T_j(t_1)}\right). \tag{1.6}$$

The model itself is linear, therefore it is indistinguishable from the tangent-linear propagator. But note that the model describes the evolution of its state variables while the tangent-linear model describes the first-order evolution of perturbations of the state variables. Owing to the symmetry of the system matrix $\mathbf{A}$, also tangent-linear and adjoint propagator are identical:

$$\left(\mathbf{R}_{t_1}^{t_2}\right)^T = \mathbf{R}_{t_1}^{t_2} \tag{1.7}$$

The inverse propagator $\left(\mathbf{R}_{t_1}^{t_2}\right)^{-1}$, in contrast, follows in this case from $\left(\mathbf{R}_{t_1}^{t_2}\right)^{-1} = \left(\mathbf{R}_{t_2}^{t_1}\right)$ as:

$$\left(\mathbf{R}_{t_1}^{t_2}\right)^{-1} = \frac{1}{2}\begin{pmatrix} 1+\mathrm{e}^{c(t_2-t_1)} & 1-\mathrm{e}^{c(t_2-t_1)} \\ 1-\mathrm{e}^{c(t_2-t_1)} & 1+\mathrm{e}^{c(t_2-t_1)} \end{pmatrix} = \frac{\partial T_i(t_1)}{\partial T_j(t_2)} \tag{1.8}$$

Furthermore a cost function $J$ is introduced which depends on the observed error at final time $\varepsilon_{t_2} = \delta T(t_2)$:

$$J = \frac{1}{2} \langle \varepsilon_{t_2}; \varepsilon_{t_2} \rangle = \frac{1}{2} (\varepsilon_{t_2})^T \varepsilon_{t_2} \tag{1.9}$$

Using $\mathbf{R}$ as first order (in this case exact) approximation of the evolution of initial state perturbations, $\varepsilon_{t_2} = \mathbf{R}_{t_1}^{t_2} \varepsilon_{t_1}$ gives $J = \frac{1}{2} (\mathbf{R}_{t_1}^{t_2} \varepsilon_{t_1})^T \mathbf{R}_{t_1}^{t_2} \varepsilon_{t_1}$. Differentiation of $J$ with respect to initial state perturbations yields:

$$\nabla_{\varepsilon_{t_1}} J = (\mathbf{R}_{t_1}^{t_2})^T \mathbf{R}_{t_1}^{t_2} \varepsilon_{t_1} = (\mathbf{R}_{t_1}^{t_2})^T \varepsilon_{t_2} \tag{1.10}$$

Panel (a) of Fig. 1.1 shows the evolution of an initial state perturbation $\delta T(t_1) = (5K, 0K)$ with the tangent-linear propagator, panel (b) the evolution of a final state perturbation $\delta T(t_2) = (5K, 0K)$ with the inverse tangent-linear propagator, and panel (c) the evolution of the derivative of $J$ for a final state perturbation $T^\star(t_2) = \varepsilon_{t_2} = (5K, 0K)$ (since $\mathbf{R}_{t_2}^{t_2}$ is the identity) with the adjoint propagator. The forward model tends to equilibrate any existing temperature difference while conserving total energy. A positive perturbation at initial time in one of the boxes as in Fig. 1.1a leads to a higher temperature of both boxes at final time. The inverse model (Fig. 1.1b) shows that for a higher end temperature in only one box, the temperature of both boxes has to be changed at initial time. The magnitude of the necessary changes increases the further they lie back in time. The derivative of $J$, $T^\star(t)$, shows decreasing sensitivity the further back it goes (Fig. 1.1c). It asymptotically stabilises to the same constant value for both boxes, reflecting the fact that due to energy conservation and the coupling of the boxes, both boxes have in the far limit the same ability to change the final temperature of box one (reflected by the value of $J$) with a fixed sensitivity.

### 1.2.2 Sensitivities and nonlinearity: the Lorenz-'63 -model

In the previous section the tangent-linear and adjoint was introduced for a linear model. Now we turn to a nonlinear model. One of the technical implications is, that the linearisation now is carried out with respect to a time-varying reference state for which a state trajectory of the nonlinear model is used. This kind of linear model is called tangent-linear.

The Lorenz (1963) model is the result of a low order spectral truncation of a convection model introduced by Rayleigh, Lord (1916). A fluid is heated from the bottom by a prescribed temperature difference between bottom and top. Here, the problem is cyclic in one horizontal direction and uniform in the other. The Lorenz'63 equations describe one mode of the vertical stream-function ($X$) and two modes of the vertical temperature distribution ($Y, Z$).

$$\dot{X} = -\sigma X + \sigma Y \tag{1.11}$$

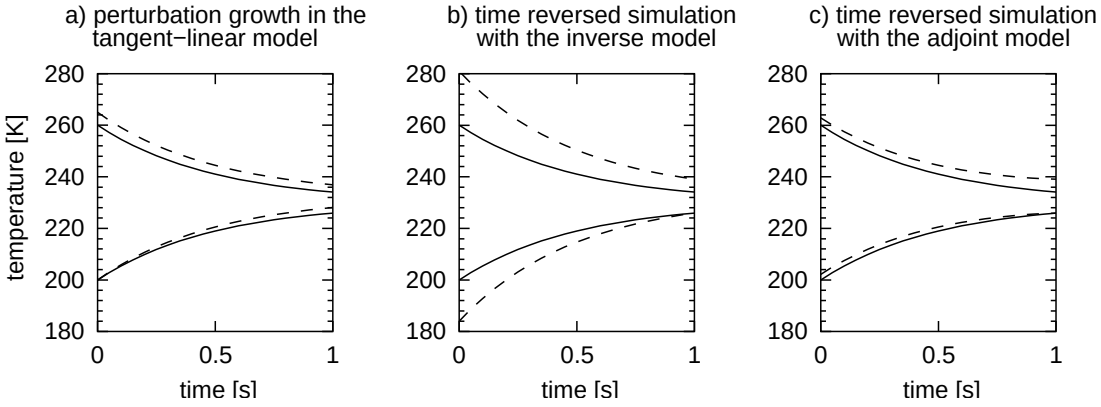


Figure 1.1: Propagation of a perturbation $\varepsilon = (5\ \mathrm{K}, 0\ \mathrm{K})^T$ (dotted) of the two-box heat conduction model in the **(a)** tangent-linear model ($\delta T(0) := \varepsilon$), **(b)** inverse model ($\delta T(1) := \varepsilon$), and **(c)** the adjoint model ($T^\star(1) = \nabla_{T(1)} J := \varepsilon$).

$$\dot{Y} = rX - Y - XZ \tag{1.12}$$
$$\dot{Z} = -bZ + XY. \tag{1.13}$$

The parameter $\sigma$ is the Prandtl-number, $r$ the Rayleigh-number, normalised with its critical value, and $b$ a measure for the geometry of the simulated convection cell. The dot denotes the derivative with respect to dimensionless time. The equations can be numerically integrated with e.g. a fourth order Runge-Kutta scheme and lead to the well known picture of the Lorenz-attractor for the parameter choices $\sigma = 10$, $r = 28$, and $b = \frac{8}{3}$. These choices describe a fluid not much unlike water ($\sigma$ about 7), in convective mode ($r > 1$).

The equations of the tangent linear model relative to a reference trajectory $\boldsymbol{X}_R(t) = (X_R(t), Y_R(t), Z_R(t))^T$ are:

$$\delta\dot{\boldsymbol{X}} = \begin{pmatrix} -\sigma & \sigma & 0 \\ r - Z_R(t) & -1 & -X_R(t) \\ -b & X_R(t) & Y_R(t) \end{pmatrix} \delta\boldsymbol{X}, \tag{1.14}$$

formally yielding the system matrix of the adjoint:

$$\mathbf{A}^\star|_t = \begin{pmatrix} -\sigma & r - Z_R(t) & -b \\ \sigma & -1 & X_R(t) \\ 0 & -X_R(t) & Y_R(t) \end{pmatrix} \tag{1.15}$$

Note that the system matrix is time dependent through its dependency on the reference trajectory $\boldsymbol{X}_R(t)$, but nonetheless linear since $\boldsymbol{X}_R(t)$ does not depend on $\delta\boldsymbol{X}$ in the tangent-linear model. This is the essence of tangent-linearity. The numerical implementation of the adjoint model was derived from the numerical version of the tangent-linear model which in turn was derived from a Runge-Kutta integration scheme of the original equations (Eqs. 1.11-1.13). For the

tangent-linear model this path of computation corresponds to a large degree to the alternative approach of integrating Eq. (1.14) using a Runge-Kutta scheme. But for the adjoint model one important difference must be noted: the outlined way of computation leads to an algorithm which is adjoint to the numerical tangent-linear model, *i.e.* it also simulates the effects of the discretisation error of the forward model. Thus it ensures that a numerical catenation of tangent-linear and adjoint operator corresponds closely to the operation of a symmetric matrix, but it also leads to the computation of sensitivities which arise partly from discretisation errors of the applied numerical scheme. Sirkes and Tziperman (1997) show for a special case that this can lead to a useless albeit precise adjoint model.

## 1.3 Stability

This section aims to give a perspective from stability theory on sensitivities. Intuitively it is clear that a stable system will be insensitive to perturbations while perturbations triggering an instability will find the system to be very sensitive. As an excursion this viewpoint allows for a very compact comparison of adjoint and inverse thinking in section 1.3.4.

The fastest growing perturbation is defined for a limited time and a corresponding reference trajectory. Eigenmodes on the other hand are computed for fixed reference states describe the tangent linear growth for the long time limit of these states. They are most likely not related to the first global Lyapunov exponent of the nonlinear system. A comparison of further modes from the different applicable eigentechniques can be found in e.g. Frederiksen (2000).

For prediction purposes it is desirable to assess the preferred directions of error growth. In this context there are several competing methods. All try to provide initial perturbations for ensemble runs such that with a minimal number of ensemble members a reliable estimate of the expected forecast error is obtained. Especially singular value decomposition (SVD) and breeding have produced much debate. While SVD identifies initial perturbations which have maximum growth in a given norm and forecast time in the tangent linear model, the breeding technique claims to be a nonlinear extension of the concept of Lyapunov vectors.

### 1.3.1 Normal modes

If the linearisation is around a constant reference trajectory, as e.g. a mean state, $\mathbf{R} = \mathrm{e}^{\mathbf{A}(t-t_0)}$ is the propagator for the linearised system $\delta\dot{\mathbf{x}} = \mathbf{A}\delta\mathbf{x}$. $\mathbf{A}$ and $\mathbf{R}$ share the same eigenvectors, and the eigenvalues of $\mathbf{R}$ are $\lambda_i = \mathrm{e}^{\alpha(t-t_0)}$ ($\alpha_i$ being the eigenvalues of $\mathbf{A}$). These eigenvectors are known as *normal modes*, even though in general $\mathbf{A}$ is not normal. For a time-varying trajectory, the eigenvectors of $\mathbf{R}$ are known as *finite time normal modes*, and those of $\mathbf{R}^\star$ as *finite time adjoint*

*modes* (Frederiksen, 2000).
In a non-linear system one has to bear in mind that linearisation with respect to a constant reference state is only locally justified in phase space. Therefore conclusions about the long time behaviour of the system based on normal modes are only of limited validity.

### 1.3.2 Local growth properties

Various definitions for local Lyapunov exponents $\lambda$ exist. One of them stems from the relation $\exp(\lambda t)e_i = \mathbf{R}_{t_1}^{t_2} e_i$, where $e_i$ is the eigenvector of $\mathbf{R}_{t_1}^{t_1}$ with largest eigenvalue. It gives the upper bound for the error growth on a piece of the attractor (Trevisan and Legnani, 1995). In atmospheric GCMs, the fastest growing modes over limited time gain much energy by geostrophic adjustment (Szunyogh et al., 1997) in their initial growth state. On top of that these growth rates are only valid for infinitesimal perturbations. The feedback of finite perturbations most likely reduces growth due to saturation effects and the reduction of the available energy of the reference state.

### 1.3.3 Singular Value Decomposition of the Propagator

The error or propagator matrix $\mathbf{R}$ of the model can be decomposed into two unitary ($\mathbf{U}^\star = \mathbf{U}^{-1}$, implying that the column vectors $\mathbf{u_i}$ form an orthonormal system) matrices $\mathbf{U}$ and $\mathbf{V}$ and a diagonal matrix $\mathbf{\Sigma}$ as $\mathbf{R} = \mathbf{V\Sigma U}^\star$. The diagonal elements $\sigma_i$ of $\mathbf{\Sigma}$ are the singular values of $\mathbf{R}$ (Golub and van Loan, 1983). In the presence of a metric matrix $\mathbf{C}$ in the scalar product, as in $\langle \cdot ; \mathbf{C} \cdot \rangle$, a preferable choice is

$$\mathbf{R} = \mathbf{C}^{-\frac{1}{2}} \mathbf{V\Sigma U}^\star \mathbf{C}^{\frac{1}{2}}. \tag{1.16}$$

Note that $\mathbf{C}$ is chosen to be real, symmetric (i.e. self-adjoint) and invertible. Consequently the adjoint operator $\mathbf{R}^\star$ can be written as

$$\mathbf{R}^\star = \mathbf{C}^{\frac{1}{2}} \mathbf{U\Sigma V}^\star \mathbf{C}^{-\frac{1}{2}}. \tag{1.17}$$

The growth of a perturbation $\delta\mathbf{x}$ in the $\mathbf{C}$-norm is given by the ratio $r$

$$r = \frac{\langle \mathbf{R}\delta\mathbf{x}; \mathbf{CR}\delta\mathbf{x} \rangle}{\langle \delta\mathbf{x}; \mathbf{C}\delta\mathbf{x} \rangle} \tag{1.18}$$

$$\overset{(1.16)}{=} \frac{\langle \mathbf{U}^\star \mathbf{C}^{\frac{1}{2}} \delta\mathbf{x}; \mathbf{\Sigma}^2 \mathbf{U}^\star \mathbf{C}^{\frac{1}{2}} \delta\mathbf{x} \rangle}{\langle \mathbf{C}^{\frac{1}{2}} \delta\mathbf{x}; \mathbf{C}^{\frac{1}{2}} \delta\mathbf{x} \rangle} \tag{1.19}$$

Apparently, growth is described by the projection of $\mathbf{C}^{\frac{1}{2}}\delta\mathbf{x}$ onto the column vectors $\mathbf{u}_i$ of $\mathbf{U}$ (initial time singular vectors) and the singular values $\sigma_i$ of $\mathbf{\Sigma}$ such that for $\delta\mathbf{x} = \mathbf{C}^{-\frac{1}{2}}\mathbf{u}_i$ equation (1.18) reduces to $r = \sigma_i^2$. Therefore, in the linearised

system, the maximum growth over a finite time in the $\mathbf{C}$-norm is determined by the largest singular value of $\mathbf{C}^{\frac{1}{2}}\mathbf{R}\mathbf{C}^{-\frac{1}{2}}$.
The initial time singular vectors $\mathbf{u}_i$ of $\mathbf{C}^{\frac{1}{2}}\mathbf{R}\mathbf{C}^{-\frac{1}{2}}$ are also the eigenvectors of $\mathbf{C}^{-\frac{1}{2}}\mathbf{R}^{\star}\mathbf{C}\mathbf{R}\mathbf{C}^{-\frac{1}{2}}$, while the final time singular vectors $\mathbf{v}_i$ of $\mathbf{C}^{\frac{1}{2}}\mathbf{R}\mathbf{C}^{-\frac{1}{2}}$, are also the eigenvectors of $\mathbf{C}^{\frac{1}{2}}\mathbf{R}\mathbf{C}^{-1}\mathbf{R}^{\star}\mathbf{C}^{\frac{1}{2}}$, both with the same eigenvalues $\sigma_i^2$. The nomenclature *initial* and *final time singular vector* becomes evident from the relationship $\mathbf{C}^{\frac{1}{2}}\mathbf{R}\mathbf{C}^{-\frac{1}{2}}\mathbf{u}_i = \sigma_i\mathbf{v}_i$.

### 1.3.4 Inverse and adjoint propagator

In order to excite an anomaly which has large projection onto a particular *final time singular vector*, $\mathbf{v_i}$, a perturbation is necessary, which has projection onto the corresponding *initial time singular vector*, $\mathbf{u_i}$. If $\delta\mathbf{\Psi}_{target} = \mathbf{R}\delta\mathbf{x}$, then

$$\delta\mathbf{x} = \mathbf{R}^{-1}\delta\mathbf{\Psi}_{target} = \mathbf{C}^{-\frac{1}{2}}\mathbf{U}\mathbf{\Sigma}^{-1}\mathbf{V}^{\star}\mathbf{C}^{\frac{1}{2}}\delta\mathbf{\Psi}_{target}. \tag{1.20}$$

This inverse operator is difficult to obtain. Moreover it is not optimal in the sense that it does not minimise the energy which is necessary to excite the target pattern $\mathbf{\Psi}_{target}$. The inverse matrix $\mathbf{\Sigma}^{-1}$, which has the reciprocal singular values in the diagonal, gives $\delta\mathbf{x}$ more projection onto weakly growing modes and less onto the ones with stronger amplification. But note the resemblance to Eq. (4.9), which is derived in section 4.2 for the optimal perturbation. It reads

$$\delta\mathbf{x_{opt}} = \lambda\mathbf{R}^{\star}\delta\mathbf{\Psi}_{target} = \lambda\mathbf{C}^{-\frac{1}{2}}\mathbf{U}\mathbf{\Sigma}\mathbf{V}^{\star}\mathbf{C}^{\frac{1}{2}}\delta\mathbf{\Psi}_{target} \tag{1.21}$$

when translated to the nomenclature and problem of this section (here, $\lambda$ is just a scalar factor). This time $\mathbf{\Sigma}$ is not inverted in order to make optimal use of the energy of the initial perturbation by emphasising the singular vectors which dominate the growth in the direction of the target. The energetically optimal perturbation (Eq. 1.21, a.k.a.*maximum sensitivity perturbation*, Frederiksen, 2000) and the inverted target (Eq. 1.20) are the same if and only if the target pattern has projection only on final time singular vectors with singular values of unity i.e. neutral growth.

## 1.4 Climate sensitivities

When it comes to the sensitivity of the climate of a chaotic model with respect to parameters or initial conditions (control variables hereafter), problems arise. It turns out that the response of the observed quantity is not smoothly depending on the control variables, at least not for finite averaging times. This "un-smoothness" is reflected by gradients (when computed with the adjoint model) which grow very rapidly with averaging time.

### 1.4.1 Dependence of sensitivities on the integration period

For the long time limit exponential growth of the sensitivities can be expected, since in the far limit the growth of the largest Lyapunov exponent should dominate. Indeed Figs. 1.2 and 1.3 show exponentially growing sensitivities with increasing lead time for most verification times (compare Fig. 3.1 for the global atmospheric circulation model `PUMA`). These are directly linked to predictability. Interestingly, the vertically banded structure of the norm of the sensitivity vector in Figs 1.2 and 3.1 is a hint that predictability seems to be more a property of the state to be predicted than of the development leading to it.

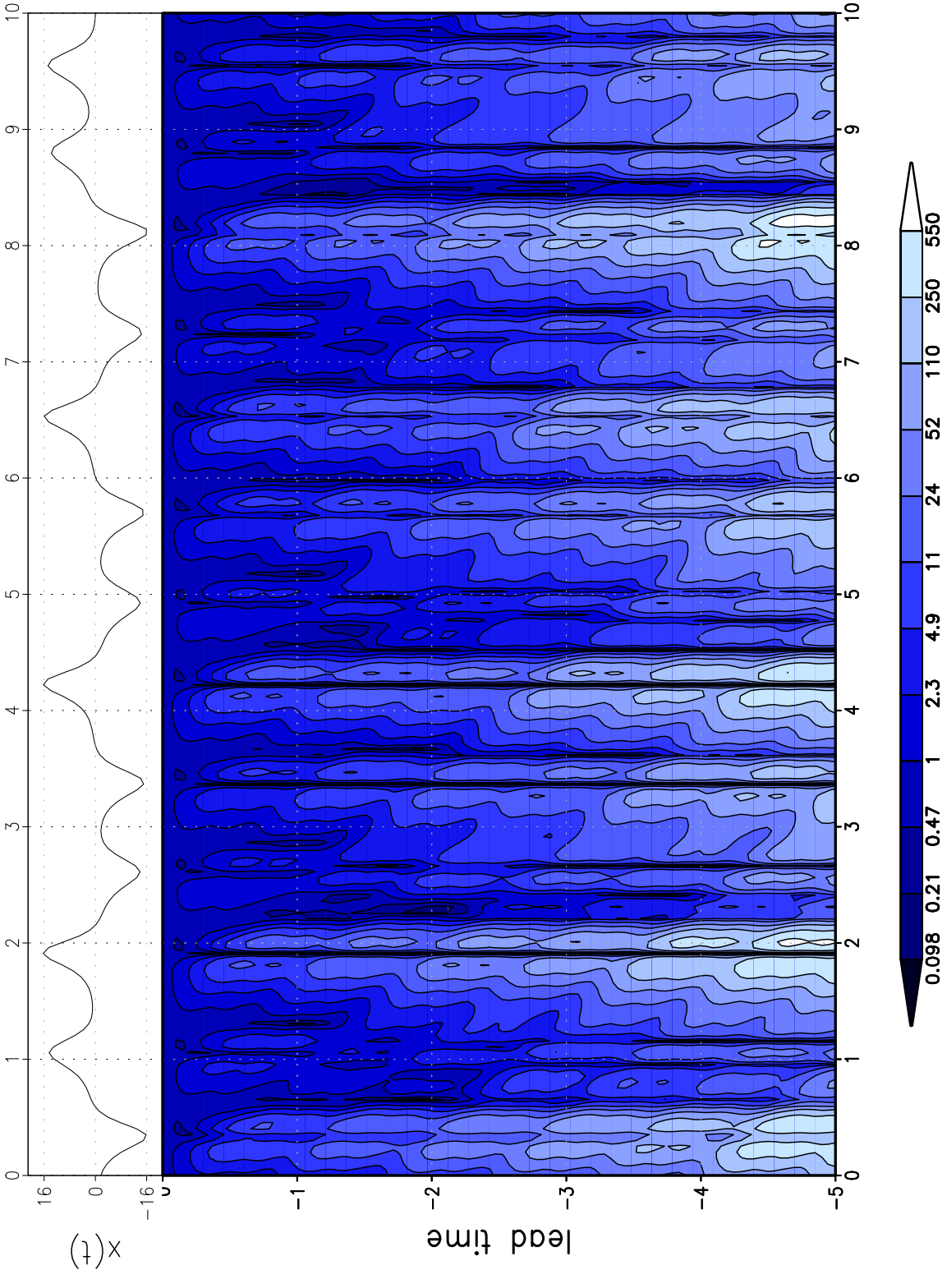


Figure 1.2: $X$-component of the Lorenz-'63 model (top) and adjoint sensitivity $\|\boldsymbol{X}^\star\|$ (bottom) for different lead (lower ordinate) and verification times (abscissae). Contours are logarithmic.

In principle, exponential growth of sensitivities, should also appear when finite differencing methods with very small perturbations are used. This problem was dealt with by Lea et al. (2000) for the Lorenz-'63-model and by Lea et al. (2002) for an ocean model. They achieved best results with an ensemble method and intermediate averaging times. This averaging time has to be a compromise between the constraints from the exponentially growing gradient and the time the model dynamics takes to respond to the changed control variables. Since growth of the adjoint gradients is directly related to the first Lyapunov-exponent of the model in question Köhl and Willebrand (2002) successfully used an adjoint model with reduced spatial resolution, and therefore reduced instability, for the gradient computations, while McLay and Marotzke (2008) demonstrate limits for the method in an eddie resolving ocean model. Based on theoretical considerations Eyink et al. (2004) suggest two algorithms related to Lea's approach for the practical computation of climate sensitivities. The exponential growth of the sensitivities is not only a problem for numerical reasons but also for statistical ones, since the distribution of the sensitivities becomes degenerate, with a non-existing mean. They also show that for the Lorenz-'63-model the required ensemble size grows very quickly with averaging time to an extent which would make the method impractical for a computationally more demanding model. How far this carries over to an atmospheric global circulation model will play an important role in chapters 3 and 4.

### 1.4.2 Finding optimal parameters - climate tuning

Probably the main problem with the computations of climate sensitivities with an adjoint model is the limited time range in which the adjoint model can give a sensitivity which is not only valid for an infinitesimal perturbation but for a finite one. In any nonlinear model these two are trivially not identical. Therefore Blessing et al. (2004) suggest a technique (documented earlier by Pires et al., 1996) where the averaging time for the climate is varied from very short times where the linearisation is a good approximation to the model dynamics to longer times which are more relevant to climate. There are three underlying assumptions to this technique:

1. There is a unique set of optimal parameters.

2. The target function is flat in parameter space around the solution, *i.e.* adjoint gradients approximate the macroscopic gradient or sensitivity to finite perturbations near the optimal parameter value.

3. The optimal parameters for the different averaging times form a curve in parameter space, *i.e.* a small change in averaging time only leads to a small change in parameters.

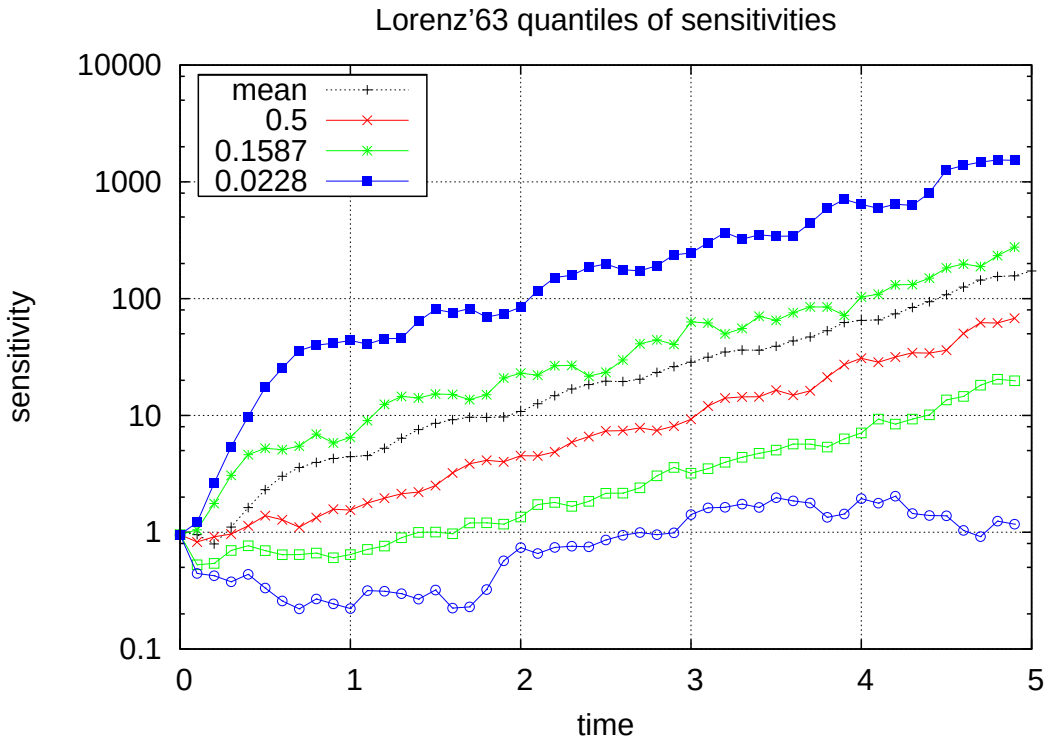


Figure 1.3: Mean and quantiles of the norm $\|\boldsymbol{X}^\star\|$ of the adjoint sensitivities of the $X$-component of the Lorenz'63 system from Fig. 1.2. The displayed quantiles are from a 1000 member ensemble and correspond to median, $1\sigma$, and $2\sigma$ of a normal distribution. Note that $\|\boldsymbol{X}^\star\|$ as a positive definite quantity cannot be normally distributed and more likely follows a Maxwell-Boltzmann distribution for the three-component Lorenz'63 system.

For study purposes the first assumption can be fulfilled in part by an identical twin experiment in which a given parameter set produces a climate which is then attempted to recover with the same model, starting from perturbed parameters. The second assumption is a consequence of the first one, but the notion of *near* may converge to infinitesimality for increasing averaging times (the timescale on which climate is defined). Also the third assumption is probably not justified for long averaging times, especially when the system trajectory of the model passes bifurcation points. Nonetheless, this may be smoother than the dependence of the observed climate on the parameters for a fixed averaging time.
To check the validity of these assumptions in a highly nonlinear model, many integrations were made with the Lorenz-'63 model for different values of the parameter $r$ and varying integration times, in the manner of Fig. 2 of Lea et al. (2000). The squared distance between the resulting time mean value of $Z$ and a fictional target value (26) is plotted in Fig. 1.4. This shows that all the above assumptions are violated for the Lorenz-'63 model, maybe except for the local flatness at the solution. Instead the figure shows the typical self-similar structures of a fractal. Averaging over 10 (Fig. 1.5a) and 100 (Fig. 1.5b) different initial conditions removes some of the fractal structure and makes the path from left to right into the absolute minimum of the cost function on a longer timescale considerably smoother. But even for the 100-member ensemble secondary minima remain which will impede any algorithm that relies on gradient information.

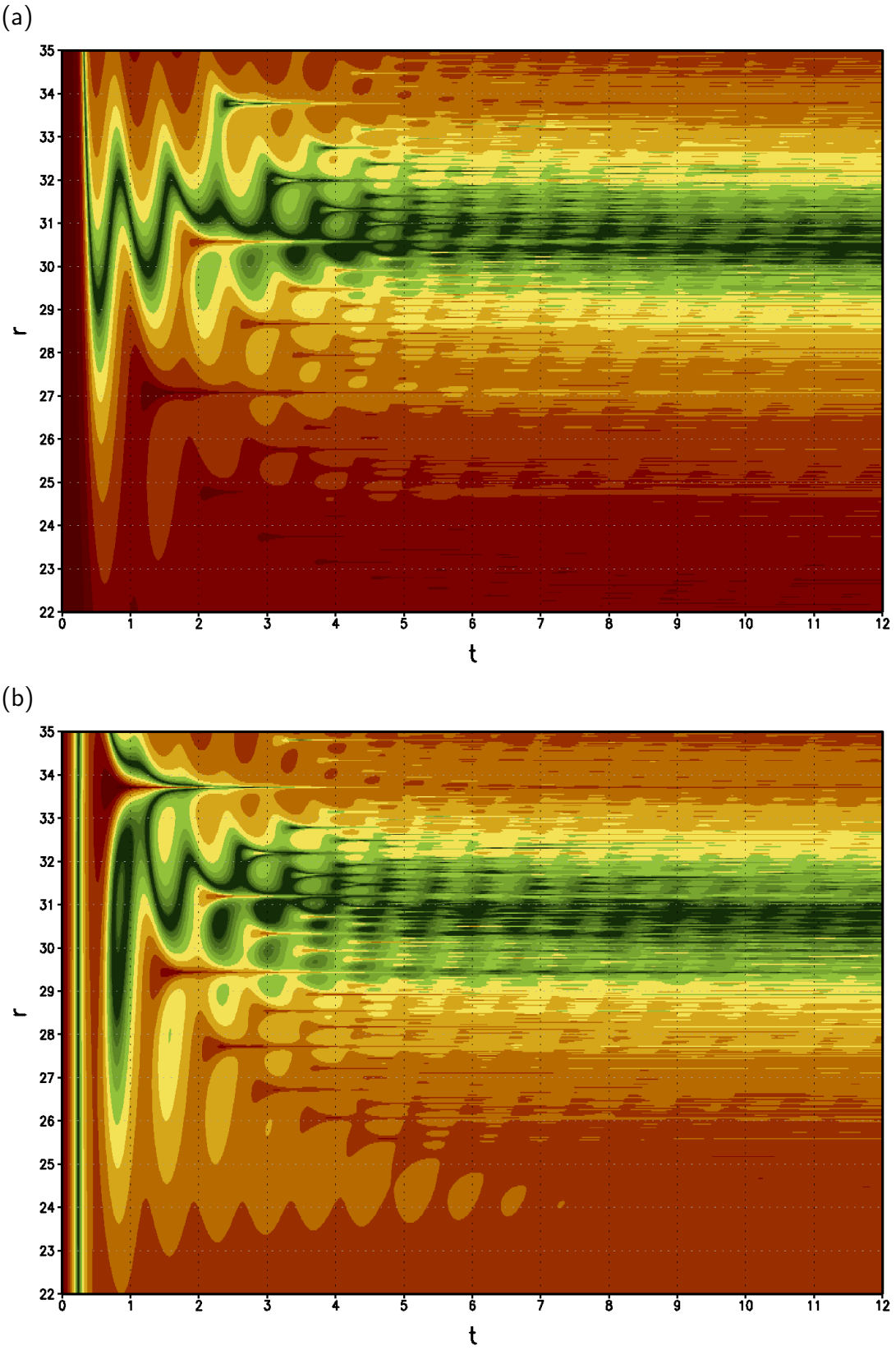


Figure 1.4: Lorenz-'63 model: Value of cost functions $J(r,t) = (\bar{Z}^t(r) - 26)^2$ for different averaging times $t$ and parameter $r$. **(a)** with initial condition $\boldsymbol{X}(0) = (-2.4, -3.7, 14.98)$, and **(b)** with initial condition $\boldsymbol{X}(0) = (8, -2, 36.05)$, same as for lines 1 and 2 of Fig. 2 in Lea *et al.* (2000), which are cross-sections of these plots. Contours are logarithmic with black as the minimum and identical levels for all subfigures.

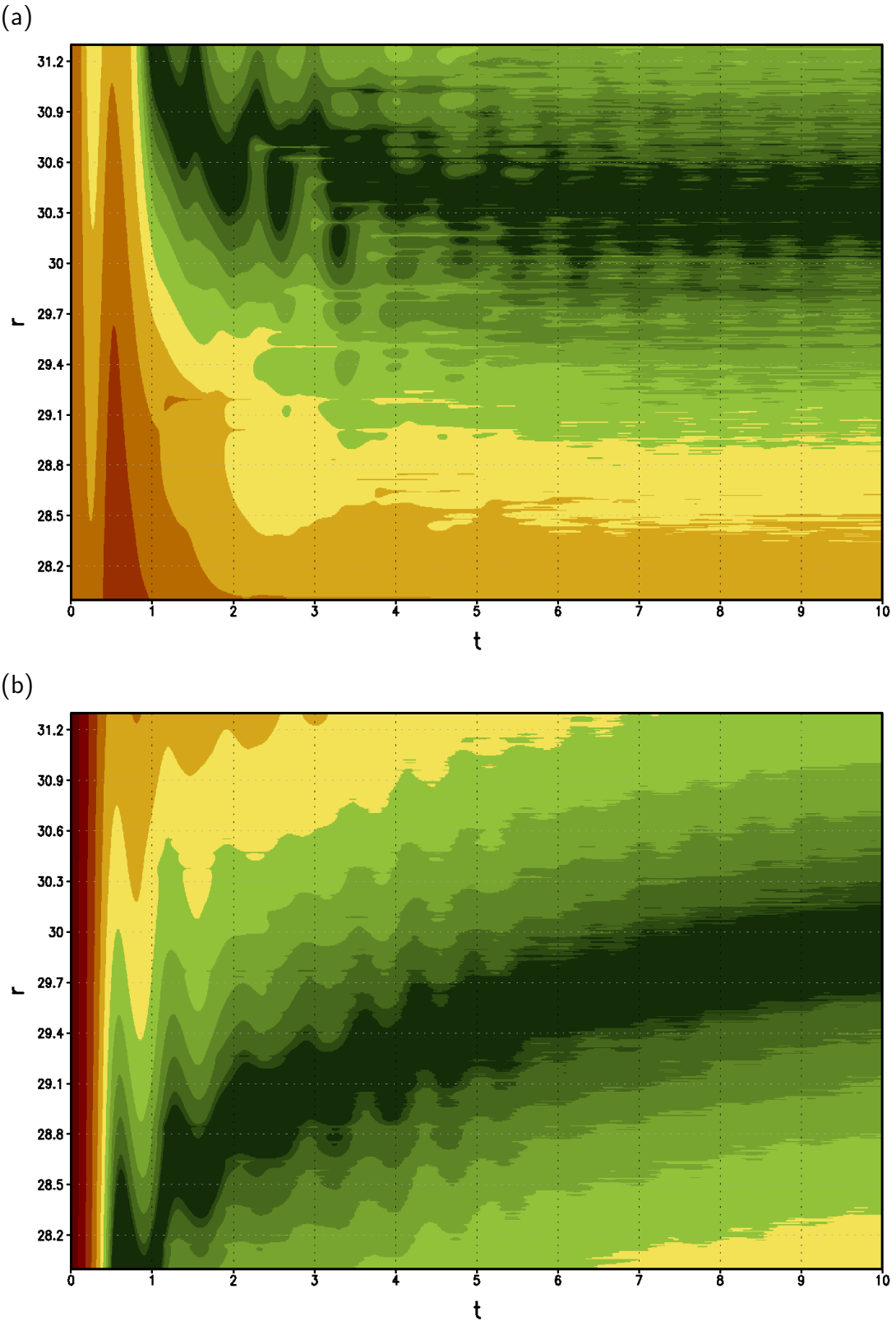


Figure 1.5: As Fig. 1.4, but for ensemble means and a smaller parameter range: **(a)** Ensemble average over 10 different initial conditions taken at intervals from one model run, **(b)** same as (a) but with 100 different initial conditions from a different run. Contours are logarithmic with black as the minimum and identical levels as in Fig. 1.4.

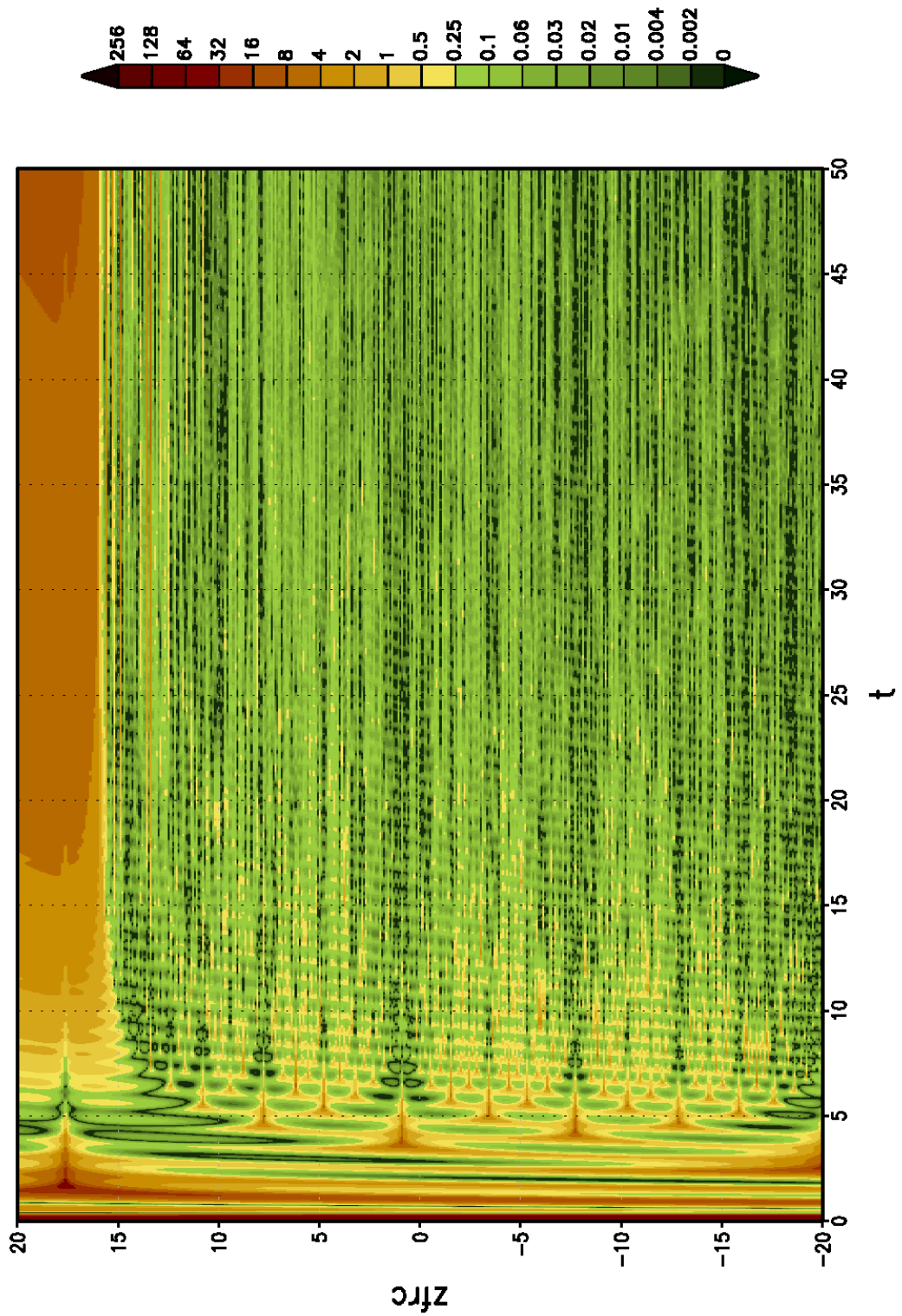


Figure 1.6: Squared deviation of the time averaged $Z$-component of the Lorenz model from the unforced mean for different averaging times $t$ and forcing strengths. Starting point of the integration is $\boldsymbol{X}(0) = (-2.4, -3.7, 14.98)$, as in Fig. 1.4a. The colour scale is approximately logarithmic.

In section 4.2 a technique is described where the gradient with respect to a constant forcing over a certain period of time is computed. Applying this approach to the Lorenz-attractor and forcing, for instance, the $Z$-component with a forcing $f_Z$ over time $t$ yields Fig. 1.6. The plotted quantity is, as above, the deviation of the time mean model output from some target value $Z_a$: $J = (\bar{Z}^t - Z_a)^2$. Here $Z_a$ is chosen to be the unforced mean over 50 time units. The adjoint gradient of $J$ with respect to $Z$-forcing, $f_Z^\star = \nabla_{f_Z} J = 2(\frac{\partial \bar{Z}^t}{\partial f_Z})^\star (\bar{Z}^t - Z_a)$ is structurally equivalent to the derivative of the projection $I$ used in section 4.2. Fig. 1.6 indicates that a relatively wide range of change of $f_Z$ has only little impact on the climatological value of $\bar{Z}^t$. Nonetheless, $\nabla_{f_Z} J$ will show very high values because of the small scale structure of $J$. This again, renders the adjoint gradients of $J$ useless for determining the sensitivity or finding the global minimum for this case. These examples are important to bear in mind when evaluating sensitivity fields. Lea et al. (2002) shows similar problems for an ocean model. To what extent these effects hamper the application of `PUMA`, is investigated in sections 3.2 and 3.3.3. For comparison of `PUMA` with Fig. 1.6, see Fig. 3.12.

## 1.5 Summary

In this chapter we showed the concept of the adjoint model in a linear (heat exchange) and a non-linear (Lorenz'63) example. In the course of this, tangent-linearity is introduced as linearity with respect to a predefined time-varying reference state. Since the adjoint is the transpose of the Jacobian matrix of the model, it runs backward in time, efficiently computing gradients when the derivatives of a low-dimensional output with respect to a high-dimensional input are required.

Sections 1.2.1 shows that this is fundamentally different from a mathematically inverse model. With the aid of the singular value decomposition of the propagator, introduced with the stability theory in section 1.3, an expression for this in singular value space is found in section 1.3.4, showing that the inverse model highlights decaying structures and attenuates growing structures (Eq. 1.20). In contrast, the adjoint sensitivity calculation highlights those initial time structures whose corresponding final time structures have large projection onto the target (Eq. 1.21). This perspective on the stability theory of non-normal linear operators is important for the understanding of the limitations of the tangent-linear model in a climate context. In section 1.4 we show how the value of the adjoint gradients or sensitivities degrades with integration time in the Lorenz'63 model and discuss some techniques how to circumvent this gap between the first order Taylor approximation and the actual behaviour of a finite perturbation in a non-linear model. One technique is dismissed as it can be demonstrated, using the Lorenz'63 system, that it cannot be generally expected that the phase space topology of the target function has the required properties, namely a smooth transition of a unique minimum at short integration time to the global minimum

at increased integration time. From the literature and conceptual experiments we show, that two other techniques are more promising, which are, in the context of a numerical atmospheric model, reduction of spatial resolution in order to suppress fast-growing small scale phenomena which may be of subordinate importance to the large-scale circulation (Köhl and Willebrand, 2002), and second, averaging of the gradients over many realisations at many locations in model state-space (reference trajectory ensemble). This does not necessarily increase the accuracy of the gradient at the given location in state space, but reflects the sensitivity of the model climate to perturbations of the respective quantity, even if the lead time has to be chosen relatively small (compared to climate time scales) in order to ensure that the average of the gradients remains a meaningful, non-degenerate quantity (Eyink et al., 2004). In the following chapters these concepts will be tested for a numerical model of the global atmospheric circulation.

# Chapter 2

# PUMA and its adjoint

In this work, the **P**ortable **U**niversity **M**odel of the **A**tmosphere (PUMA, Fraedrich et al., 1998, 2005c) is used[1]. Descriptions of the variations in the individual setups are provided in the respective sections, while the more technical aspects of the adjoint puma code with its extensions for the computation of derived adjoint quantities used in chapter 4 are described in appendix B.

## 2.1 The PUMA model

PUMA is a primitive equations model with Newtonian cooling, Rayleigh friction and optional orography. The model equations are solved on $\sigma$-levels on a Gaussian grid with the spectral transfer method and a semi-implicit time-stepping scheme. Nonlinear tendencies are computed in gridpoint-space. The spacing of the $\sigma$-levels is equidistant in this study but has recently been changed to allow for customised settings in order to study stratospheric dynamics (Kunz 2008, *in preparation*). The model is based on the spectral model described in Hoskins and Simmons (1975) with the vertical scheme of Simmons and Burridge (1981). It has recently been validated by Liakka (2006). The model has been used in various studies, ranging from different types of stochastic forcing (Perez-Munuzuri et al., 2003; Seiffert et al., 2006; Sardeshmukh and Sura, 2007), the dependence of entropy production on various parameters (Kunz et al., 2008a; Kleidon et al., 2003, 2006), low-frequency variability and the internal large-scale dynamics (Frisius et al., 1998; Franzke et al., 2000, 2001; Walter et al., 2001; Müller et al., 2002; Fraedrich et al., 2005c; Bordi et al., 2007), climate change (Lunkeit et al., 1998), tracer studies (Bagliani et al., 2000), chaotic synchronisation experiments Lunkeit (2001), to applications on Mars (Segschneider et al., 2005) and Titan (Grieger et al., 2004).

[1]The model is available for download at `http://www.mi.uni-hamburg.de/PUMA.215.0.html`

### 2.1.1 Model equations

The model equations are the Primitive Equations. They are non-dimensional equations of motion for an inviscid, adiabatic, hydrostatic perfect gas surrounding a rotating, spherical planet. See table 2.1 for the de-dimensionalisation constants. There are four prognostic equations for vorticity $\zeta$, divergence $D$, temperature $\mathcal{T}$ and natural logarithm of surface pressure $\ln p_s$ and one diagnostic equation for geopotential $\Phi$ (hydrostatic equation):

$$\frac{\partial \zeta}{\partial t} = \frac{1}{1-\mu^2}\frac{\partial}{\partial \lambda}\mathcal{F}_V - \frac{\partial}{\partial \mu}\mathcal{F}_U \tag{2.1}$$

$$\frac{\partial D}{\partial t} = \frac{1}{1-\mu^2}\frac{\partial}{\partial \lambda}\mathcal{F}_U + \frac{\partial}{\partial \mu}\mathcal{F}_V - \nabla^2\left(\frac{U^2+V^2}{2(1-\mu^2)} + \Phi + \bar{T}\ln p_*\right) \tag{2.2}$$

$$\frac{\partial T}{\partial t} = -\frac{1}{1-\mu^2}\frac{\partial}{\partial \lambda}(UT') - \frac{\partial}{\partial \mu}(VT') + DT' - \dot{\sigma}\frac{\partial T}{\partial \sigma} + \kappa\frac{T\dot{p}}{p} \tag{2.3}$$

$$\frac{\partial \ln p_*}{\partial t} = -\int_0^1 A d\sigma \tag{2.4}$$

$$\frac{\partial \Phi}{\partial \ln \sigma} = -T \tag{2.5}$$

$$\tag{2.6}$$

with

$$\mathcal{F}_U = V\zeta - \dot{\sigma}\frac{\partial U}{\partial \sigma} - T'\frac{\partial \ln p_*}{\partial \lambda} \tag{2.7}$$

$$\mathcal{F}_V = -U\zeta - \dot{\sigma}\frac{\partial V}{\partial \sigma} - T'(1-\mu^2)\frac{\partial \ln p_*}{\partial \lambda} \tag{2.8}$$

$$A = D + \mathbf{V}.\nabla \ln p_* \tag{2.9}$$

$$\text{and horiz. advect. op. } (\mathbf{V}.\nabla) = \left(\frac{U}{1-\mu^2}\frac{\partial}{\partial \lambda} + V\frac{\partial}{\partial \mu}\right) \tag{2.10}$$

$$\dot{\sigma} = \sigma\int_0^1 A d\sigma - \frac{1}{\sigma}\int_0^\sigma A d\sigma \tag{2.11}$$

$$\dot{p} = p\left(\mathbf{V}.\nabla \ln p_* - \frac{1}{\sigma}\int_0^\sigma A d\sigma\right) \tag{2.12}$$

and the definitions $U = u\cos\theta$ and $V = v\cos\theta$ for the horizontal velocities, and $\zeta = 2\mu + \frac{1}{1-\mu^2}\frac{\partial V}{\partial \lambda} - \frac{\partial U}{\partial \mu}$ and $D = \frac{1}{1-\mu^2}\frac{\partial U}{\partial \lambda} + \frac{\partial V}{\partial \mu}$ for absolute vorticity and divergence. Furthermore $\mu = \sin\theta$ and $\sigma = p/p_*$, where $\theta$ is longitude and $p_*$ the surface pressure. The temperature is split up as $T = \bar{T}(\sigma) + T'(\lambda, \mu, \sigma)$ for the semi-implicit scheme. For details refer to Hoskins and Simmons (1975), Liakka (2006) and the *PUMA User's Guide* (Fraedrich et al., 2007).

[2]This value was used throughout this study even though it represents a pre-1900 estimate for the Northern Hemisphere. Trenberth (1981) estimates a value of 1011.0 hPa and gives a

| Quantity | Scale | Value | Source |
|---|---|---|---|
| length | $a$ | $6.371 \cdot 10^6$ m | planet radius |
| time | $\Omega^{-1}$ | 13713 s | reciprocal of planet's angular velocity |
| temperature | $a^2\Omega^2/R$ | 752 K | ($R$: gas constant for dry air) |
| pressure | $p_0$ | 101325 Pa | mean sea level pressure[2] |

Table 2.1: constants used for de-dimensionalisation

### 2.1.2 Parameterisations

In its standard configuration the model uses Newtonian cooling as a heating parameterisation and Rayleigh friction at the bottom layer. For this purpose an additional term is added to the temperature equation:

$$(\partial T/\partial t)_{diab.} = (T_R - T)/\tau_T \tag{2.13}$$

with $T$ being the model temperature and $T_R$ the relaxation temperature. Note that the model is relatively free in its response to this forcing the strength of which is modulated by the time constant $\tau_T$. Usually advective processes lead to substantial differences between the relaxation temperature and the long term mean of the model temperature $T$. The parameterisation for the Rayleigh friction is similar, with a time constant $\tau_{frc}$, except that the relaxation "field" is the planetary vorticity. To increase the numeric stability of the model a hyper-diffusion is applied to fields of motion and temperature. It has the shape of $\nabla^{2n}$ with 4 being a typical choice for $n$. It has an associated time constant $\tau_H$. This configuration corresponds to the setup for the intercomparison of *dynamical cores* proposed by Held and Suarez (1994). These three time constants are the three model parameters for which the derivative is computed in section 3.2, while section 3.3 explores an assimilation scheme for the relaxation temperature $T_R$ when the mean of $T$ is given. For chapter 4 the relaxation temperature $T_R$ is not used. Instead, a fixed forcing term is used in the tendencies of all model fields in a manner similar to Hall (2000).

## 2.2 The adjoint of the atmospheric model

The adjoint with respect to initial conditions and forcings has been generated with the aid of the **T**angent-linear and **A**djoint **M**odel **C**ompiler (TAMC, Giering and Kaminski 1998). To aid the automatic differentiation, careful examination of the model code was necessary a few examples of which are given in this section.

historical overview. See Trenberth and Smith (2005) for a recent update. The implications for the results of this study are expected to be negligible.

### 2.2.1 Alterations and special directives

The adjoint of the spectral transformation was generated by hand, since in principle the operator for the Fourier transform is unitary, *i.e.* $\mathbf{S}^* = \mathbf{S}^{-1}$. In PUMA, however, the transform contains a factor which had to be compensated for by providing interface routines ($\mathbf{S}^* = \lambda_{int}\mathbf{S}^{-1}$). Furthermore the computation of index variables from loop indices was made explicit, *e.g.* in the Legendre transform (compare codes in programs 2.2.1 and 2.2.2). The reason is that otherwise re-computations for the variables `jr, ji,` and `jw` would have been triggered by TAMC in order to determine their final value after execution of the nested loops. For an example of the generated adjoint model code see program 2.2.3. Since the Legendre transform is linear, a corresponding directive was passed to TAMC and no special tangent-linear code was generated for this routine. Instead, the tangent-linear model calls the routine twice, once for the computation of the reference trajectory (unperturbed model) and a second time to compute the evolution of the perturbed quantities. The same occurs for the aforementioned case of the Fourier transform, where the adjoint routine already exists in the full model.

### 2.2.2 Reference trajectory handling

Furthermore the position in the code had to be identified in which variables needed as reference values had to be saved. Even though TAMC comes with a storage library and supports the insertion of appropriate code, a different way was chosen, which allowed for holding only parts of the total reference trajectory in memory (see scheme in appendix B.3) and the required code was developed. Reference values are stored in spectral representation and their gridpoint representation is recomputed during the adjoint model run. For the data processed for the investigations described in chapter 4 the following solution was found to provide the reference trajectory: first, daily values are provided as data file. From these the reference trajectory is interpolated to Fortran *scratch files*, providing different reference fields for every time step.

### 2.2.3 Customisation

The resulting derivative code was modified by hand in order to receive output for intermediate time steps and sensitivities with respect to derived quantities. A set of routines was developed for the convenient input and output of trajectory, target pattern, and adjoint quantities to and from the adjoint model. This functionality is described in appendix B. Details for the use of geopotential height as target pattern are given in section 4.2.2. How to obtain the derivative with respect to isentropic potential vorticity is explained in appendix A.

For other purposes not described in this work, such as SVD-computations, it was necessary to produce pure tangent-linear code, which does not compute

**Program 2.2.1** Indirect Legendre transform with implicit computation of vector indices (`jw, jr, ji`).

```
      subroutine sp2fc(psp,pfc,pol)
      use pumamod
      implicit none
      REAL pol(NLPP,NCSP)
      REAL psp(2,NESP/2)
      REAL pfc(NLON,NLPP)
      REAL zr,zi
      pfc = 0.0
      jw = 1
      jr = 1
      ji = 2
      do jm = 0 , NTRU
         do jn = jm , NTRU
            zr = psp(1,jw)
            zi = psp(2,jw)
            do jt = 1 , NLPP
               pfc(jr,jt) = pfc(jr,jt) + pol(jt,jw) * zr
               pfc(ji,jt) = pfc(ji,jt) + pol(jt,jw) * zi
            end do ! jt
            jw = jw + 1
         end do ! jn
         jr = jr + 2
         ji = ji + 2
      end do ! jm
      return
      end
```

**Program 2.2.2** Changed indirect Legendre transform with explicit dependence of vector indices `jw, jr, ji` on loop counters `jn, jm`.

```
subroutine sp2fc(psp,pfc,pol)
use pumamod
implicit none
REAL pol(NLPP,NCSP)
REAL psp(2,NESP/2)
REAL pfc(NLON,NLPP)
REAL zr,zi
pfc = 0.0
do jm = 0 , NTRU
   jr=2*jm+1
   ji=2*jm+2
   do jn = jm , NTRU
      jw=jn+jm*ntru-((jm-1)*jm)/2+1
      zr = psp(1,jw)
      zi = psp(2,jw)
      do jt = 1 , NLPP
         pfc(jr,jt) = pfc(jr,jt) + pol(jt,jw) * zr
         pfc(ji,jt) = pfc(ji,jt) + pol(jt,jw) * zi
      end do ! jt
   end do ! jn
end do ! jm
return
end
```

**Program 2.2.3** Adjoint of program 2.2.2, automatically generated with TAMC (comments manually compacted for ease of presentation). Adjoint variables are prefixed with "ad".

```
      subroutine adsp2fc( pol, adpsp, adpfc )
C*****************************************************************
C*****************************************************************
C** This routine was generated by the                           **
C** Tangent linear and Adjoint Model Compiler,  TAMC 5.3.2     **
C*****************************************************************
C*****************************************************************
      use pumamod
      use adpumamod
      implicit none
C define arguments
      REAL adpfc(nlon,nlat)
      REAL adpsp(2,nrsp/2)
      REAL pol(nlat,ncsp)
C define local variables
      REAL adzi
      REAL adzr
      integer ji
      integer jm
      integer jn
      integer jr
      integer jt
      integer jw
C RESET LOCAL ADJOINT VARIABLES
      adzi = 0.d0
      adzr = 0.d0
C ROUTINE BODY
      do jm = 0, ntru
        adzi = 0.d0
        adzr = 0.d0
        jr = 2*jm+1
        ji = 2*jm+2
        do jn = ntru, jm, -1
          jw = jn+jm*ntru-(jm-1)*jm/2+1
          do jt = 1, nlat
            adzi = adzi+adpfc(ji,jt)*pol(jt,jw)
            adzr = adzr+adpfc(jr,jt)*pol(jt,jw)
          end do
          adpsp(2,jw) = adpsp(2,jw)+adzi
          adzi = 0.d0
          adpsp(1,jw) = adpsp(1,jw)+adzr
          adzr = 0.d0
        end do
      end do
      adpfc = 0.d0
      end subroutine adsp2fc
```

its own reference trajectory, but reads it from a file. The reason is, that the reference trajectory stays the same during repeated calls of the combined operator $\mathbf{R}^\star\mathbf{R}$ (compare section 1.3.3).

## 2.3 Testing of the adjoint model

The first test for a tangent-linear as well as an adjoint model is the comparison to gradients computed with finite differences. This test was helpful in the development stage of the adjoint model to identify errors (Blessing 2000). See the tests applied in section 3.2.3, where it is carried out for the special case of the model taken to map three of these process parameters to a cost function measuring mean temperature difference.
The most common test for the adjointness of the adjoint code is the identity from Eq. (1.1). The test ensures that the adjoint actually is the adjoint of the tangent-linear model. This also has been satisfactorily tested during the development stage of the adjoint model. An even more rigorous test for this is the comparison of the gradients computed by the adjoint model and the tangent-linear model by numerically extracting the propagator matrix from both models for each forecast time step. Tab. 2.2 shows the resulting deviations of the entries of the propagator matrix $a_{ij} = (A)_{ij}$ and the adjoint propagator matrix from the adjoint model $b_{ji} = (B)_{ji}$ for a resting and a dynamic atmosphere.

The relatively small gain of precision for computations with doubled floating

| floating point precision [Byte] | 4 | | 8 | |
|---|---|---|---|---|
| smallest mantissa | $1.2 \cdot 10^{-7}$ | | $4.5 \cdot 10^{-16}$ | |
| number of time steps | 1 | 10 | 1 | 10 |
| resting atmosphere: | | | | |
| $\max_{i,j} \lvert a_{ij} - b_{ji} \rvert$ | $1.9 \cdot 10^{-6}$ | $1.1 \cdot 10^{-5}$ | $4.9 \cdot 10^{-8}$ | $6.9 \cdot 10^{-6}$ |
| $\frac{1}{NM} \sum_{i,j=1}^{N,M} \lvert a_{ij} - b_{ji} \rvert$ | $9.1 \cdot 10^{-10}$ | $2.0 \cdot 10^{-9}$ | $1.5 \cdot 10^{-12}$ | $3.3 \cdot 10^{-10}$ |
| $\frac{1}{NM} \sum_{i,j=1}^{N,M} \lvert a_{ij} \rvert$ | $3.0 \cdot 10^{-4}$ | $8.2 \cdot 10^{-5}$ | $3.0 \cdot 10^{-4}$ | $8.2 \cdot 10^{-5}$ |
| dynamic atmosphere: | | | | |
| $\max_{i,j} \lvert a_{ij} - b_{ji} \rvert$ | $3.8 \cdot 10^{-6}$ | $3.1 \cdot 10^{-5}$ | $1.7 \cdot 10^{-7}$ | $1.3 \cdot 10^{-5}$ |
| $\frac{1}{NM} \sum_{i,j=1}^{N,M} \lvert a_{ij} - b_{ji} \rvert$ | $2.2 \cdot 10^{-10}$ | $7.2 \cdot 10^{-9}$ | $3.1 \cdot 10^{-12}$ | $7.5 \cdot 10^{-10}$ |
| $\frac{1}{NM} \sum_{i,j=1}^{N,M} \lvert a_{ij} \rvert$ | $3.0 \cdot 10^{-4}$ | $3.1 \cdot 10^{-4}$ | $3.0 \cdot 10^{-4}$ | $3.1 \cdot 10^{-4}$ |

Table 2.2: consistency of tangent-linear and adjoint model for resting and dynamic atmosphere.

point precision is striking. A hypothetical explanation could be the use of fixed precision parameters in a portion of the model that has been adjoint in an analytical way rather than the line-by-line technique which has been adopted for most portions. This indeed is the case with the Fourier transform in the model,

which is making use of the fact that the direct transform is the adjoint of the indirect transform (and vice versa) but this part is not depending on fixed precision parameters, as e.g. the Bessel functions which in the model are given with ten digits after the comma. Therefore this is not an explanation. Nonetheless the differences are relatively small and there is some gain of precision, which reduces the probability of a systematic error. Errico (2004, personal communication) gives nine identical digits with eight Byte precision. Taking into account that the diagonal elements of the matrix are close to unity, this corresponds reasonably well with the maximal absolute deviation of $4.9 \cdot 10^{-8}$ from Tab. 2.2. Further tests are the test of the linearisation against finite differences approximations of the gradient as shown in section 3.2.3 and in Fig. 3.12.

# Chapter 3

# Sensitivities in an atmospheric GCM

In this chapter the theoretical concepts of the preceding chapter are tested in the context of the atmospheric global circulation model PUMA introduced in section 2.2. Section 3.1 gives an overview of reference trajectory, target pattern, propagator and sensitivities for the PUMA model for the setting of the sensitivity of a projection index on an initial state perturbation. Section 3.2 explores the timescale on which the gradient of a cost function with respect to a model parameter can be determined with the adjoint method. Section 3.3 uses climate sensitivities computed with an averaging method to recover the parameter field of the heating relaxation which produces a given climate.

## 3.1 Sensitivities to an initial state

As an instructive example for the computation of derivatives with the adjoint model, Fig. 3.1 shows the elements involved when a projection index is differentiated with respect to initial model conditions. First a projection index is defined by projecting the deviation of the model state from its long-time mean onto the dipole pattern shown in the upper left panel. Part (a) of the figure shows a clipping of the time evolution of this index from an ordinary model run. The colour shading in the two maps located above two distinct days (c: "May 14" and d: "May 24") of this index plot show the respective model state in terms of vertically averaged streamfunction deviations from the long-term mean. We choose "May 24" to be "verification time" and "May 14" to be "initial time". The vertical axis of the blue panel (labelled e) indicates the lag or lead time for the derivative of the projection index (difference between verification and initial date). The derivative or sensitivity of the index with respect to a streamfunction perturbation is indicated as green contours in the "weather" maps for "May 14" (initial, c) and "May 24" (verification, d). In the "May 24"-map they represent

the sensitivity for zero lead-time (as if this was initial and verification time at once). This is equivalent to the derivative of the projection index with respect to model output and consequently reflects the shape of the pattern projected on. In the "May 14"-map the sensitivity for a 10-day lead time is shown. This is the derivative of the "May 24"-index with respect to "May 14"-initial conditions. Since this is computed with the knowledge of the unperturbed development, *i.e.* in a tangent-linear sense, it is the precise first derivative of these quantities in the given model. Finally, the blue shading shows for each combination of verification and lead time the norm of the sensitivity. Low sensitivity has been equated to good predictability while high sensitivity corresponds to low predictability. In this sense the "May 24"-maximum of the index (a) )would have been relatively well predictable (only slow growth of sensitivity norm with increasing lead time in panel e for "May 24"), while, the index state on "May 17" and "May 22" appear to be relatively uncertain to predict, judging from the two flame-like features in panel (e). As before, in the similar representation of sensitivities in the Lorenz'63 model (Fig. 1.2), predictability seems to be strongly linked to the state at verification time and less to the trajectory sections passed, or the impact of the trajectory on the sensitivities is very time critical.

## 3.2 Sensitivity of the model climate to a parameter

In this section a feasibility study for a Climate Prediction Data Assimilation System is presented. The usefulness of accurate gradient information for estimating process parameters of the spectral atmospheric circulation model `PUMA` on climate time-scales is investigated. Pseudo observations of the long-term mean surface temperature are generated by the model itself. The gradient of the model-data misfit computed by the tangent linear version of the model provides a good approximation for integration periods of 10 days and one year. In an identical twin experiment the correct parameter values can be retrieved by variational assimilation of the pseudo observations for an integration period of 10 days. For an integration period of 100 days this works after adding pseudo observations of the seasonality of the surface temperature.

### 3.2.1 Introduction

State of the art climate predictions rely on numerical models of the earth system. One of the major sources of uncertainty in these predictions is the correct representation and parametrisation of the processes underlying the climate system (Cubasch et al., 2001; Prentice et al., 2001). Due to their high complexity, state of the art earth system models are extremely demanding in terms of computer

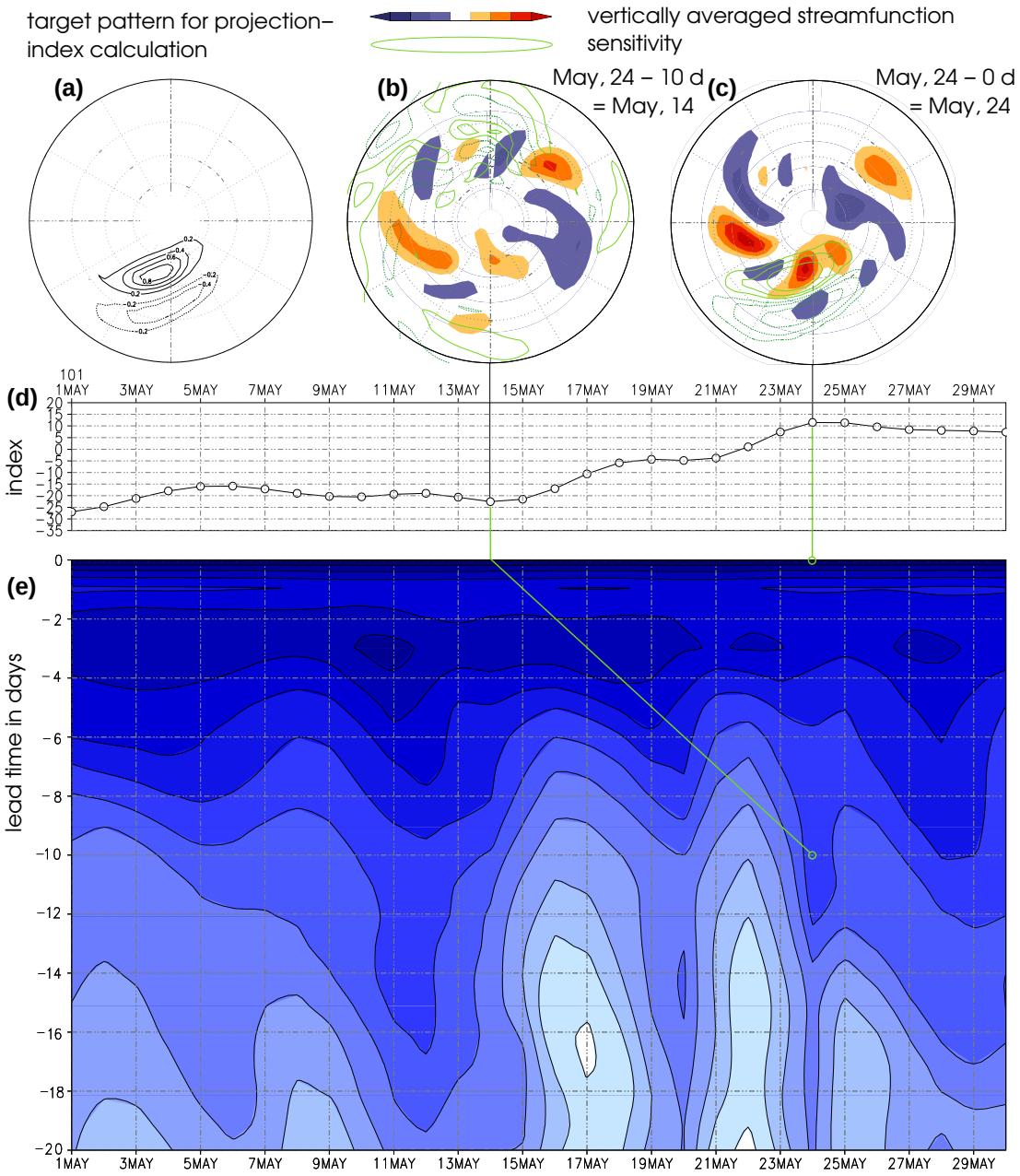


Figure 3.1: Schematic illustration of sensitivity calculation in an idealised PUMA experiment. **(a)** Target pattern to define projection index, **(b)** time series of projection index, **(c)** exemplary vertically averaged streamfunction anomaly on "May 14" (colour shading) and 10-day lead sensitivity of projection index for verification time "May 24" (green contours), **(d)** as (c) but on "May 24" and 0-day lead sensitivity, **(e)** norm of sensitivity for all combinations of lead and verification time (logarithmic colour scale from dark blue=low to bright=high).

time. This complicates both the systematic estimation (or calibration) of process parameters from observations (so-called model tuning) and the systematic assessment of the associated uncertainty in predictions.

These systematic approaches can, thus, typically only be pursued for models with reduced spatio-temporal resolution, simplified process representations, and/or reduced sets of uncertain (tunable) parameters. For instance, Jones et al. (2005) employ FAMOUS, a reduced resolution version of its parent general circulation model HadCM3 to demonstrate the systematic tuning of eight process parameters. This subset of the full parameter space, which for the atmosphere component alone has about 100 dimensions (Murphy et al., 2004), was kept small for computational reasons. This is because they approximate the gradient information in the optimisation procedure by finite differences of model runs, at a cost proportional to the number of tunable process parameters. Similarly, Murphy et al. (2004) demonstrate a systematic quantification of the uncertainty on model predictions associated with the uncertainty in 29 of the model's process parameters. Their reason for the restricted parameter space is also of computational nature, imposed by an algorithm which uses finite differences of model runs. Kunz (2003, 2007) scans the entire space of process parameters for `PUMA`, the model used in this study, in a simple but expensive procedure.

For both applications, model tuning and uncertainty assessment, the use of adjoint parameter sensitivities avoids restrictions of the parameter space. For the terrestrial biosphere component of the climate system this approach is demonstrated by the Carbon Cycle Data Assimilation System (CCDAS, Scholze, 2003; Rayner et al., 2005; Scholze et al., 2007).

The construction of an assimilation system around a coupled climate model, in what follows called CPDAS (Climate Prediction Data Assimilation System), is both tempting and challenging. It is tempting, because it would allow to employ, for instance, observational paleo records as a constraint on the process parameters of the underlying climate model. Furthermore, the impact of all process parameters and boundary conditions on the model's climate sensitivity could be rigorously assessed in a single adjoint run. Typically, such an assessment is done by perturbing one parameter at a time (Murphy et al., 2004) or by Monte Carlo simulations (Stainforth et al., 2005), at a computational cost proportional to the ensemble size.

One of the associated challenges is imposed by the code size of a coupled climate model. A number of examples, however, demonstrate the applicability of TAF (or its predecessor TAMC) to large codes representing components of the climate system, such as the atmospheric general circulation models MM5 (Nehrkorn et al., 2002), WRF (Xiao et al., 2005a), ARPS (Xiao et al., 2005b) and fvGCM (Giering et al., 2005) , or the oceanic general circulation models MITgcm (Marotzke et al., 1999; Heimbach et al., 2002), HOPE (van Oldenborgh et al., 1999; Junge and Haine, 2001), and MOM3 (Galanti et al., 2002).

As described in section 1.4, a more fundamental challenge results from the

non-linearity of the climate system. The usefulness of derivative code depends on the capability of the linearisation around a point to represent the model in the point's neighbourhood. This capability is closely connected to the concept of predictability, which Lorenz (1963) analysed for a non-linear three-dimensional system that possesses a strange attractor. Lea et al. (2000) use this system to demonstrate that the usefulness of the linearisation of the long-term mean state around the system's parameters decreases with increasing integration period. Köhl and Willebrand (2002) analyse how this affects the parameter estimation from the long-term mean state via a gradient method for the same model as well as for a high-resolution quasi-geostrophic model. In this estimation context, the poor linearisability of the long-term mean shows up in the form of multiple local minima in the model-data misfit. Pires et al. (1996) using the Lorenz model and Tanguay et al. (1995) using a $\beta$-plane model address the linearisation problem in the context of four-dimensional variational data assimilation, estimating initial conditions that minimise the model-data misfit. Lorenc (2006) presents a summary of the linearisation topic, together with a sketch of a four-dimensional variational assimilation system, which models probability density functions for the uncertain, small-scale processes.

This section examines the feasibility of a CPDAS in the light of the linearisation problem. For the ocean component the feasibility has been demonstrated by the ECCO project Stammer et al. (2002), and for the terrestrial component by the Carbon Cycle Data Assimilation System. Hence, the focus on the atmospheric component. Section 3.2.3 investigates, for time scales of up to one year, the validity range of the model's linearisation with respect to three process parameters. If the linearisation was not valid even in a small neighbourhood of the linearisation point, a gradient based optimisation environment could not even find a local minimum of the model-data misfit. Although the model-data misfit is used as target quantity, this is primarily a test of the model. The next experiment Section 3.2.4, in contrast, tests the combination of model and observing system. In a so-called identical twin setup, an attempt is made to recover the values of the three process parameters from (pseudo)-observations that have been generated by the model itself. Since, as mentioned above, model calibration from the paleo record is a tempting perspective, such observation systems are deliberately selected that mimic the paleo record. Section 3.2.5 lists a few conclusions.

### 3.2.2 Model and Parameters

Regarding the feasibility of a CPDAS, `PUMA` is particularly interesting, because it is the atmospheric component of the Planet Simulator (Fraedrich et al., 2005a,b), a coupled climate model designed for long integration periods, and also one of the available atmospheric modules in the coupled climate model BREMIC (Lohmann et al., 2003).

PUMA is introduced in section 2.1. It is a primitive equations model of the global atmospheric circulation. Although many of the process representations are simplified, PUMA simulates atmospheric key processes, for instance storm tracks (Frisius et al., 1998) by means of a prescribed heating relaxation (see section 2.1 for details). A model setup with 64 × 32 grid cells in the horizontal domain (T21 in spectral space), 5 vertical levels, and a time step of 1 hour is used. This setup does not contain orography nor a hydrological cycle or land-sea differences. Lacking a representation of direct solar heating, the model induces a heating dipole by relaxation against a prescribed temperature field. In Figure 3.2 the relevant information is therefore just the relative location of the storm tracks (shown as standard deviation of 500 hPa height) with regard to the prescribed heating. The heating relaxation and, thus, the temperature, have no seasonality.

Three tuning parameters have been selected. The first parameter is the relaxation time scale of the heating. The second and the third parameter influence the model's friction and diffusion schemes, respectively. Kunz (2003, 2007) gives a detailed description of the parameters and schemes and estimates the parameters in a simple but expensive procedure that scans the entire parameter space.

In view of parameter estimation from the paleo record, the long-term mean temperature over the integration period at each surface grid cell was selected as observed quantity, i.e. there are 64 × 32 observations. The model $M$ was set up such that it directly produces this quantity as output. A vector of pseudo observations, $d$, are generated and recorded by running the model, $M(x)$, with the standard values of the parameters, $x_{opt}$, forward in time, i.e.

$$d = M(x_{opt}) \ . \tag{3.1}$$

For a given set of parameter values, $x$, the misfit of the model simulation and the data can then be quantified by the cost function

$$J(x) = \frac{1}{2}((M(x) - d)^T \, \mathbf{C}_d{}^{-1} \, (M(x) - d)) \ , \tag{3.2}$$

where, for convenience, $\mathbf{C}_d$, which expresses the combined uncertainty from model and observational error, is the identity.

Tangent linear and adjoint versions of the model had been generated in (Blessing, 2000; Blessing et al., 2004) by means of TAF's predecessor TAMC. These codes were generated to evaluate derivatives of the final state with respect to the initial state and not with respect to the process parameters. Hence, the model code was rearranged for the purpose of this section to express the mapping of the three tuning parameters on the cost function in a TAF-compliant way. A vectorial version of the tangent linear model (TLM), simultaneously evaluating the derivative of the cost function with respect to the three parameters, was generated by TAF.

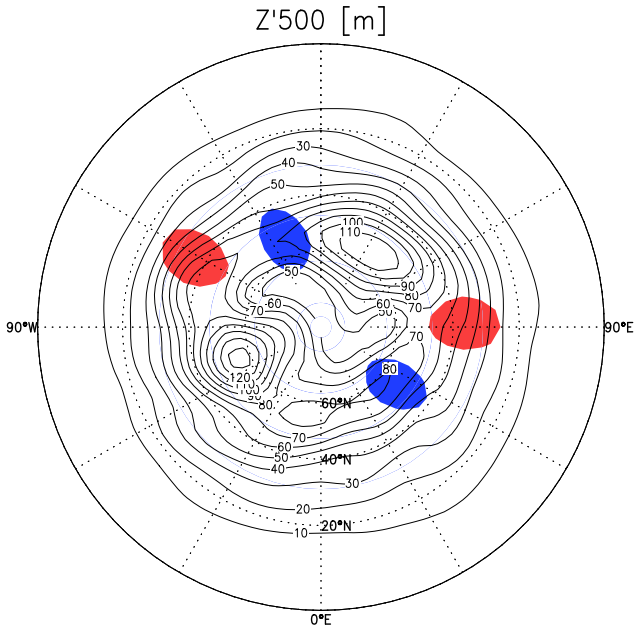


Figure 3.2: Standard deviation of 500 hPa geopotential height [m] in a year-long integration of the PUMA setup with two heating dipoles. The maxima of the contours indicate the location of the simulated storm tracks on the Northern Hemisphere. The light and dark shading mark the maxima (325 K) and minima (215 K), respectively, of the relaxation temperature field. Due to the setup without orography the longitudinal position is arbitrary but the distance of 150° is most effective to approximate observed variability (Franzke et al., 2000).

### 3.2.3 Finite Difference Tests

Before addressing the parameter estimation problem, the linearisability of the model around a base point $x_0$ in parameter space is investigated. Regarding the selection of the base point, the point $x_{opt}$ is avoided, at which the pseudo observations have been generated (see Eq. (3.1)). Being the global minimum of the cost function with zero gradient, $x_{opt}$ is a special point. Instead, a generic base point is constructed by adding a relative perturbation of 0.5 to each parameter value, i.e.

$$x_0 = (1 + 0.5)x_{opt} \quad . \tag{3.3}$$

First an integration period of 10 days is used. Figure 3.3 shows both the cost function and its linearisation around the base point over the relative perturbation size. Both functions are evaluated for 14 perturbations with relative sizes ranging from $10^{-13}$ to 1. For relative perturbation sizes up to 0.1 the agreement is excellent. Another way of quantifying the usefulness of the linearisation is to plot the difference between the derivative provided by the TLM against its approximation by finite differences:

$$fd(x_0, \epsilon) = \frac{J(x_0 + \epsilon) - J(x_0)}{\epsilon} \quad . \tag{3.4}$$

The norm of this difference is shown in Figure 3.3, for parameter perturbations, $\epsilon$, spanning several orders of magnitude. For very small perturbations the accuracy of the finite difference approximation is low due to rounding error. For large perturbations the effect of quadratic and higher order terms in the Taylor expansion becomes visible, i.e. the non-linearity of the model. In between there is a range of good agreement, which strongly supports the correctness of the TLM and also demonstrates the smoothness of the cost function.

Figure 3.4 shows the same quantities for a 1-year integration. Compared to the 10-day integration the non-linearity has increased, but nevertheless, the function is still reasonably smooth.

### 3.2.4 Parameter Estimation

The previous section demonstrated that the model is linearisable with good accuracy. The experiments in this section investigate the model's behaviour in an iterative optimisation procedure for parameter estimation. The cost function (see Eq. (3.2)) introduced in section 3.2.2 is used, which is based on the pseudo observations generated from the model's standard parameter values (see Eq. (3.1)). From a base point in parameter space (see Eq. (3.3)) it is aimed to reconstruct the original parameter values with an iterative gradient search algorithm (Fletcher and Powell, 1963). This type of setup is known as identical twin experiment.

Regarding the optimisation strategy, there are different options. The typical procedure in operational numerical weather prediction, known as incremental

(a)

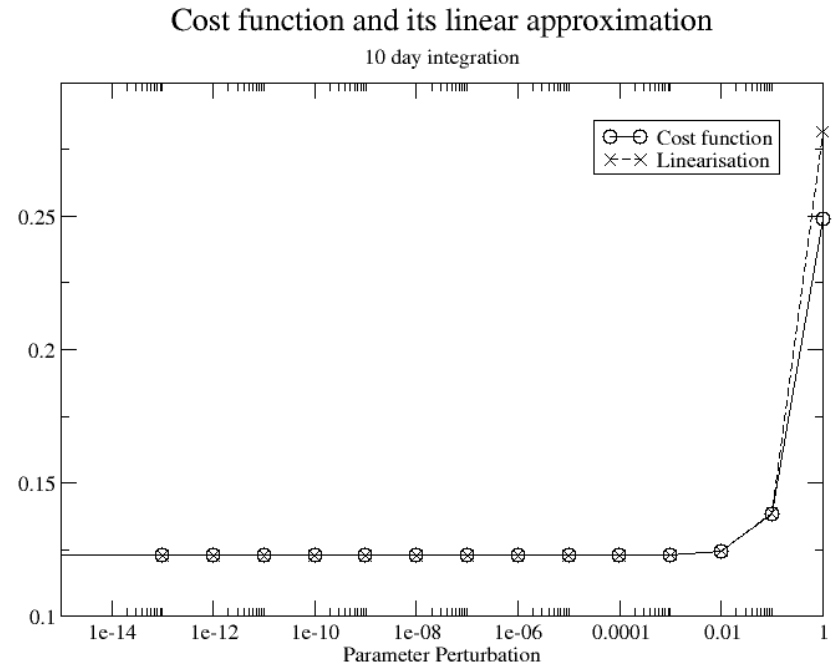


(b)

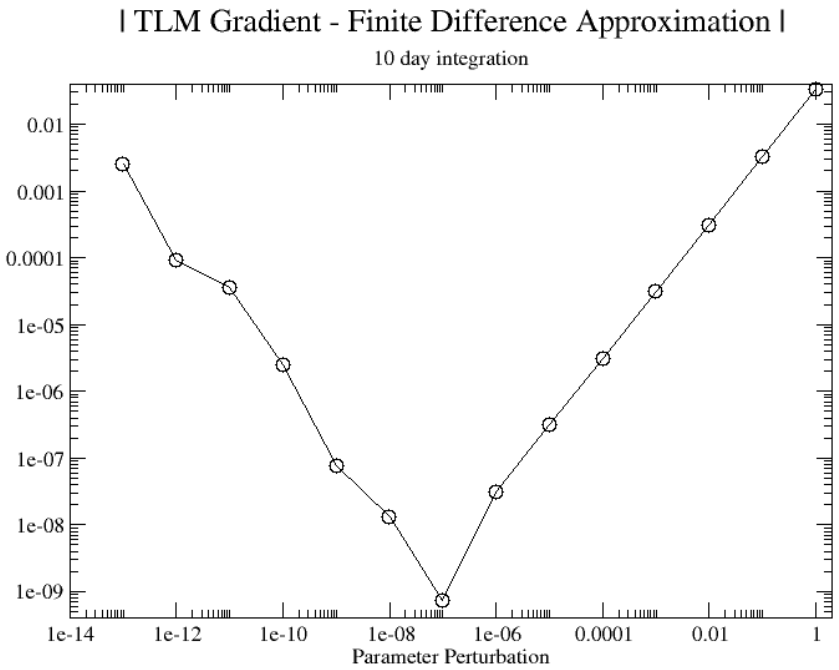


Figure 3.3: Linearisation properties for 10-day integration: **(a)** Cost function (solid) and its linearisation around the base point (dashed). **(b)** Difference between TLM and finite differences.

(a)

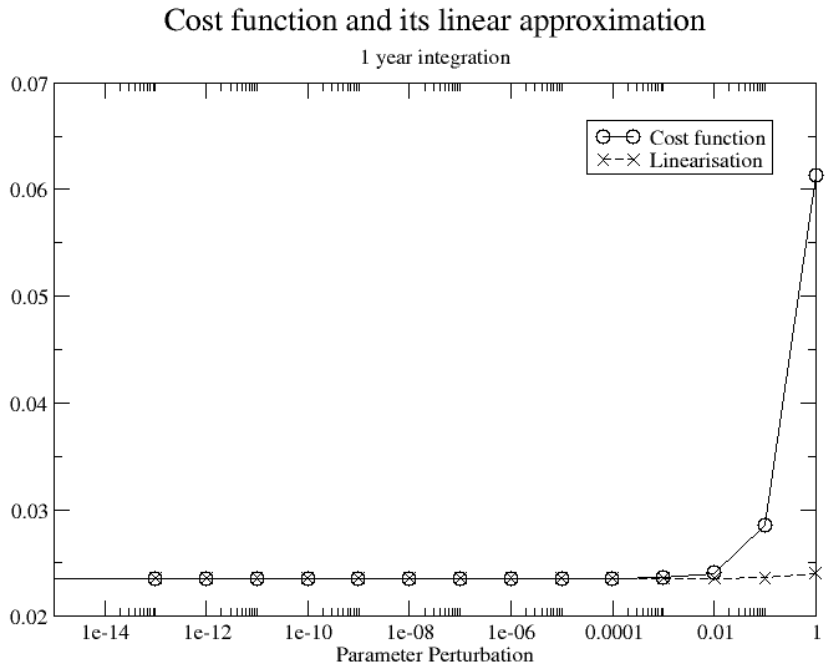


(b)

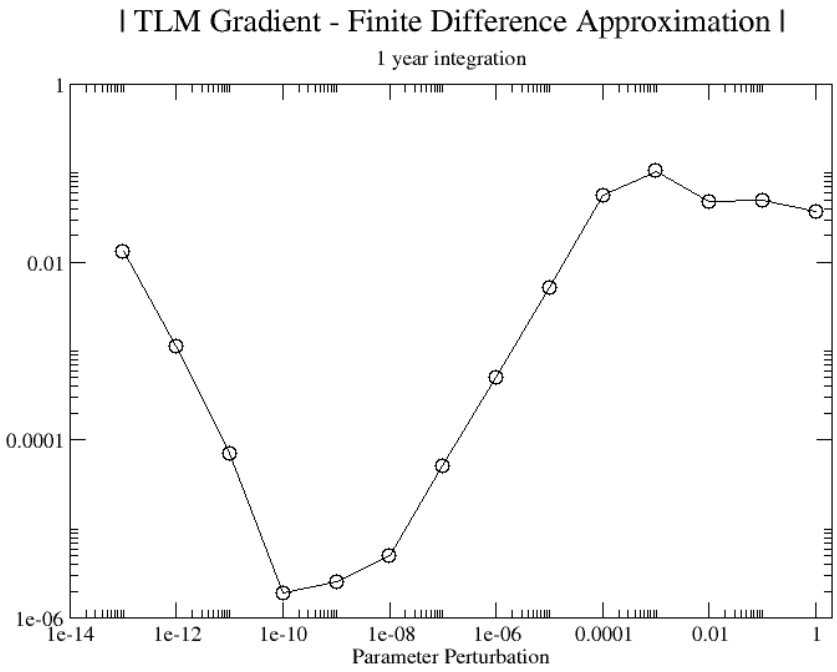


Figure 3.4: As Figure 3.3, but for 1-year integration: **(a)** Cost function (solid) and its linearisation around the base point (dash **(b)** Difference between TLM and finite differences.

4D-VAR and introduced by Courtier et al. (1994), is to solve (in a so-called outer loop) a sequence of optimisation problems. For each of these problems, a fixed linearisation point for the model is chosen and the corresponding quadratic cost function is minimised iteratively (in a so-called inner loop) by the gradient algorithm. The solution of one problem defines the linearisation point for the next problem. The advantage of this technique is that, owing to their quadratic cost functions, the individual optimisation problems cannot be trapped in secondary minima. At worst, the optimisation problem could be underdetermined, so that the global minimum is reached not only for a single point but for a set of points. But this is avoided by including prior information (a so-called background term) in the cost function. The guaranteed convergence of the individual optimisation problems is particularly useful in an operational context, with its hard time constraint.

Here, a slightly different strategy is used, which applies the gradient algorithm directly to the non-linear model. This avoids the risk of the inner loop improving only the fit to the linearised model but not to the non-linear model. Instead the gradient algorithm can benefit of an update of the linearised model in every iteration on its way to the minimum. Indeed, the experiments show that the model's linearisation with respect to process parameters changes continuously. The same approach is used in assimilation systems for other components of the climate system, e.g. in the ECCO system for the ocean (Stammer et al., 2002) and in CCDAS for the terrestrial biosphere (Scholze, 2003; Rayner et al., 2005; Scholze et al., 2007). In contrast to these systems, the experiments presented do not use any prior information on the parameters, although it stabilises the inverse problem via the convex component it adds to the cost function. This is done deliberately in these twin experiments, in order to not include the knowledge of the true parameter values in the solution process. When applying a CPDAS to real observations, one would certainly include a prior information term in the cost function.

Figure 3.5 illustrates the performance of an optimisation for an integration period of 10 days. Both the cost function and the gradient decrease over several orders of magnitude. As the observations have been generated by the model, the optimal parameter values are known. Unlike in an experiment with real observations, it is hence possible to also record, in each iteration, the distance from the optimum. The optimisation algorithm has no problem finding the optimum. Figure 3.6a shows the cost function for a section in parameter space (using relative units) through the optimal parameter value ($s = 0$) with the starting point ($s = \sqrt{3 \cdot 0.5^2}$). The function decreases by 14 orders of magnitude from the starting point of the optimisation to the minimum.

The same experiment for a 100-day integration period did not succeed in reconstructing the original parameter values. The norm of the gradient decreases by about 7 orders of magnitude, but the cost function value decreases only by one order of magnitude to about 0.002. The final parameter distance from the

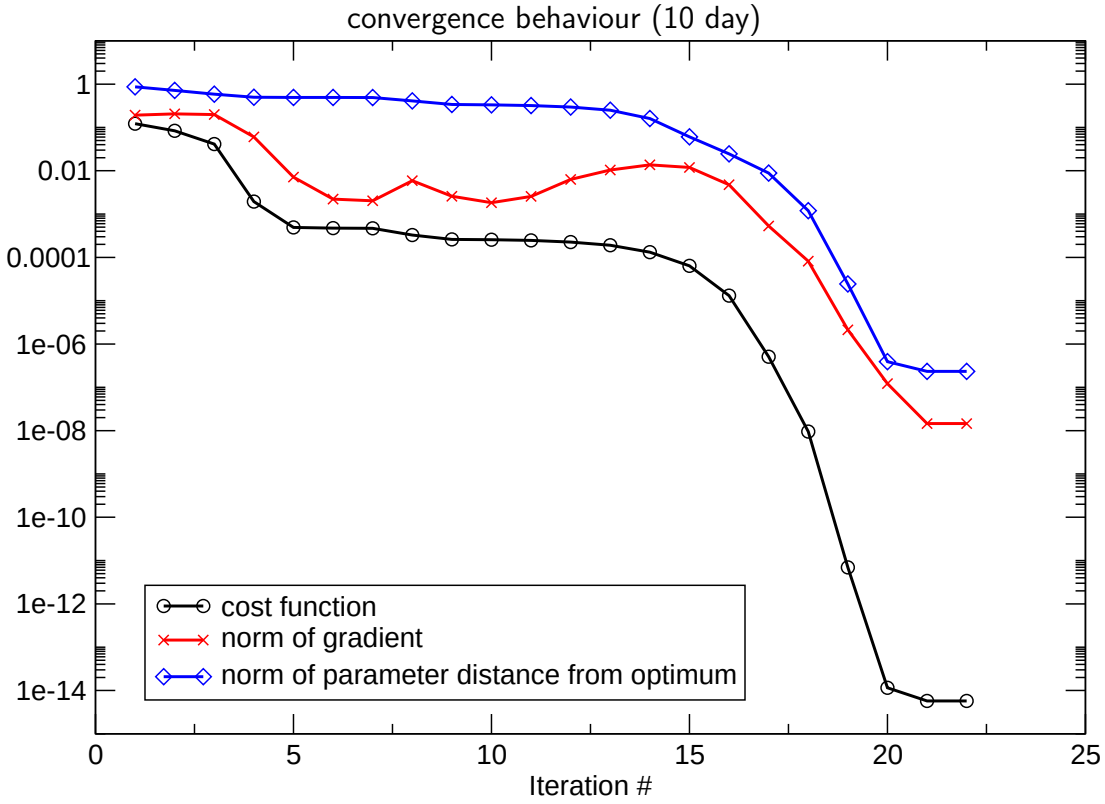


Figure 3.5: Integration period of 10 days: Various aspects of convergence behaviour of cost function, its gradient, and distance from optimum over iteration number.

(a) 10 day

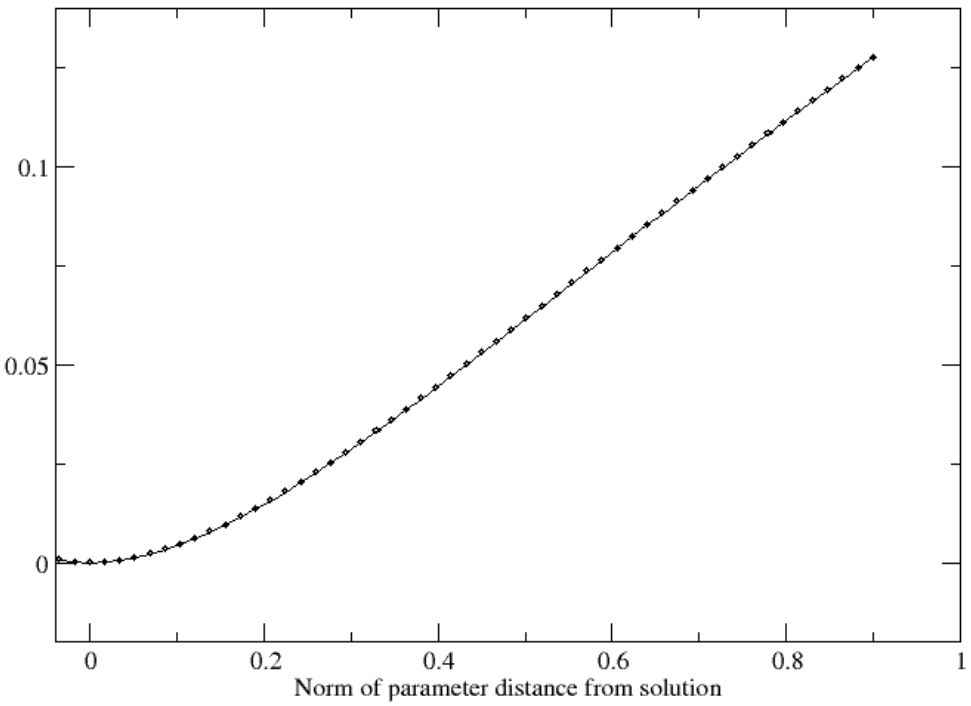


(b) 100 day

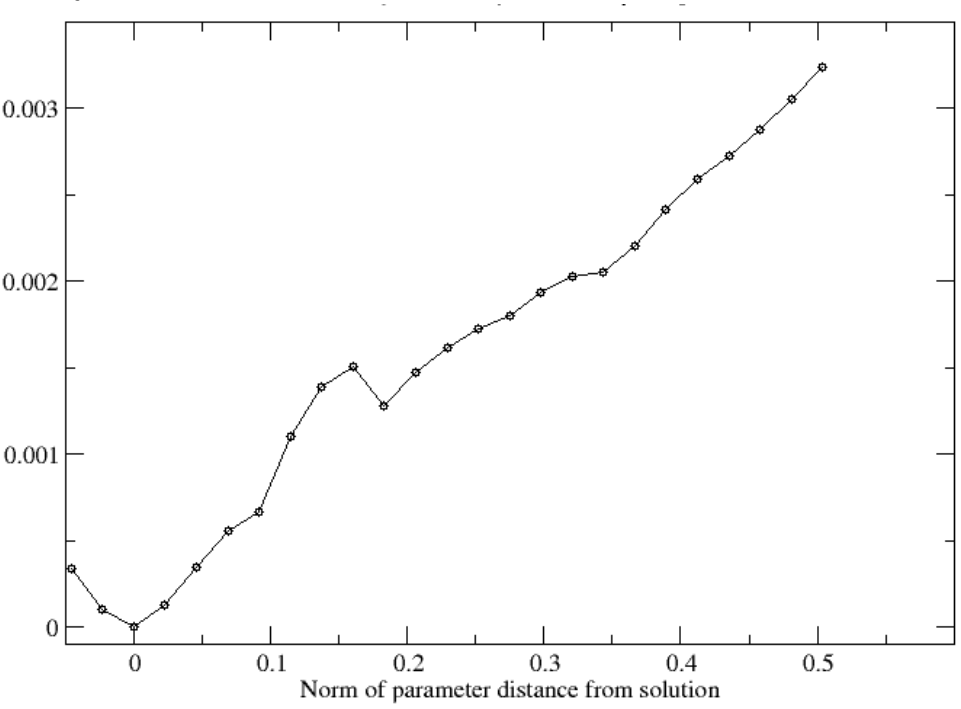


Figure 3.6: Cost function for section in parameter space. **(a)** 10 day integration period, **(b)** 100 day integration period.

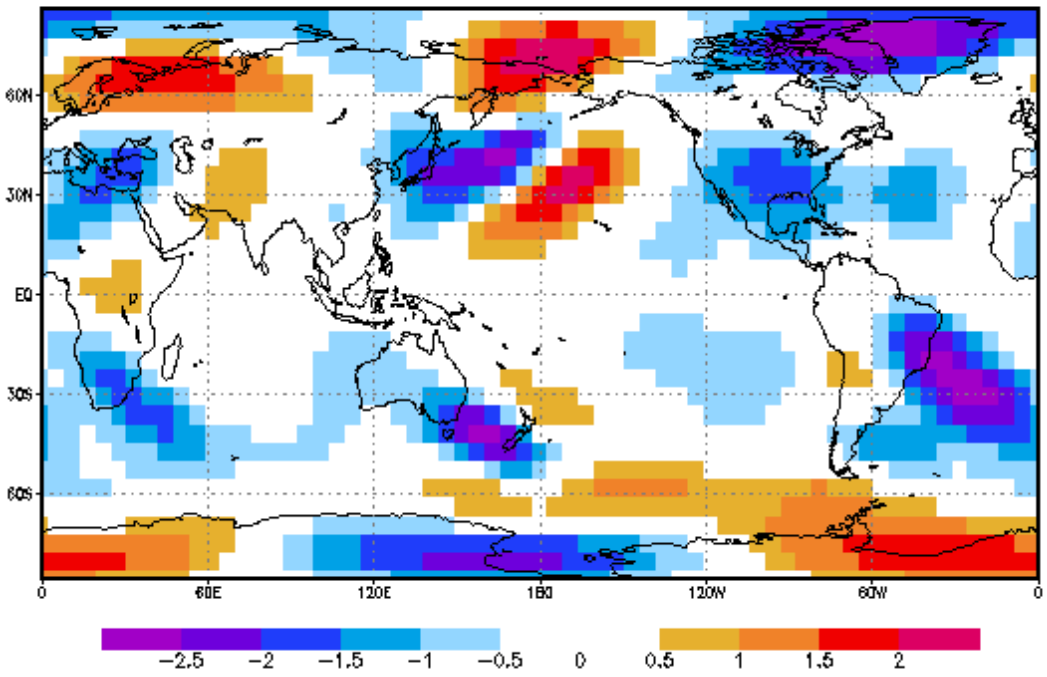


Figure 3.7: Difference in surface temperature simulated from optimal parameters (global minimum) and parameter set at local minimum of cost function, 100 day integration period.

optimum is about $s = 0.4$. Unfortunately this minimum is only a local one. The existence of local minima is supported by the section shown in Figure 3.6b. The decrease of the gradient norm suggests that the optimisation was indeed successful in finding a minimum, which is another confirmation for the usefulness (and correctness) of the gradient information discussed in section 3.2.3. Figure 3.7 shows the difference in simulated surface temperature between the local and global minima of the cost function. Interestingly, the difference also contains large-scale structure.

The constraints incorporated in the cost function are not powerful enough to render its shape more convex and avoid the optimisation's getting trapped in local minima. This problem can, however, be tackled by changing the formulation of the cost function. As mentioned above, this feasibility study for a CPDAS also aims at investigating the potential of paleo observations as data constraint. The paleo record (Boenisch et al., 2001) provided by the BIOME 6000 project, for instance, includes in addition to local annual mean temperature also information on the local seasonal cycle in temperature and moisture. Since the PUMA version under study does not include a hydrological cycle, the moisture constraint could not be included. Usage of the seasonal cycle in temperature is also limited, because the PUMA version under study is forced without seasonal cycle. Nevertheless three additional constraints are implemented on the temporal variation of the local temperature, each yielding an additional pseudo data point per surface grid cell. To emphasise the small seasonal signal, all three constraints first remove the temporal mean:

1. The variance over the integration period, i.e. for a surface grid point with coordinates $\lambda$ and $\phi$ an observation $d_{var}(\lambda, \phi)$ is produced by

$$d_{var}(\lambda,\phi) = \frac{1}{N} \sum_{i=1,N} \left[ T(\lambda,\phi,t_i) - \frac{1}{N} \sum_{j=1,N} T(\lambda,\phi,t_j) \right]^2, \tag{3.5}$$

   where $T$ denotes the temperature, $t_i$ the time in years, and $N$ the number of time steps.

2. The projection on a cosine signal with annual period, i.e.

$$\begin{aligned} d_{cosine}(\lambda,\phi) &= \frac{1}{N} \sum_{i=1,N} cos(2\pi t_i) T(\lambda,\phi,t_i) \\ &\quad - \frac{1}{N} \sum_{i=1,N} T(\lambda,\phi,t_i) \cdot \frac{1}{N} \sum_{i=1,N} cos(2\pi t_i). \end{aligned} \tag{3.6}$$

   This is the discretised form of

$$d_{cosine}(\lambda,\phi) = \int cos(2\pi t) \left( T(\lambda,\phi,t) - \bar{T}(\lambda,\phi) \right) dt, \tag{3.7}$$

where the the overlying bar denotes the average over the integration time.

3. The projection on a sine signal with annual period ($d_{sine}$).

The effect of adding various combinations of these pseudo data to the cost function is assessed, i.e. instead of Eq. (3.2) now the extended cost function

$$J_{ext} = J + \alpha_{var} J_{var} + \alpha_{cosine} J_{cosine} + \alpha_{sine} J_{sine} \tag{3.8}$$

is minimised, with different choices of the weighting factors $\alpha_{var}$, $\alpha_{cosine}$, and $\alpha_{sine}$.

Figure 3.8 shows the convergence behaviour for a cost function with the cosine and the sine constraints added to the mean constraint, all with equal weights. The optimal parameter values were reconstructed after 37 iterations. The behaviour of the individual components of the gradient and the parameter vector is shown in Figure 3.9.

Other combinations of pseudo-data were equally successful. For instance, when adding only the cosine component to the mean component, giving it ten times more weight than the cosine component, the optimisation reconstructs the optimal parameter set in 24 iterations.

Repeating the same experiment for a 1-year integration period, different combinations of cost function contributions were tested. The optimisation was, however, not able to reconstruct the optimal parameter set. Instead, it converged well (with the gradient norm reduced by 3–7 orders of magnitude) to local minima. Motivated by the structure of the difference in surface temperature simulated from the optimal parameter vector and the one in the local minimum (see Fig. 3.7) a smoothness constraint was added. To this end a corresponding contribution to the cost function was implemented as the squared difference in surface temperature between neighbouring grid cells, summed up for each pair of neighbouring cells on the horizontal grid. Activating this cost function contribution punishes small scale deviations from the (pseudo)-observed surface temperature field. Figure 3.10 shows all cost function contributions that were implemented for a section in parameter space from the optimisation's starting point to the optimal parameter value. The challenge is to compose these contributions to an over-all cost function with a shape sufficiently close to convex to avoid the optimisation's getting trapped in local minima.

### 3.2.5 Conclusions

The linearisation of the chosen cost function of three process parameters is a good approximation for integration periods of 10 days and one year. In an identical twin experiment the three parameters could be retrieved from pseudo observations of long-term mean surface temperature for integration periods of 10 days. For an integration period of 100 days this worked only after adding pseudo observations of the seasonality. For a 1-year integration period the true parameter values could

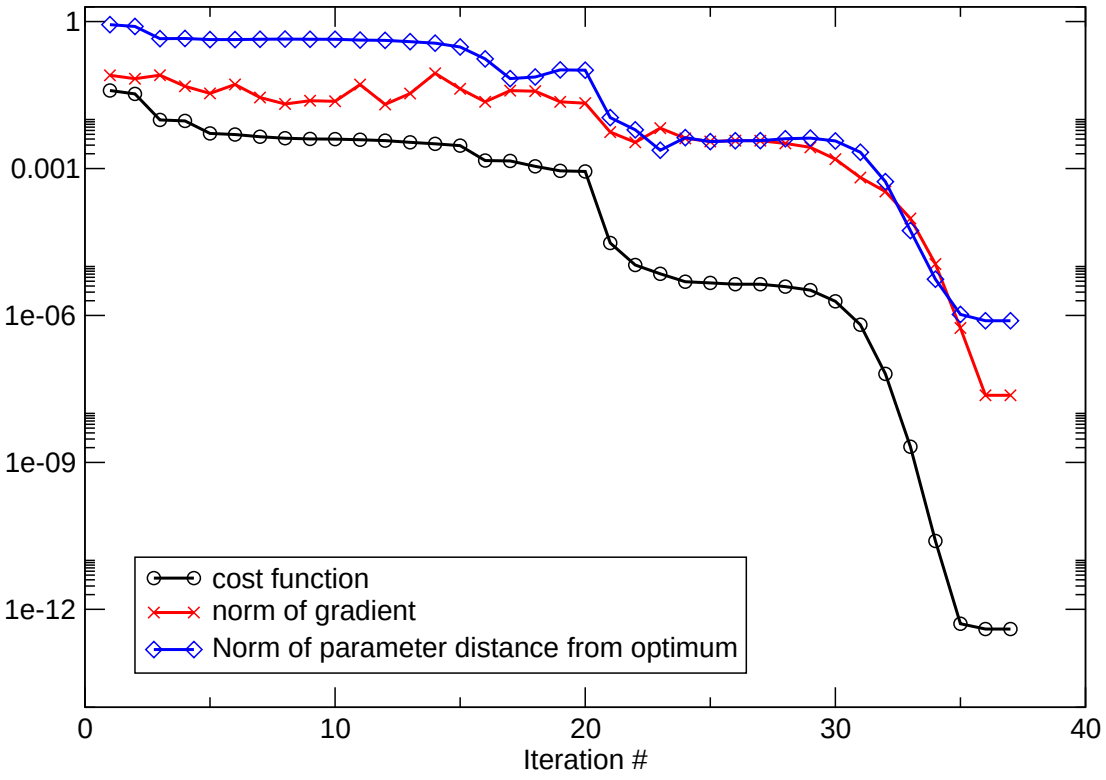


Figure 3.8: Various aspects of convergence behaviour for an integration period of 100 days: Cost function, its gradient, and distance from optimum over iteration number. Setup with cost function contributions by cosine, sine and mean components, all with equal weights.

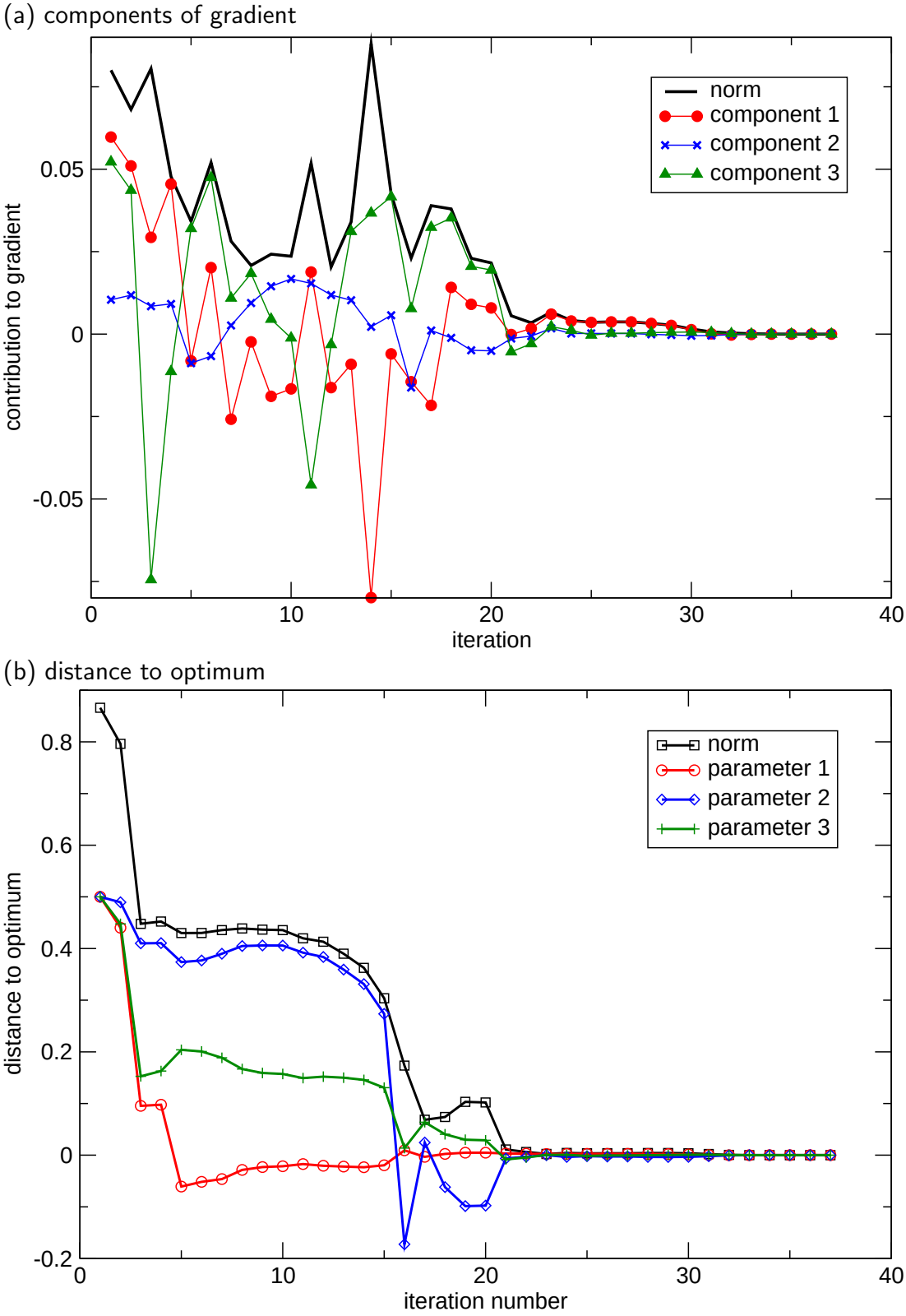


Figure 3.9: Convergence behaviour for an integration period of 100 days: **(a)** components of gradient and **(b)** distance of parameter vector to optimum. Setup with cost function contributions by cosine, sine and mean components, all with equal weights.

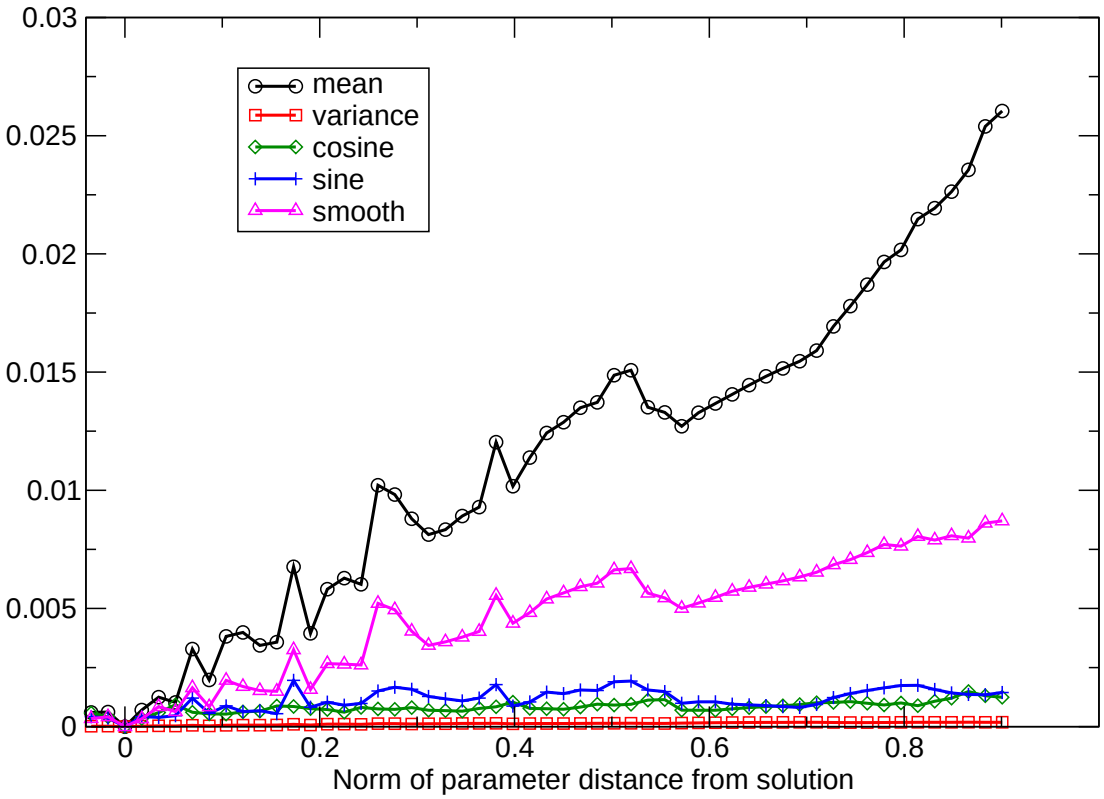


Figure 3.10: Cost function for section in parameter space. 1-year integration period.

not be retrieved. For all these integration periods, however, the optimisation algorithm has converged in only a few 10 iterations to (sometimes local) minima, with a gradient norm reduction by 3–7 orders of magnitude. This demonstrates that the gradient information provided by the linearised model has been very useful, but there were not enough observational constraints to avoid the local minima. The `PUMA` version used here had no seasonal cycle in the temperature, so that the temporal constraint was only a weak one. Furthermore, no hydrological cycle is included. The seasonality of temperature and the hydrological constraint, which are both available in observational records (both historical and paleo), are expected to have a favourable impact on the optimisation.

On purpose, an experiment setup was selected for which the optimum was known. Hence, no observational or model error were added to the observations, which are expected to complicate the parameter estimation. On the other hand no prior information was incorporated, which would have regularised the estimation problem by its quadratic contribution to the cost function and usually speeds up the estimation procedure considerably.

For the estimation a gradient approach was used in a straightforward way. Promising technical extensions such as using an averaged gradient (Lea et al., 2000), a gradient from an even coarser resolution model in grid point (Köhl and Willebrand, 2002) or spectral (Tanguay et al., 1995) space in conjunction with averaged forward integrations, or tracking the absolute minimum when extending the integration period (Pires et al., 1996, shown to be unsuccessful for the Lorenz'63-case in 1.4.1) have not been applied, nor was, in this section, the system run in an incremental mode as described by Courtier et al. (1994).

## 3.3 Assimilation of a model climate

In this section the encouraging results of the previous section are used to set up a climate assimilation system. From the technical extensions, suggested above to avoid secondary minima of the cost function and to receive meaningful gradients, the averaging method is demonstrated to be successful.

### 3.3.1 Aims and Methods

The long-term or climate mean fields are considered as the response to a forcing. In particular, changes in the climate are linked to changes in the climate forcing. Here we analyse the link from a time-mean temperature field (target climate $\overline{T}_T$ from the control run) to its forcing field. That is, a suitable forcing field is reconstructed (for example, the `PUMA` relaxation temperature $T_R$), whose time-mean response (substitute climate, $\overline{T}$) should be as close to the target climate $\overline{T}_T$, as possible. A unique forcing-response relation, however, cannot always be guaranteed as different forcings may lead to the same climate mean state.

Therefore we carry out an internal experiment in the sense that the target climate itself has been produced by the PUMA with a prescribed forcing. This allows an objective judgement of the quality of the forcing reconstruction by comparison with the known solution. For the forcing reconstruction we define a cost function $J$, which describes the distance between target and its substitute in a manner similar to the $J$ used in section 3.2:

$$J := \frac{1}{2}\left(\overline{T} - \overline{T}_T, \overline{T} - \overline{T}_T\right). \tag{3.9}$$

In the experiments discussed here the inner product $(\cdot,\cdot)$ contains area weights to compensate for the geometry of the model grid and variance scaling with the temperature variance of the control run. For the forcing reconstruction this cost function needs to be minimised by choice of appropriate parameters $T_R$ of the relaxation temperature. The gradients of $J$ with respect to the parameters are calculated by the adjoint PUMA. Let $\mathcal{H}$ be the mapping of the $n \epsilon \mathbb{N}$ parameters $T_R$ on the $n$ elements of $\overline{T}$ as calculated by PUMA:

$$\begin{aligned} \mathcal{H} : \mathbb{R}^n &\rightarrow \mathbb{R}^n \\ T_R &\mapsto \overline{T}. \end{aligned} \tag{3.10}$$

This makes the cost function J and its first order approximation $\delta J$:

$$J(T_R) = \frac{1}{2}\left(\mathcal{H}(T_R) - \overline{T}_T, \mathcal{H}(T_R) - \overline{T}_T\right) \tag{3.11}$$

$$\delta J = \left(\nabla_{T_R} J(T_R), \delta T_R\right). \tag{3.12}$$

This equation introduces the gradient operator with respect to the parameters of the relaxation temperature field $\nabla_{T_R}$ to relate a small perturbation of this parameter $\delta T_R$ to a change in the cost function $\delta J$. Let $\mathbf{R}\,|_{T_{R_0}}$ be the tangent-linear model of $\mathcal{H}$, which is the Jacobian of $\mathcal{H}$ at a first-guess relaxation temperature field $T_{R_0}$. By writing $\delta\overline{T} = \mathbf{R}\big|_{T_{R_0}} \delta T_R$, the differentiation of (3.11) and subsequent application of the adjoint model $\mathbf{R}^*$ yields:

$$\delta J = \left(\mathcal{H}(T_{R_0}) - \overline{T}_T, \mathbf{R}\big|_{T_{R_0}} \delta T_{R_0}\right) \tag{3.13}$$

$$= \left(\mathbf{R}^*\big|_{T_{R_0}} \left(\mathcal{H}(T_{R_0}) - \overline{T}_T\right), \delta T_R\right). \tag{3.14}$$

Comparing (3.14) with the definition of the gradient of the cost function $\nabla_{T_R} J(T_{R_0})$ (3.12) leads to (in analogy to the development of Eq. 1.10):

$$\nabla_{T_R} J(T_{R_0}) = \mathbf{R}^*\big|_{T_{R_0}} \left(\mathcal{H}\left(T_{R_0}\right) - \overline{T}_T\right). \tag{3.15}$$

The linear operators $\mathbf{R}\,|_{T_{R_0}}$ and $\mathbf{R}^*\,|_{T_{R_0}}$ represent the tangent linear model and its adjoint. Both depend on the first guess relaxation temperature field $T_{R_0}$ about which the model is linearised. Equation (3.15) shows how the gradient of the cost function with respect to the relaxation temperature parameters can be calculated efficiently by feeding the misfit between the calculated and the targeted time mean model temperature, $\mathcal{H}(T_{R_0}) - \overline{T}_T$, into the adjoint model $\mathbf{R}^*\,|_{T_{R_0}}$.

### 3.3.2 Single storm track climate (control run)

Reconstructing the forcing of the mean climate we use a single storm track climate (Frisius et al., 1998). It is generated by a meridionally oriented heating and cooling dipole of the relaxation temperature $T_R$ (Fig. 3.13a), representing the contrast between a cold continent and a warm ocean current. In the vertical its amplitude follows a lapse rate and becomes isothermal near the tropopause. The climate response is characterised by a storm track developing downstream of the heating dipole. We use the climate mean temperature $\overline{T}$ (Fig. 3.13b) of this model climate (and its standard deviation $\sigma_T$; Fig. 3.13c) as the target climate $\overline{T}_T$ to reconstruct the forcing $T_R$.

### 3.3.3 Cost function properties

Experience has shown that with the above type of cost function, where the time average of a variable is included, a few precautions need to be taken. Lea et al. (2000) investigate the dependence of a time averaged variable of the Lorenz (1963) model on a single parameter. Their results suggest that analytical gradients calculated with the adjoint model are not useful for minimising the cost function when the averaging time is too long. Nonlinear dependence of the cost function on the parameter lets the gradient attain too large values which only represent the slope in a very small neighbourhood. On the other hand, for short averaging times, the dependence on the initial conditions of the model variables distorts the picture. Therefore, they suggest an ensemble of adjoint gradient calculations, with different initialisations of the model variables and an intermediate averaging time. In the `PUMA` model the shape of the cost function depends on the high-dimensional relaxation temperature field. Figs. 3.11 and 3.12 are an attempt to plot this relationship in a similar fashion as Fig. 1.6 for the Lorenz63-model. In order to plot the cost function for the `PUMA` model against the averaging time and the choice of the relaxation temperature, it is made dependent on a single parameter $\lambda$ which represents a one-dimensional parameter subspace:

$$T_R = (1 - \lambda)\overline{T}_T + \lambda T_{R_0}. \tag{3.16}$$

Here $T_{R_0}$ is chosen to be the relaxation temperature of the control experiment, which is the forcing of the single storm track climate. Choosing the mean temperature response as the target climate $\overline{T}_T$ in the cost function $J$, we expect $J$ to converge towards zero for $\lambda = 1$ and $t \to \infty$. Fig. 3.12 shows the value of a cost function which measures the difference between the `PUMA`-model climate for perturbed ($\lambda \neq 1$) and unperturbed ($\lambda = 1$) parameter values for different averaging times from daily mean to year mean (one model year are 8640 hours). No seasonal variations were included.

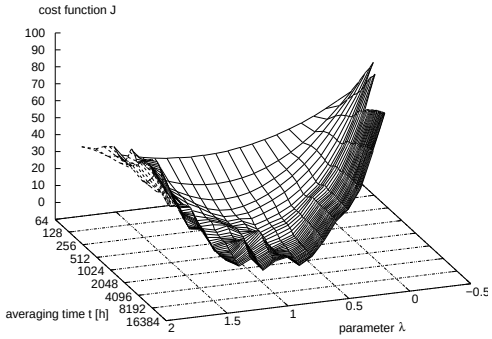


Figure 3.11: Cost function depending on different averaging times and parameters. The relaxation temperature parameters $T_R$ change from the target mean temperature $\overline{T}_T$ ($\lambda = 0$) to the known relaxation temperature of the control run $T_{R_0}$ ($\lambda = 1$) as described by equation (3.16). All integrations start ($t = 0$) from the same atmospheric state randomly chosen from the control run.

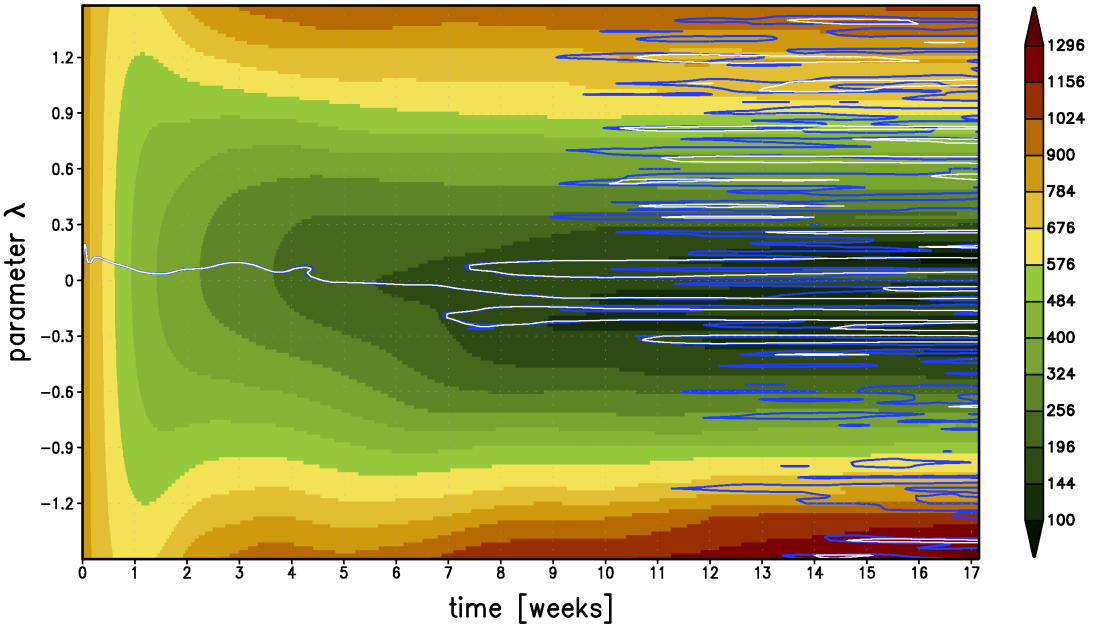


Figure 3.12: `PUMA`: Value of cost function $J(\lambda, t)$, as Fig. 3.11, for different averaging times $t$ in a one-dimensional projection of parameter space (shading, quadratic scale). The cost function measures the distance to a target spacial temperature distribution and parameter $\lambda$ varies the heat source. $\lambda = 0$ was used to create the target in a 10-year run of the model. The **blue line** is the zero-contour of the differentiated model ($\partial J/\partial\lambda$) while the thin **white line** is the centred differences approximation for comparison. Seasonality is not included.

Indeed the cost function possesses a marked minimum, where the forcing has the right shape and amplitude ($\lambda = 1$) even for short averaging times. This justifies the choice of an averaging time of 240 time steps for the cost function in the gradient calculations. At intermediate times in the order of months, however, internal variability causes some shifting of the minimum without severely changing its location.

### 3.3.4 Forcing reconstruction

An internal experiment is carried out to reconstruct the forcing of the single storm track climate. The mean temperature distribution of the control run (Fig. 3.13b) is taken as the target climate $\overline{T}_T$ in the cost function $J$. An iterative algorithm is used: First an ensemble of five calculations of the gradient is carried out with an averaging time of 240 time steps (corresponding to ten days). The initial conditions of the next ensemble member are the final conditions of its predecessor. The ensemble mean gradient field is then used to alter the relaxation temperature field $T_R$ (that is the forcing) by a small amount. Subsequently the model is run for 1200 time steps (50 days) to let the circulation adapt to the new parameters; then the cost function is evaluated. The final atmospheric conditions are made the initial conditions of the next iteration. The procedure is repeated until there is no further decrease of the cost function.

### 3.3.5 Results and Discussion

The gradients of the cost function $J$, obtained by the adjoint model and applied to reconstruct the single storm track climate of the control run, determine the forcing reasonably well in the lower levels of the model (Fig. 3.13d) while the upper levels (not shown) are less well defined. In this experiment, the relaxation time constant $\tau(\sigma)$ (from the diabatic part of temperature tendency $(\partial T/\partial t)_{diab.} = (T_R - T)/\tau$) is larger in the upper (30 days) than in the lower levels (10 and 5 days, respectively). They reflect the relative importance of advection versus radiative forcing. Long relaxation timescales should make the problem more nonlinear. However shorter relaxation times in the upper layers cannot be seen as a remedy since they would make the model less realistic and consequently alter the link between climate and forcing.

A `PUMA` simulation with the reconstructed relaxation temperature $T_R$ leads to a time mean temperature (Fig. 3.13e), which is remarkably similar to the mean temperature distribution of the control run ($\overline{T}_T$). This is also true for the upper levels and in contrast to the poor reconstruction of the forcing in these levels. Again their longer relaxation timescale appears to be the reason but this time with a positive effect. Baroclinic processes probably triggered by the bottom

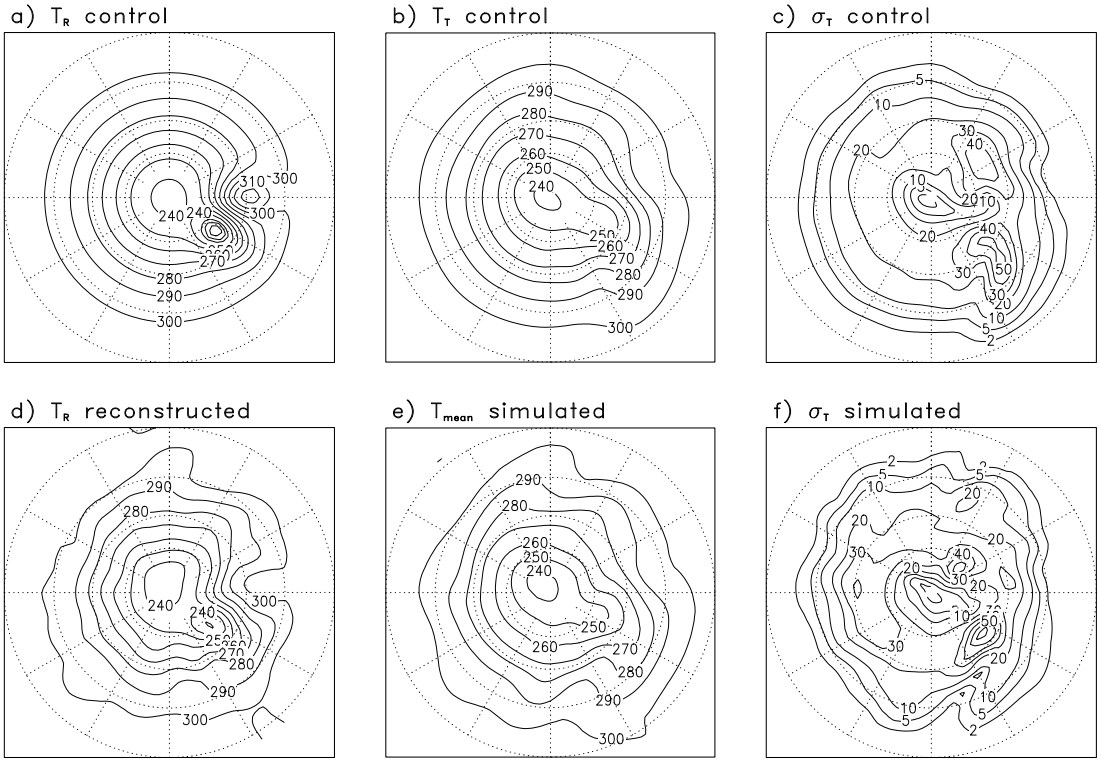


Figure 3.13: *Control run (single storm track climate):* **(a)** Relaxation temperature $T_{R_0}$, **(b)** mean temperature $\overline{T}$ and target temperature $\overline{T}_T$ in the cost function $J$, **(c)** standard deviation of the temperature $\sigma_T$. *Reconstruction:* **(d)** Relaxation temperature $T_R$ reconstructed from $\overline{T}_T$, **(e)** mean temperature of a simulation with $T_R$, **(f)** standard deviation of the temperature in the simulation with relaxation temperature $T_R$ (all at $\sigma$-level 0.9 near 900 hPa).

level make up for the errors in the radiative-convective parameterisation in the temperature tendency. The similarities between the temperature variances in the control run (Fig. 3.13c) and the simulation (Fig. 3.13f) are less well pronounced but some features are reproduced. A second experiment, which includes orography in the control run and in the run with the reconstructed forcing, yields results of comparable quality (not shown).

The experiment demonstrates that the combined information of model dynamics and a spacial distribution of the mean temperature can contain enough information to reconstruct main aspects of a historical climate. On the technical side, the averaging of gradients over different realisations has proven successful to avoid secondary minima far away from the known solution. The remaining uncertainty reflects the internal fluctuations of the model climate. It remains open whether comparable results could be achieved for a model of increased resolution.

# Chapter 4

# Interpreting the atmospheric circulation trend during the last half of the 20th century

The tangent linear adjoint for a low resolution dynamical model of the atmosphere (T21, 5 levels in the vertical) `PUMA` (see chapter 2) is used to derive the optimal forcing perturbations for all state variables such that after a specified lead time the model response has a given projection, in terms of an energy norm, on the pattern associated with the 51 year trend in the northern hemisphere winter tropospheric circulation, 1948/49-1998/99. A feature of the derived forcing sensitivity is a Rossby wave-like feature that emanates from the western tropical Pacific and is associated with the deepening of the Aleutian low, whereas an annular pattern in the forcing sensitivity in the uppermost model level is shown to be associated with the pattern of the trend over the Euro-Atlantic/Asian sectors, including the upward trend in the North Atlantic Oscillation Index. We argue that the Rossby wave-type feature is consistent with studies that have argued a role for the upward trend in tropical sea surface temperature during the 51 year period . On the other hand we interpret the annular pattern in the forcing sensitivity as being consistent with studies that have argued that the trend over the Euro-Atlantic sector was associated with influences from the stratosphere. In particular, a nonlinear model driven by the optimal forcing perturbation applied only to the top model level is successful at reproducing the trend pattern with the correct amplitude in the Euro-Atlantic sector, but implies a trend over the North Pacific towards a weaker Aleutian low, contrary to what was observed but similar to the spatial pattern associated with the Northern Annular Mode. These results show that the adjoint approach can shed light on previous apparently different interpretations of the trend. The study also presents a successful application of a tangent linear adjoint model to a climate problem.

## 4.1 Introduction

Figure 4.1 shows the trend in northern hemisphere winter (DJF) 500 hPa geopotential height (hereafter Z500) during the last half of the 20th century (1948/49 – 1998/99) taken from NCEP reanalysis data. Although there are some variations in details between different reanalysis products, the basic features are robust, in particular the deepening trend for both the Aleutian and Icelandic lows. The latter was associated with an upward trend in the North Atlantic Oscillation (NAO) index (*e.g.* Hurrell 1996; Hurrell *et al.* 2003) which, itself, has been the subject of much speculation regarding the possible role of anthropogenic forcing (*e.g.* Wunsch 1999; Greatbatch 2000; Feldstein 2002; Gillett *et al.* 2003). The pattern of the trend projects strongly onto the so-called COWL (Cold Ocean Warm Land) pattern (see Lu *et al.* 2004; Wu and Straus 2004) identified by Wallace *et al.* (1996), and it has been suggested that the trend corresponds to an increased occupancy of the circulation regime associated with COWL (Corti *et al.* 1999).

Currently, there are two competing hypotheses as to the origins of the circulation trend, both of which could involve some contribution from anthropogenic forcing. The first concerns the upward trend in tropical ocean sea surface temperature (SST). In particular, Hoerling *et al.* (2001) showed that the NCAR CCM3 model, run with the time series of the observed SST at the lower boundary, reproduces the observed trend in northern hemisphere winter Z500 in the ensemble mean sense, but with the amplitude reduced by half. Their work further pointed to the importance of forcing from the tropical Pacific and Indian Oceans, and indeed, there was a marked shift in tropical convection eastwards in the tropical Pacific associated with the climate shift that took place around 1976 (*e.g.* Trenberth *et al.* 2002; Deser *et al.* 2004). Nevertheless, Hoerling *et al.* (2004) and Hurrell *et al.* (2004) have gone on to argue an important role for the upward trend in SST in the tropical Indian Ocean (see also Bader and Latif 2003) and have noted that forcing the model with only the linear trend in SST at the lower boundary is successful at capturing the deepening trend of the Icelandic low, but that the deepening trend of the Aleutian low depends in their model on including the interannual variability of the tropical ocean SST. These authors have further argued that the discrepancy in amplitude between the trend in Z500 in their model simulations and in reality can be accounted for by a coincidence between the forced signal (captured by the ensemble mean) and internal variability of the climate system. Work by other authors has also pointed to the importance of forcing from the tropics, notably Lu *et al.* (2004) and Kucharski *et al.* (2006). The latter argue that the western tropical Pacific warm pool region played an important role in forcing the trend.

There has also been much speculation about the possible role of the stratosphere in the dynamics of the northern hemisphere winter circulation trend. This is because the strengthening of the circumpolar vortex was not confined to the tro-

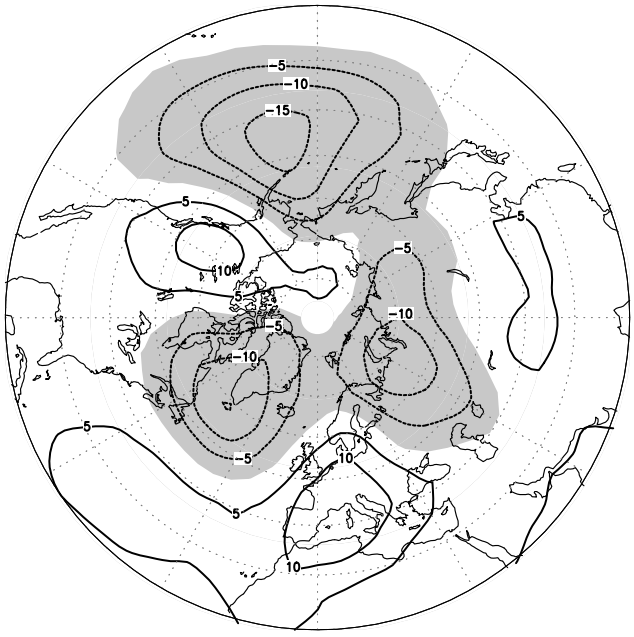


Figure 4.1: Linear trend in 500 hPa height over 51 winters of NCAR/NCEP reanalysis data. Contours are every 5 m(10 yr)$^{-1}$ and negative regions are shaded. All centres are significant on the 5%-level under the assumption that winter means are independent and normally distributed.

posphere alone, but also occurred in the stratosphere (*e.g.* Thompson *et al.* 2000). Furthermore, there is mounting evidence that circulation changes in the winter stratosphere can indeed affect the troposphere, with the changes in the stratosphere leading those in the troposphere on a time scale of days to months (*e.g.* Baldwin and Dunkerton 1999; Polvani and Kushner 2002; Gillett and Thompson 2003; Gillett *et al.* 2003; Charlton *et al.* 2004; Jung and Barkmeijer 2006). Indeed, Scaife *et al.* (2005) have pointed out that models driven by the observed time series of SST at the lower boundary consistently fail to capture the correct amplitude of the trend, some models doing much worse in this respect than Hoerling *et al.* (2001). Scaife et al. take a different approach and impose a trend on the stratospheric circulation in the Hadley Centre AM3 model comparable to that observed in the stratospheric circulation, and find that the model successfully reproduces the trend in the tropospheric circulation over the Euro-Atlantic sector with the correct amplitude, even though there is no anomalous SST forcing. These results suggest an important role for the stratosphere in the dynamics of the trend, at least over the North Atlantic sector. Nevertheless, there is still the question of the origin of the changes in the stratospheric circulation. In the case of the northern hemisphere, there is no really conclusive evidence that this is related to changes in the chemical composition of the stratosphere (*e.g.* ozone; Gillett *et al.* 2003), in which case the trend in the stratospheric circulation may

well originate from the troposphere. Evidence that there is an influence from El Niño events on the stratosphere has been presented by Taguchi and Hartmann (2006), suggesting a possible link, once again, to tropical ocean SST.

In order to gain more clarity about the different hypotheses, a method is required which identifies forcing perturbations that can excite a given climate response (in our case the pattern associated with the atmospheric circulation trend during the last half of the $20^{th}$ century). For non-linear systems like the atmosphere, this is a non-trivial task and a variety of methods exist, all of which have in common that they attempt to estimate a linear operator which links changes in climate to changes in forcing. The simplest and computationally most expensive approach is the execution of many forward runs using different small forcing perturbations, *e.g.* at each grid point, in order to estimate a complete set of Greens functions (an example is given by Branstator 1985). Another approach is based on a modified fluctuation-dissipation theorem (Gritsun and Branstator 2007 and references therein) and estimates the climate response to a (weak) forcing perturbation by using the covariances and lag-covariances of fluctuations of the undisturbed system. This approach relies on historical or synthetic data and involves the computation and handling of correlation matrices of what is usually a very high-dimensional state space. A related study is that of Penland (1989) based on the assumption that the atmosphere can be optimally modelled by a linear Markov process. Penland's approach assumes that the underlying system dynamics is linear and noise driven whereas the Fluctuation Dissipation approach of Gritsun and Branstator has the advantage that it does not require this assumption. A similar approach is that of Branstator and Haupt (1997) who construct a linear empirical model by seeking a best fit between the state vector of a fully nonlinear dynamical model and its time tendency.

Our approach is different again and uses a tangent-linear adjoint for a nonlinear dynamical model applied to both, model-generated (state space-) trajectories and trajectories taken from observations. The computations directly yield an estimate of the forcing perturbation that optimally excites the given climate response with a given lead-time. Since the forcing perturbation is optimal (in the sense to be defined in Section 4.2) it is not the only forcing perturbation that can excite the climate response and, in the case of the trend, it is not necessarily the forcing perturbation that actually led to the trend during the last half of the $20^{th}$ century. Rather, our approach indicates the most effective way of exciting a climate response that is similar to the trend pattern and, hopefully, throws light on the different interpretations of the trend noted earlier. This approach is comparable to established methodology in ocean-model studies (*e.g.* Junge and Haine, 2001; Junge and Fraedrich, 2007). A general discussion of the approach can be found in Eyink *et al.* (2004). A related issue is the question of the relevance to the climate problem of optimal forcing perturbations derived using a linear adjoint model with a lead time of days. Previous works, *e.g.* Corti and Palmer (1997) and, more recently Jung and Barkmeijer (2006), suggest that forcing de-

rived using a tangent linear adjoint, and applied to a fully nonlinear dynamical model, does indeed lead to a systematic forcing of the target pattern, an issue discussed further in this chapter and also by Iversen *et al.* (2008). Iversen *et al.*, like us, use a tangent linear adjoint to determine optimal forcing perturbations for the COWL pattern (to which the pattern of the trend is closely related). Their basic model is the ECMWF operational model and they are only able to determine the optimal forcing with a lead times of 4 days. In our study, due to the much coarser resolution of our model, we are able to extend the lead out as far as 14 days (the results we show use 12 days lead time).

The dynamical model used to derive the tangent linear adjoint is essentially the same as that used by Lu *et al.* (2004). Lu et al. had earlier argued that the trend can be captured by a model linearised about the climatological winter mean state and that the important forcing originates in the tropical Indo-Pacific region. We therefore begin by using the adjoint for a model linearised about the winter climatological mean state, and then go on to use the adjoint tangent linear version of the model linearised about both observed and model generated trajectories.

We begin in Section 4.2 by describing the model set-up and the adjoint technique. Section 4.3 presents the results and Section 4.4 provides a summary and discussion.

## 4.2 Description of the adjoint model

We take as our starting point the model of Hall (2000), previously used by Lu *et al.* (2004) to study the trend. The dynamical core of the Hall model is the semi-spectral model of Hoskins and Simmons (1975) and is essentially the same as employed in the `PUMA` model (*P*ortable *U*niversity *M*odel of the *A*tmosphere; Fraedrich *et al.* 2005) developed at the University of Hamburg. The `PUMA` model is used for all the model runs presented here (the dynamical cores of the two models differ only in the spectral truncation: while `PUMA` uses triangular, the Hall model uses a "jagged" truncation). The Hall model has a flat-bottom, a horizontal resolution of T21 and a vertical resolution of five $\sigma$-levels. The model solves the dry primitive equations on a sphere and employs empirical forcing for all state variables derived from daily mean data for the northern hemisphere winter season taken from the NCAR/NCEP reanalysis (the technique is an extension to the primitive equations of that applied by Marshall and Molteni 1993 to a quasi-geostrophic model). The model exhibits a realistic climate (Hall 2000) and also reproduces the principal modes of variability exhibited by the northern hemisphere winter troposphere (*e.g.* the North Atlantic Oscillation and the Pacific-North America pattern, Wallace and Gutzler 1981). To study the trend, Lu *et al.* (2004) used forcings derived independently for each winter from 1948/49 to 1998/99. These forcings consist of climatological forcing (the average

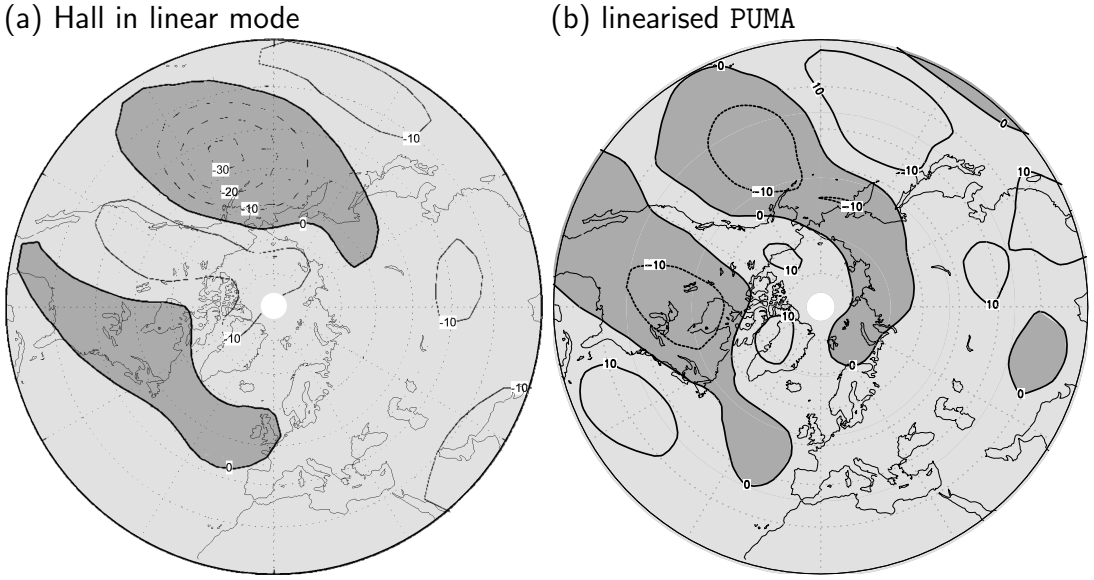


Figure 4.2: Response of 500hPa-geopotential height in the linear model to the forcing from the tropical western Indo-Pacific (36° S – 36° N, 60° E – 180° E) derived in Lu *et al.* (2004): **(a)** Hall model in linear mode (after Lu), **(b)** linearised PUMA model. Both simulations use the same climatological reference state; results are averaged from day 10 through day 16.

over all 51 winters) plus forcing anomalies for each winter. In the present study, we take the inverse approach. In particular, we use the adjoint model to infer the optimal forcing anomaly that can excite the pattern associated with the trend with lead times up to 14 days. The model parameters and resolution are the same as used by Hall (2000) and Lu *et al.* (2004). Forward model runs are carried out (see below) using a constant forcing. The tangent linear and adjoint code were generated with the aid of the TAMC (Tangent linear and Adjoint Model Compiler, Giering and Kaminski 1998), a source-to-source compiler.

To understand how the adjoint technique works, we begin by noting that the forward model can be written as the action of a nonlinear operator $N$ on the model state $\Psi$ plus a time-independent forcing term $\mathbf{f}$:

$$\frac{\partial \boldsymbol{\Psi}}{\partial t} = N(\boldsymbol{\Psi}) + \mathbf{f}. \tag{4.1}$$

Linearising about a given (possibly time dependent) reference state $\boldsymbol{\Psi}_\mathbf{0}(t)$ with respect to model state and forcing yields the tangent-linear model with forcing. The tangent linear model predicts the first order development of perturbations of the original model:

$$\left.\frac{\partial\, \delta\boldsymbol{\Psi}}{\partial t}\right|_{\boldsymbol{\Psi}_\mathbf{0}(t)} = \left.\frac{\partial N}{\partial \boldsymbol{\Psi}}\right|_{\boldsymbol{\Psi}_\mathbf{0}(t)} \delta\boldsymbol{\Psi} + \delta\mathbf{f}. \tag{4.2}$$

Lu *et al.* (2004) approximate the operator $\frac{\partial N}{\partial \mathbf{\Psi}}\big|_{\mathbf{\Psi_0}(t)}$ of the above equation for the case of a time-independent reference (or 'basic') state $\mathbf{\Psi_0}$. To achieve this, they apply a special forcing to the nonlinear operator $N$ to maintain the reference state, and choose $\delta\mathbf{f}$ sufficiently small to get a mainly linear response. Figure 4.2a shows a result from their study created with this method. In the present study we use the operator $\frac{\partial N}{\partial \mathbf{\Psi}}\big|_{\mathbf{\Psi_0}(t)}$ itself, which allows us to use time-varying reference states. Integrating Eq. (4.2) from time $t = t_1$ to $t_2$, with the forcing perturbation $\delta\mathbf{f}$ set to zero, gives an operator $\mathbf{R}_{t_1}^{t_2}$ (called the resolvent or propagator, $\delta\mathbf{\Psi}_{t_2} = \mathbf{R}_{t_1}^{t_2}\,\delta\mathbf{\Psi}_{t_1}$), which is linear with respect to the initial state perturbation $\delta\mathbf{\Psi}_{t_1}$, but still depends nonlinearly on the reference state $\mathbf{\Psi_0}(t)$. It propagates a perturbation $\delta\mathbf{\Psi}_{t_1}$ at $t = t_1$ to $\delta\mathbf{\Psi}_{t_2}$ at $t = t_2$ and can be expressed as $\mathbf{R}_{t_1}^{t_2} = \frac{\partial \mathbf{\Psi}_{t_2}}{\partial \mathbf{\Psi}_{t_1}}$. This is the tangent-linear model for initial state perturbations. The solution of Eq. (4.2) with forcing then gives the tangent-linear model for forcing and initial state perturbations:

$$\delta\mathbf{\Psi}_{t_2} = \mathbf{R}_{t_1}^{t_2}\,\delta\mathbf{\Psi}_{t_1} + \int_{t_1}^{t_2} \mathbf{R}_t^{t_2}\,\delta\mathbf{f}\,dt \tag{4.3}$$

(compare, for example, with Eq. 6 in Barkmeijer *et al.* 2003). Setting the initial perturbation of the model state $\delta\mathbf{\Psi}_{t_1}$ to zero and replacing the integral with a sum over the actually performed model time steps leads to

$$\delta\mathbf{\Psi}_{t_2} = \sum_{t=t_1}^{t_2} \mathbf{R}_t^{t_2}\,\delta\mathbf{f}\,\Delta t. \tag{4.4}$$

Thus the effect of the forcing is expressed as the accumulated action of the linear operator $\mathbf{R}_t^{t_2}$ on the small model perturbation $\delta\mathbf{f}\,\Delta t$ at each time step. Figure 4.2b shows an example of a run of this model forced with the tropical western Indo-Pacific part of the forcing derived in Lu *et al.* (2004), using the their climatology as a constant reference state for comparison.

In the following it is the adjoint $\mathbf{R}_t^{t_2\,*}$ of $\mathbf{R}_t^{t_2}$ that is used to determine the optimal constant anomalous forcing $\delta\mathbf{f_{opt}}$ required to excite a targeted state perturbation $\delta\mathbf{\Psi}_T$ with lead time $t_2 - t_1$. By definition, an adjoint operator satisfies the equation $\langle \mathbf{R}\mathbf{\Psi}_a, \mathbf{\Psi}_b\rangle = \langle \mathbf{\Psi}_a, \mathbf{R}^\star\mathbf{\Psi}_b\rangle$ for some scalar product. Here $\langle\cdot,\cdot\rangle$ defines the Euclidian scalar product so that, in matrix notation, we have $(\mathbf{R}\mathbf{\Psi}_a)^T\mathbf{\Psi}_b = \mathbf{\Psi}_a^T\,(\mathbf{R}^T\,\mathbf{\Psi}_b)$.

We now introduce a projection index $I$ of the model state $\mathbf{\Psi}$ on the observed trend pattern $\delta\mathbf{\Psi}_T$. Its variation $\delta I$ with respect to an evolved model state perturbation $\delta\mathbf{\Psi_2}$ is given by:

$$\delta I = (\delta\mathbf{\Psi}_{t_2}; \delta\mathbf{\Psi}_T) \tag{4.5}$$

The scalar product $(\cdot;\cdot)$ is defined as the area- ($\mathbf{W}$) and energy-weighted ($\mathbf{E}$) Euclidean scalar product $\langle\cdot, \mathbf{WE}\,\cdot\rangle$. The energy-weighting attempts to make the

contributions of the different physical variables of the model state vector comparable in the contribution to the norm (see the sensitivity measure in Langland et al 2002 and Barkmeijer *et al.* 2003 for further discussion of this issue). The entries of the matrix $\mathbf{E}$ are derived from the linearised total energy norm of a perturbation to an isothermal, resting atmosphere with horizontally invariant surface pressure (Talagrand 1991, Errico 2000). It is diagonal and its elements are defined in terms of the Euclidian scalar product $\langle \cdot, \cdot \rangle$ by the equation

$$\begin{aligned}\langle \delta\mathbf{\Psi}_1, \mathbf{WE}\, \delta\mathbf{\Psi}_2 \rangle = \\ \tfrac{1}{2g} \sum_{\lambda,\phi} \Bigg( \Big( \sum_{\sigma} \Big( \Big( \delta u_1(\sigma)\delta u_2(\sigma) + \delta v_1(\sigma)\delta v_2(\sigma) + \tfrac{c_p}{T_{ref}} \delta T(\sigma)_1 \delta T(\sigma)_2 \Big) \bar{p}_s \Delta\sigma_h \Big) \\ + T_{ref} p_{ref} R \delta \ln p_{s1} \delta \ln p_{s2} \Big) w_{\lambda,\phi} \Bigg). \end{aligned} \tag{4.6}$$

Here $\mathbf{\Psi}_i = (\zeta_i, D_i, T_i, \ln p_{si})^T$, where $\zeta$ is vorticity, $D$ is horizontal divergence, $T$ is temperature and $p_s$ is surface pressure. The horizontal velocity $(u_i, v_i)$ is a function of $\zeta_i$ and $D_i$ given by $[(\hat{\mathbf{k}} \times \nabla)\Delta^{-1}\zeta + \nabla\Delta^{-1}D]$ ($\hat{\mathbf{k}}$ is a unit vector in the upwards vertical direction), $g$ is the gravitational acceleration, $\bar{p}_s$ the global mean surface pressure, $c_p$ is the specific heat of dry air at constant pressure, $T_{ref} = 300$ K is a reference temperature, $\Delta\sigma_h$ is the distance between adjacent half-levels, $p_{ref} = 800$ hPa is a reference pressure, $R$ is the gas constant for dry air, and $w_{i,j}$ are the relative area weights. Thus, using Eqs. (4.4), (4.5), linearity, and the adjoint propagator $\mathbf{R}_t^{t_2\,*}$, we get:

$$\delta I = \left\langle \sum_{t=t_1}^{t_2} \mathbf{R}_t^{t_2}\, \delta\mathbf{f}\, \Delta t\ ,\ \mathbf{WE}\, \delta\mathbf{\Psi}_T \right\rangle \tag{4.7}$$

$$= \left\langle \delta\mathbf{f}\ ,\ \sum_{t=t_1}^{t_2} \mathbf{R}_t^{t_2\,*} \mathbf{WE}\, \delta\mathbf{\Psi}_T\, \Delta t \right\rangle. \tag{4.8}$$

The sum is over individual time steps $\Delta t$ of the model. Given the equivalence $\delta I = \langle \delta\mathbf{f}, \mathbf{f}^* \rangle \Leftrightarrow \mathbf{f}^* = \nabla_{\mathbf{f}} I$, the expression $\mathbf{f}^* = \sum_{t=t_1}^{t_2} \mathbf{R}_t^{t_2\,*} \mathbf{WE}\, \delta\mathbf{\Psi}_T\, \Delta t$ in the scalar product of Eq. (4.8) is just *the gradient of $I$ with respect to a constant forcing* or, for brevity, *forcing sensitivity* (cf. Barkmeijer *et al.* 2003). It has the unit of $[I]/[\mathbf{f}]$. Maps of forcing sensitivity $\mathbf{f}^\star$ show at each point how strong an index perturbation $\delta I$ would result from a unit perturbation of the forcing of the respective state variable at that point in a forward run of the linearised model. Eq. (4.9) below shows how to use $\mathbf{f}^\star$ to construct a forcing which uses minimal energy to produce a given index perturbation $\delta I$. In a linear context this is equivalent to the maximum response at a given forcing energy. Such a forcing perturbation is termed *optimal forcing* in the remainder of this chapter.

Mathematically, for a forcing perturbation $\delta\mathbf{f}$ to be *optimal* we require that for a given index change $\delta I = \langle \delta\mathbf{f}, \mathbf{f}^* \rangle$ and lead time $t_2 - t_1$, the forcing perturbation has minimal "energy" $\langle \delta\mathbf{f}, \mathbf{WE}\,\delta\mathbf{f} \rangle$. Using the method of Lagrange-multipliers yields

$$\delta\mathbf{f}_{opt} = \lambda \mathbf{E}^{-1}\mathbf{W}^{-1}\mathbf{f}^*, \text{ with } \lambda = \frac{\delta I}{\langle \mathbf{f}^*, \mathbf{E}^{-1}\mathbf{W}^{-1}\mathbf{f}^* \rangle}. \tag{4.9}$$

### 4.2.1 Relationship of sensitivities and optimal forcing

The kinetic energy part of the energy matrix defined by Eq. (4.6) involves the transform of vorticity and divergence to the horizontal velocity components $u$ and $v$. Defining $\mathbf{U}$ as the operator $\left(\hat{\mathbf{k}} \times \boldsymbol{\nabla}, \boldsymbol{\nabla}\right)^T$, which converts $(u, v)^T$ to $(\zeta, \mathbf{D})^T$, and $\mathbf{Z} = \mathbf{U}^{-1} = \mathbf{U}\Delta^{-1}$ as the inverse of $\mathbf{U}$ (as used for Eq. 4.6), the following relationship holds for the optimal forcings in terms of velocities, $\mathbf{f_{opt_{u,v}}}$, and vorticity and divergence, $\mathbf{f_{opt_{\zeta,D}}}$:

$$\mathbf{f}_{opt_{\zeta,D}} = \mathbf{U}\mathbf{f}_{opt_{u,v}}, \tag{4.10}$$

and for the forcing sensitivities with respect to velocities, $\mathbf{f^*}_{u,v}$ and vorticity and divergence, $\mathbf{f^*}_{\zeta,D}$ (cf. Appendix B of Kleist and Morgan 2005):

$$\mathbf{f^*}_{u,v} = \mathbf{U^*}\mathbf{f^*}_{\zeta,D}. \tag{4.11}$$

Furthermore we can write the sub-matrix $\mathbf{E}_{\zeta,D}$ of $\mathbf{E}$ which operates on the components contributing to kinetic energy as

$$\mathbf{E}_{\zeta,D} = \mathbf{Z^*}\mathbf{E}_{u,v}\mathbf{Z}, \tag{4.12}$$

since $\mathbf{W}$ is diagonal and $\langle \mathbf{Z}\cdot, \mathbf{WE}_{u,v}\mathbf{Z}\cdot \rangle = \langle \cdot, \mathbf{Z^*WE}_{u,v}\mathbf{Z}\cdot \rangle$. Inserting Eq. (4.12) into Eq. (4.9) yields

$$\mathbf{f}_{opt_{\zeta,D}} = \lambda \mathbf{U}\mathbf{E}_{u,v}^{-1}\mathbf{W}^{-1}\mathbf{U}^*\mathbf{f^*}_{\zeta,D}. \tag{4.13}$$

Since $\mathbf{E}_{u,v}$ and $\mathbf{W}$ are diagonal, we find the shape of $\mathbf{f^*}_{\zeta,D}$ and $\mathbf{f_{opt}}_{\zeta,D}$ to differ only from the combined operator $\mathbf{UU}^*$ which is equal to $-\mathbf{I}\Delta$ ($\mathbf{I}$ being the identity matrix). This reflects the difference between kinetic energy weights and enstrophy weights. The fact that the optimal forcing involves the application of a Laplacian operator to the forcing sensitivity explains why the latter has much more small scale structure than the former. Apart from the scaling, the sensitivities have the structure of the stream function field corresponding to the optimal vorticity perturbation.

### 4.2.2 Geopotential height as target pattern

Throughout this chapter geopotential height is conveniently used for the graphical representation of the thermal structure of the lower half of the troposphere. Nonetheless, with the aid of the total perturbation energy norm (Eq. 4.6), the projection index $I$ (Eq. 4.5) is defined for projections onto full atmospheric states, *i.e.* including three-dimensional temperature, velocity fields and surface pressure. Alternatively it is possible to project directly onto geopotential height fields. Introducing a linearised operator $\mathbf{D}_{z_p}$ which diagnoses the first order response of the geopotential height of a pressure surface $p$ to changes in temperature and surface pressure, we can change the definition of the index $I$ by replacing the projection on an anomaly of the model state $\delta\mathbf{\Psi}_T$ (target pattern) by a geopotential height pattern $\delta\mathbf{z}_{\mathbf{p}T}$. For this case the matrix $\mathbf{E}$ is dropped from the projection index since there is no need to weigh the contributions of different physical fields.

$$\begin{aligned}
\delta I &= \left\langle \mathbf{D}_{z_p}\,\delta\mathbf{\Psi}_{t_2}, \mathbf{W}\,\delta\mathbf{z}_{\mathbf{p}T} \right\rangle && (4.14)\\
&= \left\langle \mathbf{D}_{z_p} \sum_{t=t_1}^{t_2} \mathbf{R}_{t_1}^{t_2}\,\delta\mathbf{f}\,\Delta t, \mathbf{W}\,\delta\mathbf{z}_{\mathbf{p}T} \right\rangle && (4.15)\\
&= \left\langle \delta\mathbf{f}, \sum_{t=t_1}^{t_2} \mathbf{R}_{t_1}^{t_2\star}\mathbf{D}_{z_p}^{\star}\mathbf{W}\,\delta\mathbf{z}_{\mathbf{p}T}\,\Delta t \right\rangle && (4.16)
\end{aligned}$$

Consequently, the forcing sensitivity for this case takes the form:

$$\mathbf{f}^{\star} = \sum_{t=t_1}^{t_2} \mathbf{R}_{t_1}^{t_2\star}\mathbf{D}_{z_p}^{\star}\mathbf{W}\,\delta\mathbf{z}_{\mathbf{p}T}\,\Delta t \qquad (4.17)$$

Note that $\mathbf{E}$ still is part of the norm and Eq. (4.9) applies. However, throughout this chapter a projection index will be used which projects onto the trend in all model variables unless explicitly stated otherwise. The reason is that a geopotential height pattern as target may be dynamically ambiguous and could lead to forcing sensitivities which reflect the action of gravity waves on short timescales.

### 4.2.3 Sensitivity Averaging

In Section 4.3.1 we discuss results when we have an ensemble of trajectories taken from either the NCAR/NCEP reanalysis data or from an unperturbed forward run with the model of Hall (2000). When using an ensemble of trajectories, the optimal forcing perturbation is computed using equation (4.9) applied to the average of the sensitivities, but with the amplitude rescaled so that the forcing perturbation has the same total energy norm (Eq. 4.6) as the optimal forcing perturbation in the case linearised about winter climatology. We note that by averaging over the sensitivities we hope to capture some information about the eddying, nonlinear character of the real atmosphere hopefully leading to a more

realistic derived forcing perturbation than for the cases that use a model linearised about the winter mean climatology. In terms of the investigations of section 1.4, this is to ensure the sensitivity reflect the sensitivity of the model climate.

## 4.3 Results

In what follows, the target or trend pattern is the total change over 51 years related to the linear trend during winter, 1948/49 to 1998/99, at each grid point and for each model variable, except that we restrict the target to the region north of 20°N in order to focus on the northern hemisphere. Figure 4.1 shows the trend, as it appears in Z500, and Figure 4.3 shows the area weighted (Euclidean) projection of daily mean NCAR/NCEP Z500 data on the trend pattern. Figure 4.3 gives an indication of the day to day variability in the occupation of the trend pattern by the atmosphere over all 51 winters. There is a clear trend over the 51 year period toward more days with a stronger than average projection on this pattern, as expected.

### 4.3.1 The forcing sensitivities

We begin by using the adjoint to determine the optimal forcing perturbations for a fixed projection on the target pattern and different lead times. For the case linearised about climatology, we can test the "efficiency" with which the forcing at different lead times excites the target pattern by plotting the amplitude of the optimal forcing as a function of lead time. The forcings are the result of equation (4.9) with $\delta I$=34.4 kJm$^{-2}$, which is the projection of the target upon itself, $\langle \delta\mathbf{\Psi}_T, \mathbf{WE}\, \delta\mathbf{\Psi}_T \rangle$. Their amplitudes are computed using the square root of the energy norm. As can be seen from Fig. 4.7, the amplitude initially decreases rapidly as the lead time increases, and then levels off. Furthermore amplitude times lead time also decreases as lead time increases. These results indicate that, at least out to 14 days, the longer the lead time the more efficient the optimal forcing becomes at exciting the trend pattern. As the lead time is increased the forcing sensitivities settle down into the patterns shown in parts (a-c) of Figs. 4.4 to 4.6 for which the lead time is 12 days. (Unless stated otherwise all following experiments use a 12 day lead time.) We show mostly forcing sensitivities, and not the optimal forcing perturbations themselves, because the latter have a lot of small scale structure for vorticity and divergence. (Compare parts c and d of the figures and see section 4.2.1 for a detailed explanation.) In essence, the presence of the small scale structures in the optimal forcing for vorticity and divergence are a consequence of using the energy norm and the need, as a consequence, to convert from vorticity and divergence to velocity. The result is that the optimal forcings for vorticity and divergence are related to their corresponding forcing sensitivities by a Laplacian operator which, in turn, puts weight on small spatial

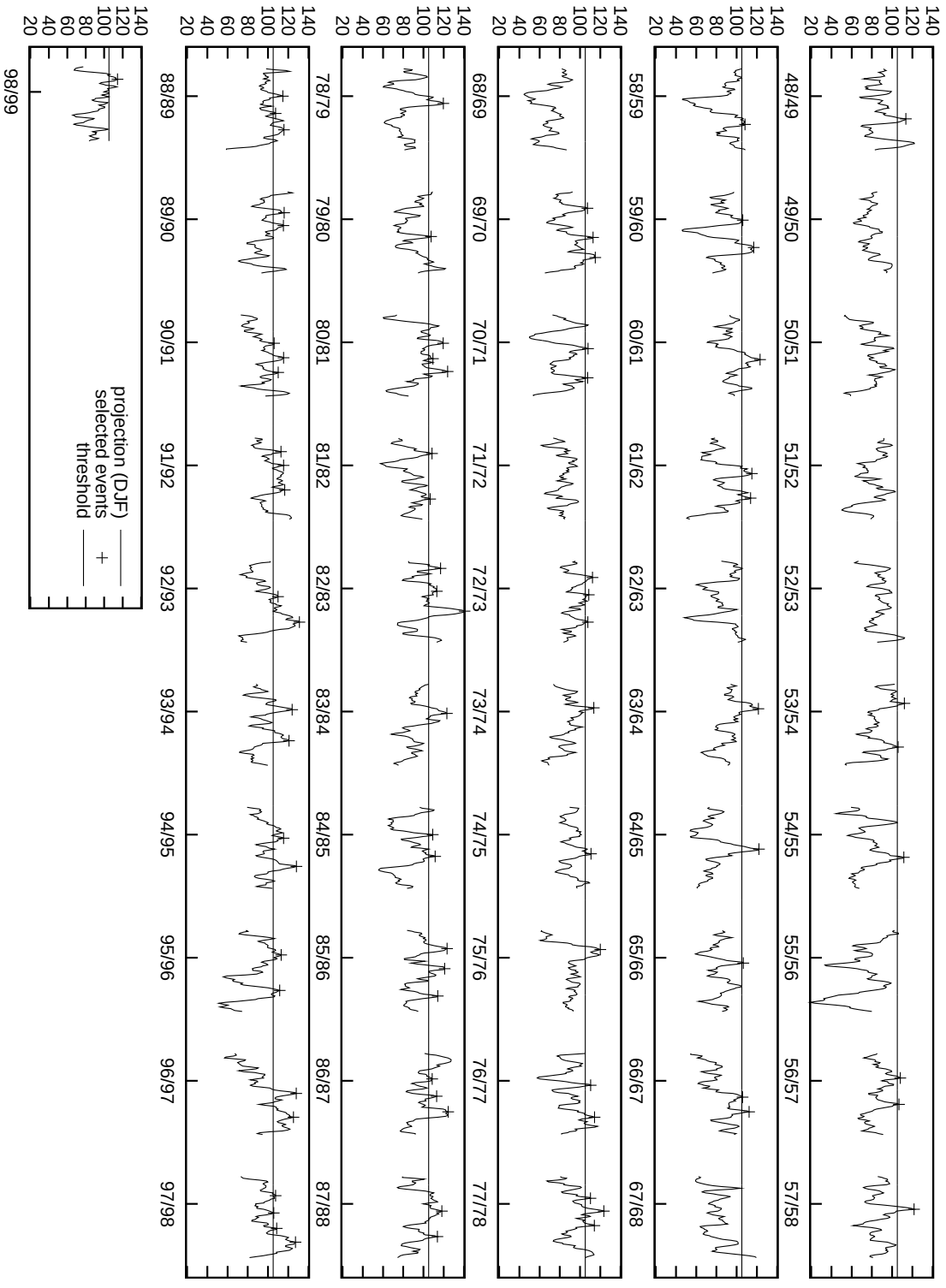


Figure 4.3: Projection of daily NCAR/NCEP 500 hPa height data onto the 500 hPa trend north of 20 N (Fig. 4.1). The line separates the higher 10% from the lower 90%. Crosses mark the maxima used for the subset of composites that terminate with a strong projection on the trend pattern (see text).

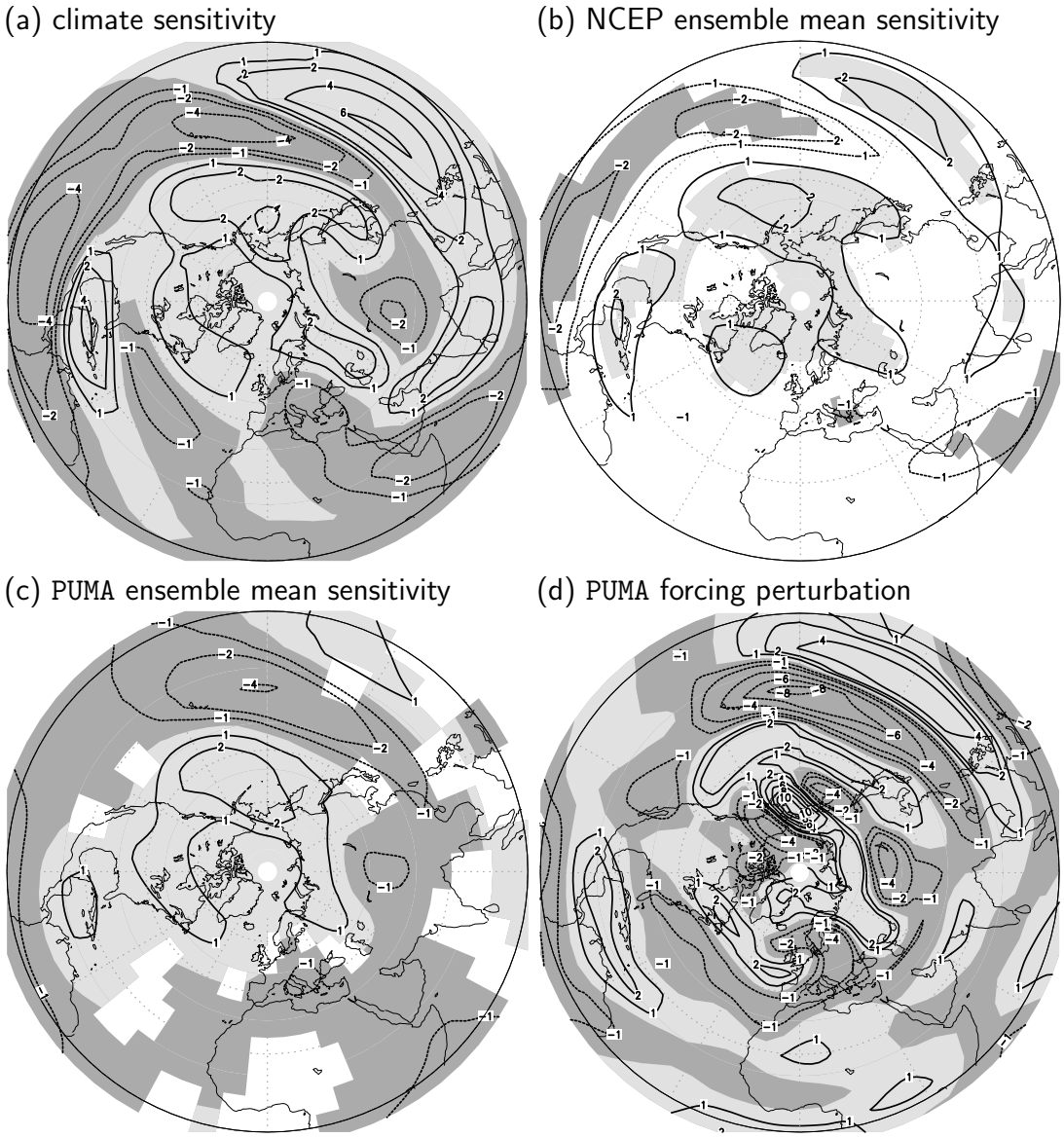


Figure 4.4: Sensitivities (in $10^{12}$ $\mathrm{Jm^{-2}s^{-1}}$) for the vorticity forcing in the middle model level (about 500 hPa) in **(a)** the linear adjoint experiment, **(b)** averaged over many realisations of the adjoint using the NCAR/NCEP trajectories, and **(c)** averaged over many realisations of the adjoint PUMA experiment. **(d)** optimal forcing perturbations (in $10^{-12}\mathrm{s^{-2}}$) derived from (c). In parts (b) and (d) only sensitivities which are significant on the 10%-level are shaded (light grey: positive; dark: negative). All sensitivities are scaled to relate to the full observed amplitude of the trend pattern. Optimal forcing perturbations in (d) are scaled to have the same global amplitude as in the case linearised about climatology (see text for details).

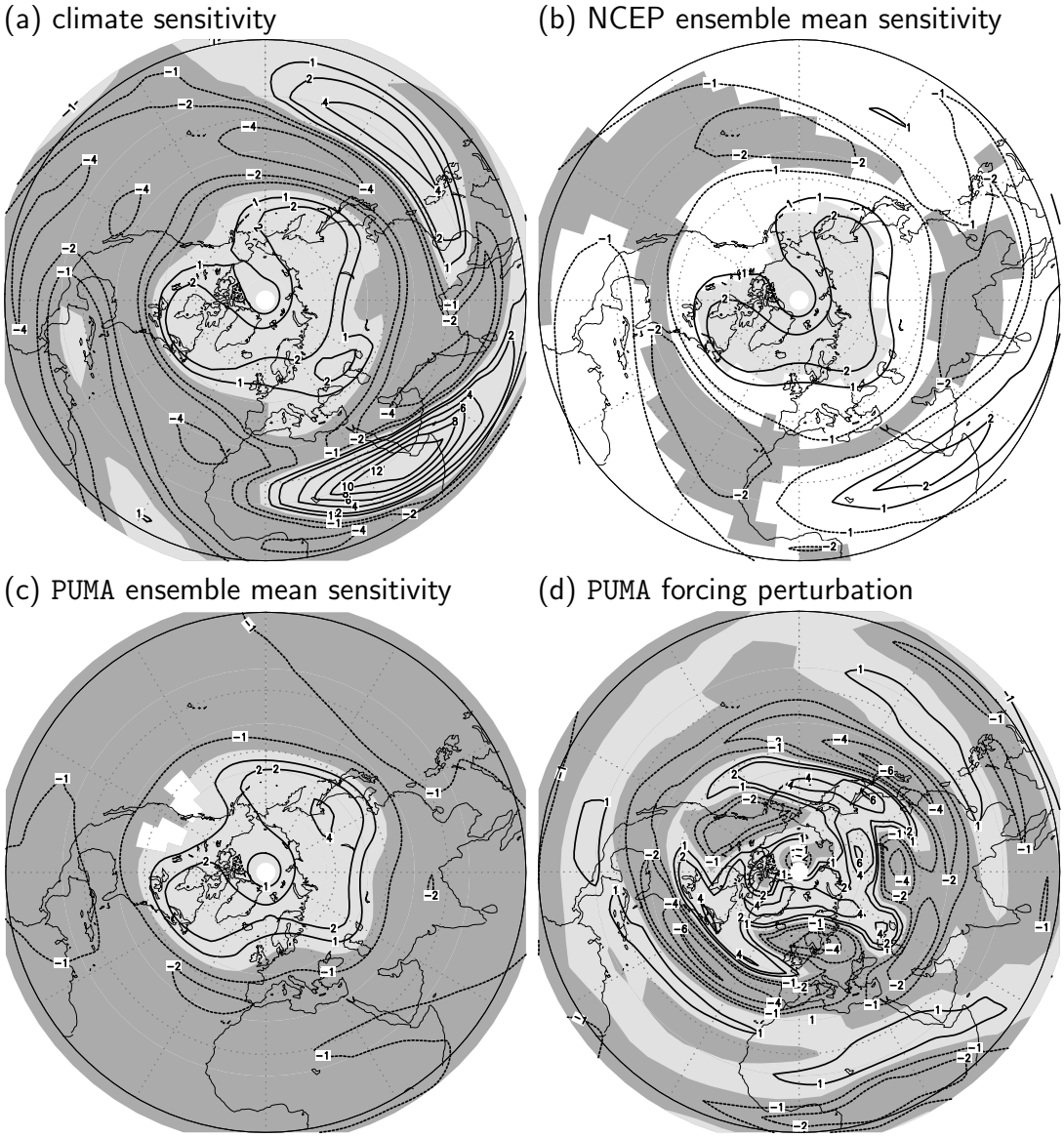


Figure 4.5: As Figure 4.4 but for vorticity forcing in the highest model level (about 100 hPa).

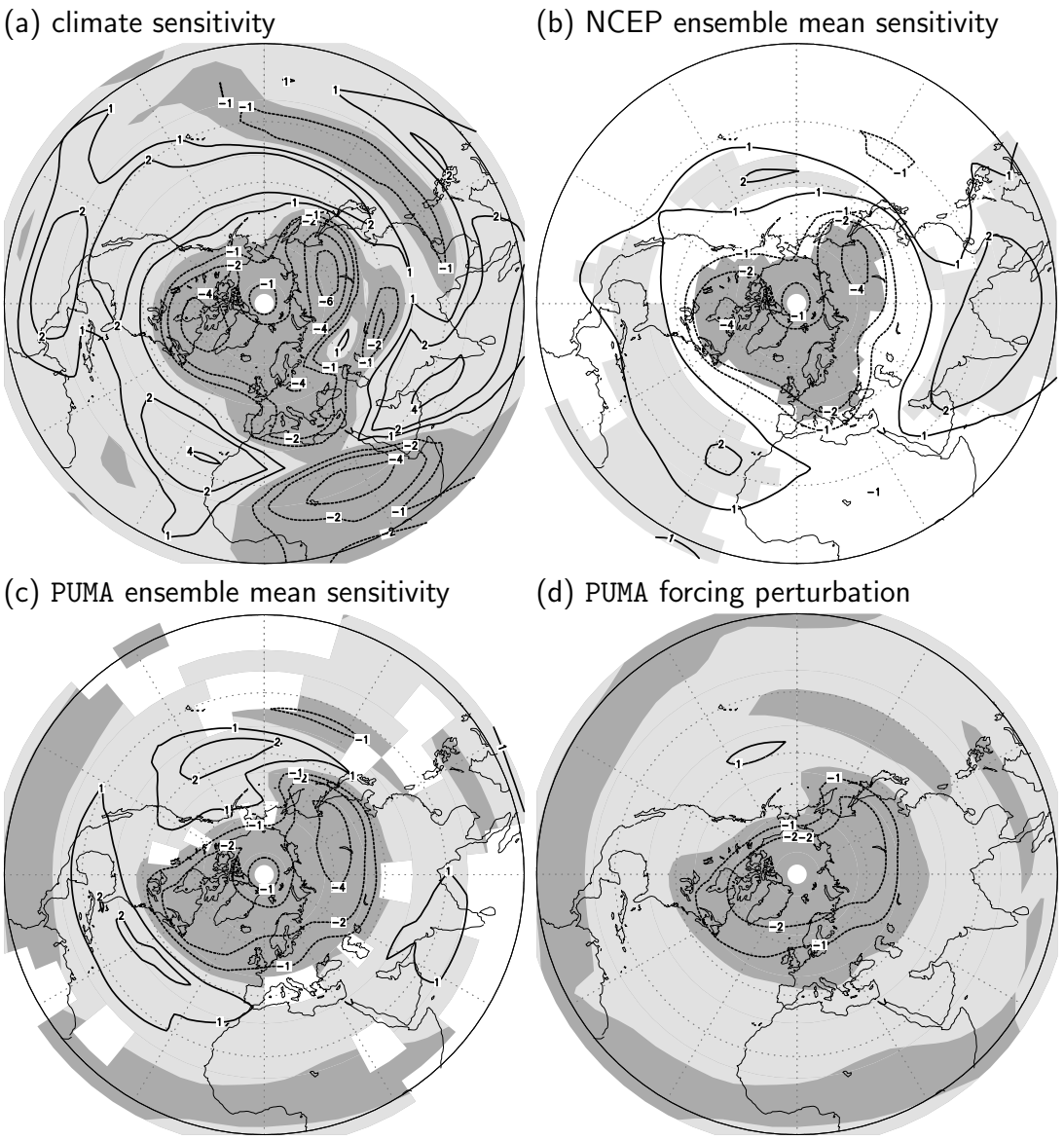


Figure 4.6: As Figure 4.4 but for temperature forcing in the highest model level (100 hPa). Sensitivities (a,b,c) in $10^6$ $\mathrm{Jm^{-2}K^{-1}}$ and optimal perturbations (d) in $10^{-6}$ $\mathrm{Ks^{-1}}$.

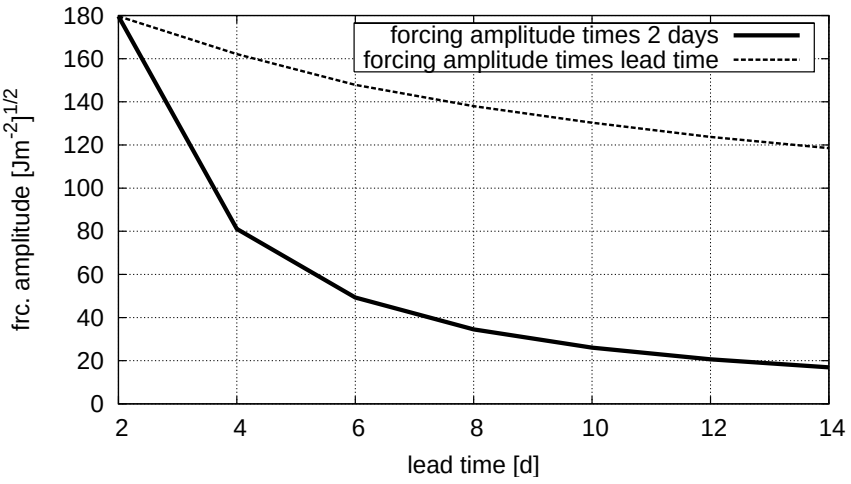


Figure 4.7: Amplitude of the optimal forcing (solid line), and amplitude times lead time (dashed line), measured using the energy norm and as a function of lead time, for the case linearised about climatology $[(\mathrm{Jm}^{-2})^{1/2}]$. For ease of plotting, the amplitude of the forcing in the solid line case is multiplied by 2 days.

scales. We note that the optimal vorticity forcing converted to streamfunction would have the same spatial structure as the sensitivity to vorticity forcing.

We begin by using the adjoint for the model linearised about the winter climatological mean state (part a of the figures) and then go on to consider the adjoint for a tangent linear model linearised about time evolving states (parts b and c of the figures). Results from areas where the flat bottom of the model is in strong contradiction with reality, namely the Himalaya, are omitted. Looking first at the vorticity sensitivity for level 3 (at about 500 hPa) shown in Fig. 4.4a, we see what looks like a Rossby wave train originating over the tropical western Pacific south of our cut-off latitude of 20°N. This feature is present at other model levels and has corresponding features in the forcing sensitivities for other variables. It is reminiscent of a Rossby wave source (*e.g.* Sardeshmukh and Hoskins 1988) and is in a similar (though not identical) position to the Rossby wave source identified by Greatbatch and Jung (2007) as being effective in forcing the positive NAO in the ECMWF model. Nevertheless, it is important to realise that what is plotted is forcing sensitivity and so is not actually a Rossby wave itself. Rather, the adjoint technique selects the optimal forcing that excites a model response with a given projection onto the trend pattern. It follows that if a Rossby wave train emitted from the tropical Pacific is a potentially important part of the trend, then the adjoint approach will find the most efficient way to excite the Rossby wave train within the given lead time, and this may not be the same way that the Rossby wave train was excited in nature. For example, directly forcing the pattern of the Rossby wave train itself (as appears to be the case here) could well be more efficient than a diabatic heat source in the tropical Pacific, even if

in reality the latter were the physically relevant forcing perturbation. It should also be noted that the way the model finds it most efficient to excite a particular feature probably also depends on the resolution of the model.

Nevertheless, a Rossby wave source in this region is broadly consistent with the finding of Lu *et al.* (2004) that forcing from the tropical Indo-Pacific region is important for driving the target pattern (i.e. the 51 year trend). The importance of forcing over the western tropical Pacific for driving the trend has also been noted by Kucharski *et al.* (2006) in forward model runs using a simplified GCM.

In addition to the Rossby wave feature, Fig. 4.4a also exhibits an annular pattern with implied positive vorticity forcing over the polar region and implied forcing of the opposite sign around the 30°N latitude belt, indicative of forcing for the positive phase of the Northern Annular Mode (or Arctic Oscillation, Thompson and Wallace 2000). The annular forcing feature is even clearer in the top model level vorticity forcing sensitivity (Fig. 4.5a), although the Rossby wave feature can be seen here too. Looking at the sensitivity for temperature in the top model level (Fig. 4.6a), we again see both the annular mode-type forcing pattern, with cooling over the pole and warming at lower latitudes, and the Rossby wave-type pattern originating from the tropical western Pacific. It is possible that the presence of the annular mode-type forcing in the uppermost model levels mimics influences from the stratosphere. Such a view is consistent with the work of Scaife *et al.* (2005) who have argued an important role for the stratosphere in explaining the trend. Other features in parts (a) of Figs. 4.4 to 4.6, such as the large forcing anomaly over east Africa in Fig. 4.5a, become less important when time-evolving trajectories are considered, as we discuss next.

Next we turn to forcings derived using the tangent linear model linearised about time-evolving trajectories. We begin by using trajectories obtained by projecting daily mean realisations from the NCAR/NCEP reanalysis onto the model grid. Each 12 day-integration using the adjoint model yields sensitivity fields which are then averaged to produce a "composite" sensitivity to forcing and this "composite" sensitivity is then tested for significance against the null hypothesis of zero sensitivity (for a discussion on how the corresponding forcing perturbation is derived from average of the sensitivities, see Section 4.2). Here we use 1000 partly overlapping trajectories, each using a different daily realisation as the initial condition. The results are shown in part (b) of Figures 4.4 to 4.6. We have also considered a subset of trajectories selected on the basis that the trajectories terminate with a strong projection on the target pattern (see Figure 4.3). The results for this subset are basically the same as for the case using all available trajectories and are not discussed further here. To ensure that the mean of the sensitivities is actually meaningful, *i.e.* , has bounded variance, we checked the ensemble distribution of the sensitivities at a few individual gridpoints and found them to be reasonably Gaussian. To get a more complete picture, we compared ensemble mean and ensemble median of the sensitivities and found the corresponding maps to be largely similar, with differences

attributable to the skewness of the distributions. In the figures, regions where the sensitivity is significantly different from zero at the 10% level are shaded (light grey: positive; dark: negative; independence was assumed). It is immediately clear that the main features in parts (b) are the same as in part (a) of the figures, indicating that linear dynamics, linearised about the winter climatological mean state, is an important aspect of the dynamics of the 51 year trend in this model, consistent with Lu *et al.* (2004). We can investigate this further using trajectories taken from a fully non-linear, time-evolving model run, rather than based on observations. Here, the model run uses time-independent climatological forcing, as in Hall (2000), and corresponds to the same model set-up that forms the basis for our adjoint model. Again, 1000 trajectories are used. The results are shown in part (c) of the figures, together with the corresponding optimal forcing perturbation in part (d) (the amplitude of the latter being determined as for the case linearised about NCAR/NCEP trajectories). The sensitivities are again found to be very similar to those shown in parts (a) and (b), except that compared to the cases linearised about NCAR/NCEP trajectories (part b), there is an increase in the area where the forcing sensitivity is significantly different from zero, reflecting the reduced spread of the trajectories taken from the model compared to those based on observations. It is interesting that when linearising about time-evolving trajectories, the Rossby wave-type feature from the tropical Pacific is reduced in amplitude compared to the annular forcing pattern in the top model level (Fig. 4.5), especially when using model trajectories (part c). In addition, in Figure 4.4, the part of the Rossby wave feature that extends westward over the Asian continent, as well as the feature over Africa in the case linearised about climatology (part a) is also reduced in importance when using time-evolving trajectories (parts b and c).

Finally in this section we note that the amplitude of the optimal forcings we have derived are not unrealistic. For example, the temperature forcing shown in Fig. 4.6d corresponds to a forcing at 100 hPa of less than 0.2 Kelvin per day and the vorticity forcing in Fig. 4.4d to $\approx 10^{-5}$ per second per day at the maximum.

### 4.3.2 Forward runs using a linear model

We now verify the optimal forcings derived above by using them to drive a model linearised about the climatological winter mean flow. The model is based on the `PUMA` model code and uses the same dissipation parameters as in the fully non-linear model of Hall (2000). In each case, the model forcing is that derived with a lead time of 12 days, and the model, in turn, is run forward for 12 days. Fig. 4.8b shows the response pattern to the forcing diagnosed from the model linearised about climatology. It should be noted that the amplitude of the forcing used to produce Fig. 4.8b is determined from Eq. (4.9) with $\delta I$ equal to the projection (using the energy norm) of the target on itself (this choice is made so that the amplitude of the model response can be compared with Figure 4.1, repeated for

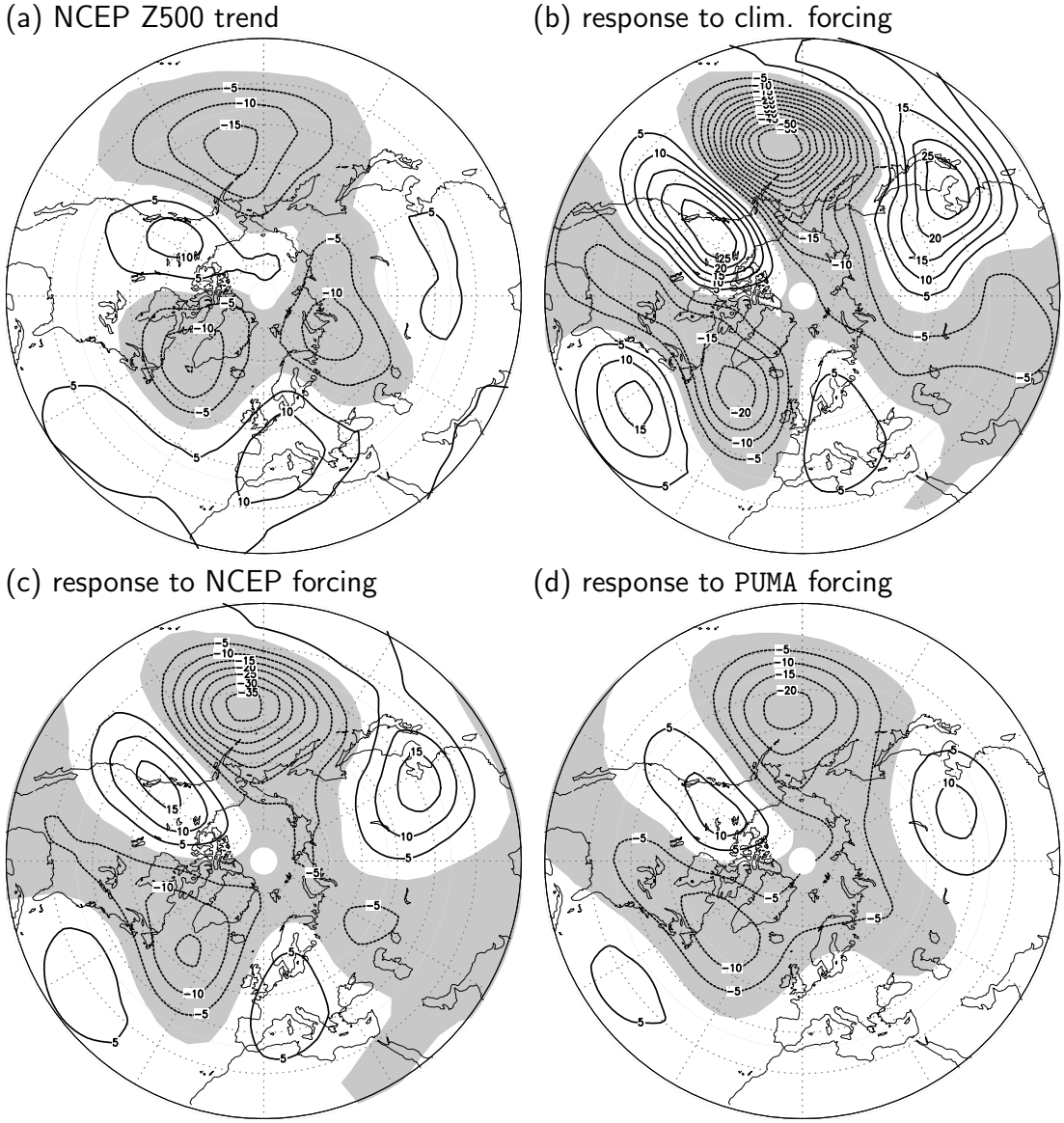


Figure 4.8: **(a)** Linear trend in 500 hPa height from Figure 4.1, **(b)** 500 hPa-response in a 12d-run linearised about NCAR/NCEP climatology to the optimal anomalous forcing. The forcing is scaled to produce the same projection as the trend projected onto itself. The amplitude of the response is 2.2 times larger than the target pattern, and the pattern correlation is 0.46. **(c)** The same for the anomalous forcing derived from averaged sensitivities using the NCAR/NCEP trajectory. With the forcing scaled as in the optimal case the response reaches a relative amplitude of 1.4, the projection on the target is 73 %, and the pattern correlation is 0.55. **(d)** The same for the anomalous forcing derived from averaged sensitivities using a PUMA trajectory. With the forcing scaled as in the optimal case, the response reaches a relative amplitude of 0.91, the projection on the target is 54 %, and the pattern correlation is 0.59. Contours are every 5 m(10 yr)$^{-1}$ and negative regions are shaded.

convenience as Fig. 4.8a). If we define correlation and amplitude using the energy norm, the model response has a correlation of 0.46 with the target pattern, but a larger amplitude by a factor of 2.2. By construction, for this case the projection onto the target is 100 %, corresponding to the projection of the target onto itself. The main centres of action are reproduced, but with some shortcomings over Asia and southern North America and with the amplitude of the Aleutian low overemphasised. The fact the model does not reproduce the target pattern exactly is because "optimality" of the derived forcing perturbation is measured in terms of projection onto the target using the energy norm and does not require that the model response correspond exactly to the target itself. Chiefly the result is a mathematical compromise between the growth rate of internal modes and their respective pattern correlation with the target. Fig. 4.8c shows the model response to the forcing derived from the average of the sensitivities obtained using trajectories derived from the NCAR/NCEP reanalysis. The amplitude of the forcing in this case is chosen to be the same as the amplitude of the forcing used to produce Fig. 4.8b. This time the amplitude of the model response is weaker (only 1.4 times that of the target amplitude), but the correlation is increased to 0.55. On the other hand, the projection on the target is 73 % of the projection of the target on itself. The reduced projection is an indication that the forcing is less efficient at exciting the target than the previous forcing for the particular model being used here (that is a model linearised about climatology). We have also used forcing derived from the time-evolving model trajectories (see Fig. 4.8d), where the amplitude of the forcing is again the same as the amplitude of the forcing used to produce Fig. 4.8b. In this case, the model response has even less amplitude (0.91), a slightly higher correlation (0.59), but an even smaller projection on the target of 54 % of the projection of the target on itself, indicating that the forcing in this case is even less efficient at exciting the target pattern for the particular model used here (that is, linearised about climatology).

### 4.3.3 Forward runs using a nonlinear model

We now turn to forward model runs that use the fully, nonlinear dynamical model, in this case the model of Hall (2000), except that the model core uses the `PUMA` model code. The model forcing is the climatological mean forcing used by Hall (2000), with the climatological forcing perturbed by the forcing derived using the adjoint model. For the model runs shown here, different perturbed forcings are considered using different amplitudes and derived using different lead times. In all cases, the perturbed forcing is derived from the tangent linear model applied to model trajectories, as in Fig. 4.8d described above, as this is the forcing considered most consistent with the model dynamics. For each particular choice of forcing, an ensemble of 30 model runs is created, each ensemble member being initialised with a random realisation from the NCAR/NCEP reanalysis projected onto the model grid and run for 6 months with only the last 3 months being used for

(a) ens. mean response, pos. forcing (b) ens. mean response, neg. forcing

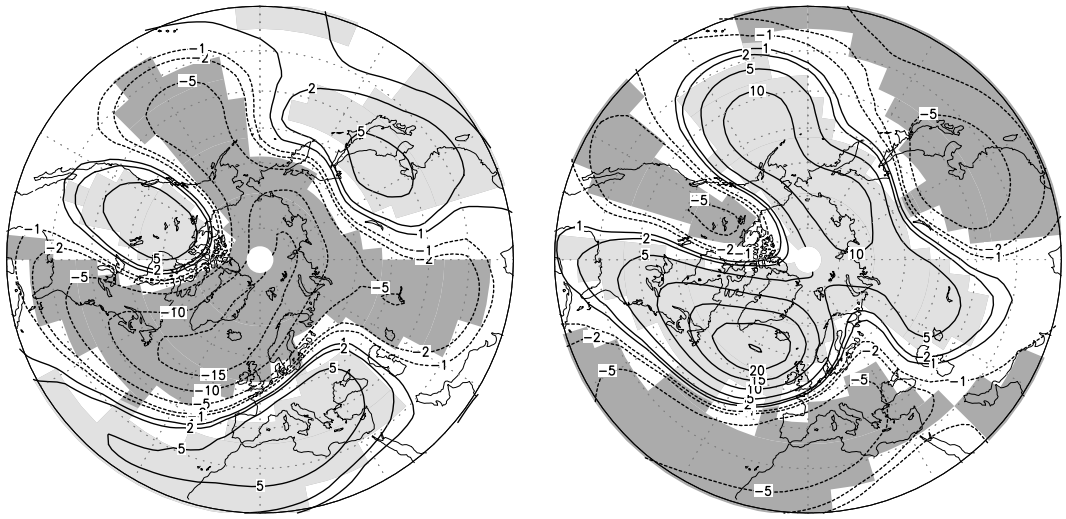

Figure 4.9: Ensemble mean response to forcing derived in a nonlinear run. Shown is 500hPa-geopotential height difference from a control ensemble, significant on the 10%-level. The forcing was scaled to yield the same projection in a linear run as the full observed trend and the result was divided by the number of decades to make it comparable to Fig. 4.1. **(a)** for positive, **(b)** for negative forcing. Contours are at 1, 2, and then every 5 m, significant positive (negative) areas are shaded in light (dark) grey.

(a) 12 days lead

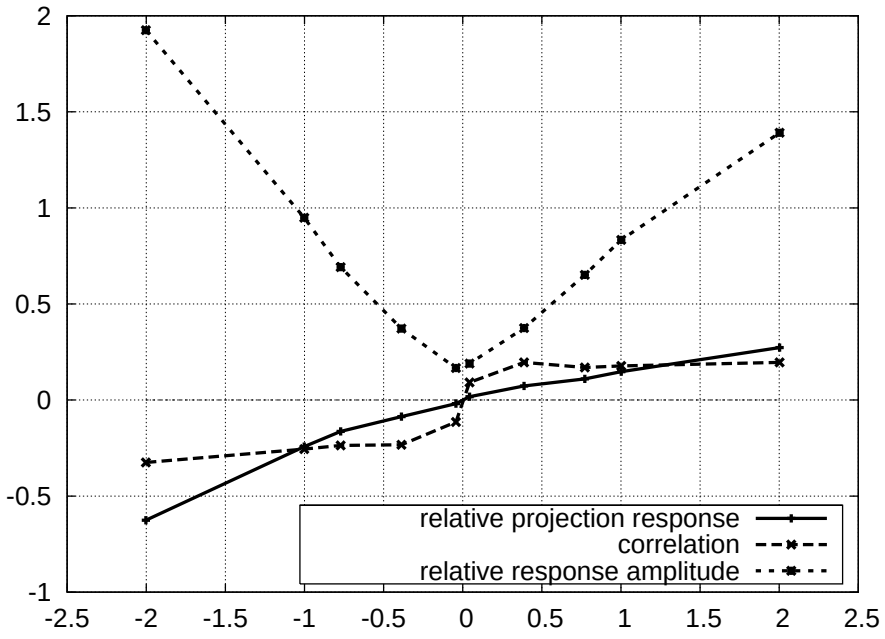


(b) 6 days lead

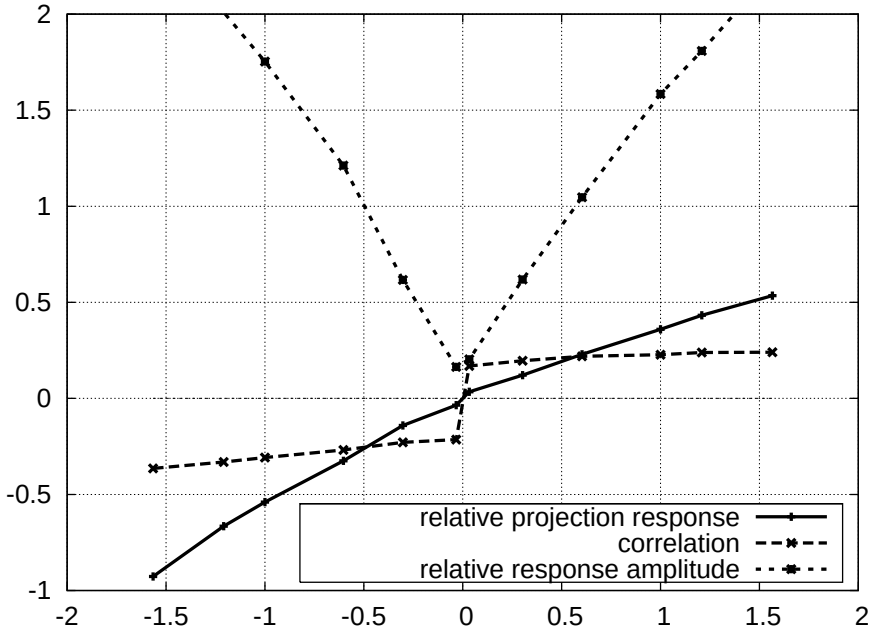


Figure 4.10: Responses in nonlinear runs to anomalous forcings optimal for lead times **(a)** 12 days and **(b)** 6 days. The x-axis gives the amplitude of the applied forcing relative to the respective optimal forcing in the fully linear experiment. The y-axis is scaled with the projection of the full trend onto itself (except for correlation). We show projection onto the trend (solid line), correlation with the trend (dashed), and amplitude of the response measured in the energy norm (dotted).

analysis. For comparison with the perturbed runs, a control run is also carried out using climatological forcing only (the perturbed forcing is zero), this time using 100 ensemble members. Fig. 4.9 shows the ensemble mean model response to the perturbed forcing (perturbed forcing minus control) when the amplitude in terms of the total energy norm of the perturbed forcing is the same as used to produce Fig. 4.8d. Positive and negative forcing cases are shown. The same basic structure is seen when the amplitude is reduced to 1/3 of that used here, or if forcing derived for a lead time of 6 days is used, rather than the 12 days lead time used here. We see that the ensemble mean model response is quite similar (but with the sign reversed in the negative forcing case) to both that of the target pattern (Fig. 4.8a) and of that produced by the linear model (Fig. 4.8d), indicating that forcing derived using an adjoint with a lead time of days (in this case 12 days) can systematically excite a pattern similar to that of the target when applied in a non-linear dynamical model. Compared to Fig. 4.8d, the model response in the nonlinear case shows a weakening of the Aleutian low and a deepening of the Icelandic low features. Figs. 4.10a and b show plots of amplitude, correlation and projection (using the energy norm and where projection is relative to that of the projection of the target pattern on itself) for different amplitudes of the forcing, where 1 on the abscissa corresponds to the forcing amplitude used in the linear model run shown in Fig. 4.8b. The fact that the correlations are roughly constant either side of zero indicates the model response is rather linear with increasing amplitude of the forcing. We also see that the amplitude of the model response also increases with an increase of the forcing amplitude, although this increase is steeper for the negative forcing cases. Likewise, the projection suggests essentially linear behaviour. Using forcing derived with a lead time of 6 days gives similar results (see Fig. 4.10b).

As noted in the introduction, previous studies (*e.g.* Corti and Palmer 1997 and Jung and Barkmeijer 2006) have shown that nonlinear models, perturbed by forcing derived using an adjoint model with a lead time of days, show a systematic tendency to excite the corresponding target pattern. Our results confirm this effect. We suggest that the connection between forcing derived using lead times of, say, 10 days, and forcing that systematically excites a pattern in an ensemble mean sense on climate time scales, arises because the dissipation time scale in the atmosphere is typically measured in 10's of days, a time scale comparable to the lead times we have considered. Nevertheless, a close comparison between Figs. 4.8d and 4.9a shows that in the nonlinear runs, the anomalies associated with the Aleutian low tend to be weaker than in the linear model runs, whereas the anomalies associated with the Icelandic low tend to be increased for both positive and negative anomalous forcing (most likely due to systematic forcing from the eddies in the nonlinear runs). In addition, the features in the ensemble mean response tend to be shifted slightly eastward in their positions compared to their linear counterparts.

### 4.3.4 Forcing restricted to parts of the model domain

We begin by examining the role played by the Rossby wave feature noted in the forcing sensitivities (Figs. 4.4 to 4.6), and which originates in the western tropical Pacific region. To do this, the forcing perturbations for all model variables diagnosed using the PUMA model trajectories are restricted to the Western Tropical Pacific (WTP: 30°S to 30°N and 120°E to 210°E); see Fig. 4.4c, d). This part of the forcing contributes 18 % of the energy (measured using the squared energy norm) of the total forcing in all variables. Fig. 4.11a shows the response of 500 hPa height to this forcing in the model linearised about winter climatology. It accounts for 12 % of the projection of the response to full forcing onto the target pattern with a pattern correlation of 0.24. As expected, the model response shows a wave train emanating from the western tropical Pacific and extending across North America, not unlike the pattern shown in Lu *et al.* (2004, Fig. 5d, e) when their model forcing was restricted to the western tropical Indo-Pacific region, but with the centres of action slightly shifted. These results confirm the importance of the Rossby wave feature in the forcing sensitivities for exciting this part of the trend pattern, supporting claims by a number of authors (*e.g.* Hoerling *et al.* 2004; Hurrell *et al.* 2004; Lu *et al.* 2004; Kucharski *et al.* 2006). We now restrict the anomalous forcing (forcing for all variables) to the top model level (about 100 hPa). The response of the linear model about climatology is shown in Figure 4.11b. The model response accounts for 28 % of the projection of the full response onto the target with a pattern correlation of 0.56. In this case, the model response is very similar to that of the trend pattern itself, but with reduced amplitude, and captures the features of the trend pattern over the Euro-Atlantic/Asian sector not accounted for by the Rossby wave-type forcing (cf. Figure 4.11a).

The importance of the forcing in the top model level for driving an annular-type response can be seen in Figure 4.12a. Here the ensemble mean response of the nonlinear model (ensemble minus control, as before) is shown for the same forcing as used to produce Figure 4.11b. Interestingly, the amplitude of the model response is greatly increased in this case compared to the linear model run, and is about two thirds of the amplitude when the full anomalous forcing is used (cf. Fig. 4.9). This suggests that synoptic eddies in the troposphere can act to amplify signals that are imposed on the troposphere from the overlying stratosphere (albeit in the very simple model setting being used here). For the case shown, the amplification is by a factor of up to 5 compared to the linear model; indeed the model response over the North Atlantic in this case is comparable to that in the trend pattern itself (Figure 4.1). Our results therefore provide some corroboration for the finding of Scaife *et al.* (2005) that imposing the observed trend on the stratosphere in a model can drive a trend similar to that observed in the troposphere over the Euro-Atlantic sector. We note, however, that although the model response in this case implies a deepening trend for the Icelandic low,

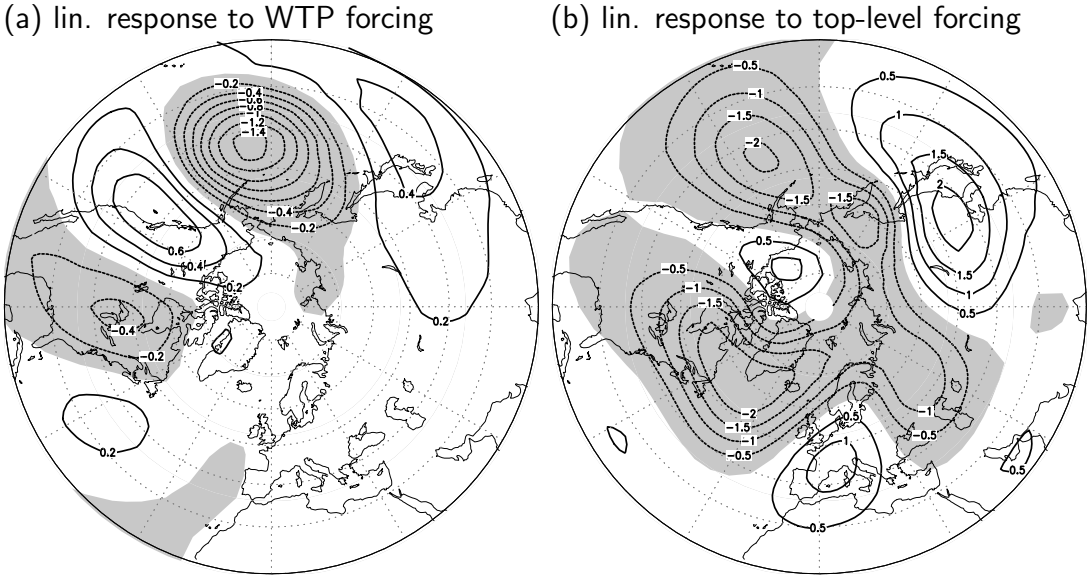


Figure 4.11: Same as Fig. 4.8d but with the anomalous forcing restricted to **(a)** vorticity in the second-to-top (300 hPa) model level in the Western Tropical Pacific (30°S to 30°N and 120°E to 210°E), and to **(b)** vorticity, divergence, and temperature in the top model layer (about 100 hPa).

similar to what was observed, the opposite trend is implied in the North Pacific; that is a trend towards a less deep Aleutian low than in climatology and the opposite to what was observed. Interestingly, the spatial pattern associated with the northern annular mode also shows a weakened Aleutian low together with a deepened Icelandic low (Thompson and Wallace 2000). Clearly further studies using higher resolution model versions (especially higher vertical resolution) will be required to explore further the role played by the stratosphere in the trend. We also show the response of the nonlinear model to the negative of the forcing used to produce Figure 4.12a. In this case (Figure 4.12b), the model response is similar in both pattern and amplitude to the negative of the response in Figure 4.12a, suggesting that a negative trend in the stratosphere can excite a similar negative trend in the underlying troposphere. Finally, for completeness we show the result of two nonlinear model runs using both signs of the forcing used to produce Fig. 4.11a. In this case (Figure 4.12c,d), the nonlinear model leads to some distortion of the linear model response, but with similar amplitude, and will not be discussed further here.

## 4.4 Summary and discussion

In this chapter, we have applied a tangent linear adjoint model in an effort to clarify aspects of the forcing for the trend in the northern hemisphere winter

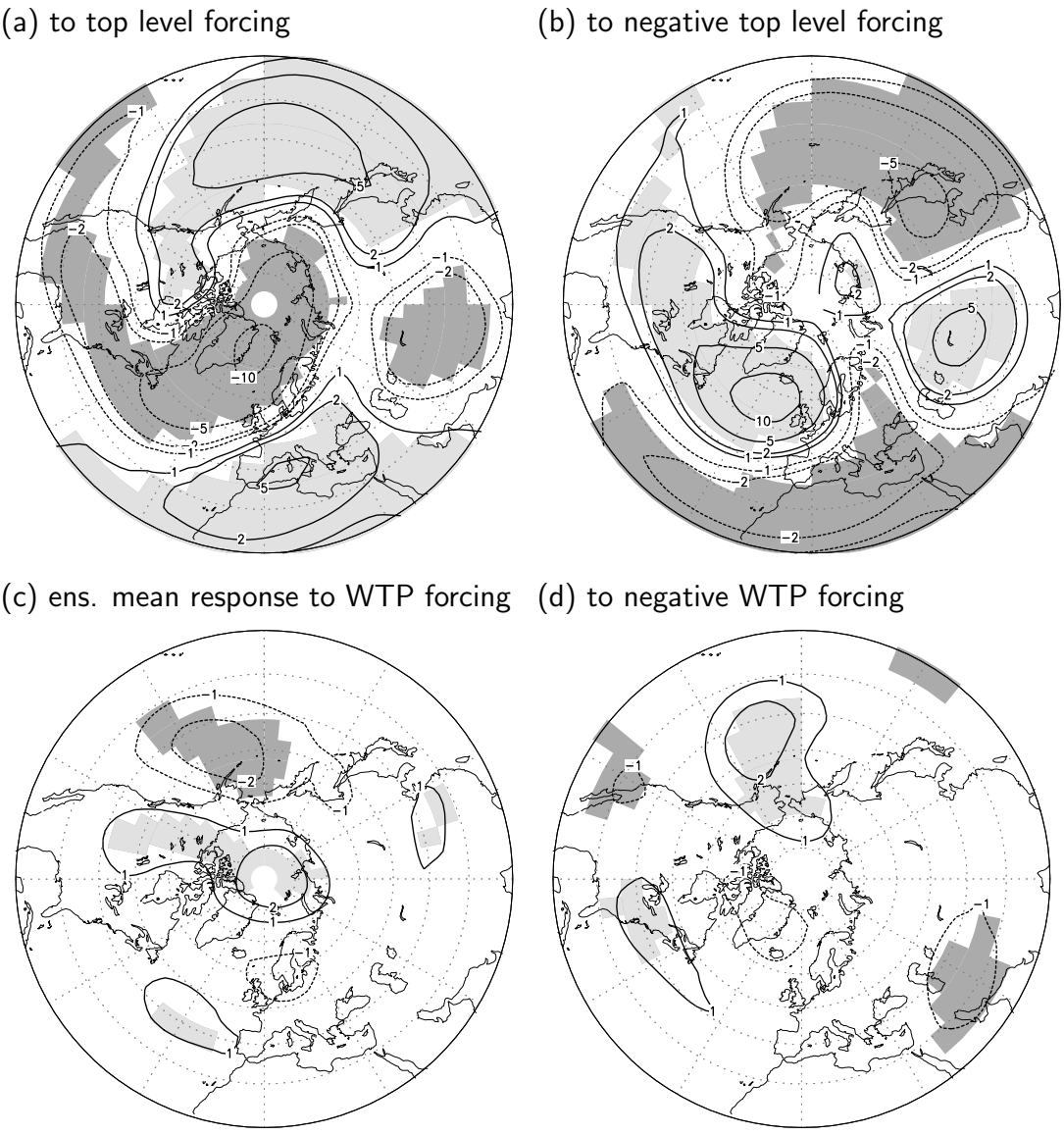


Figure 4.12: As Fig. 4.9 but with the anomalous forcing restricted to **(a)** to vorticity, divergence, and temperature in the top model level (about 100 hPa), **(b)** as (a) but with reversed sign, and **(c)** vorticity at the second-highest model level (300 hPa) in the Western Tropical Pacific (30°S to 30°N and 120°E to 210°E), and **(d)** as (c) but with reversed sign.

tropospheric circulation, 1948-1999. In particular, we have taken as a target pattern the 51 year trend restricted to the region north of 20°N, and asked what is the optimal forcing that excites this target with different lead times. The modelling system we use is the `PUMA` model developed at the University of Hamburg (Fraedrich *et al.* 2005) and the set-up and model parameters we use are the same as in Hall (2000) and Lu *et al.* (2004). In particular, we use T21 horizontal resolution with 5 levels in the vertical. In the fully nonlinear (forward) model runs, the forcing for the unperturbed control integration is the same as used in Hall (2000) and leads to a realistic northern hemisphere winter climate. In these runs, the optimally-derived forcing is added as a perturbation to the climatological forcing using a range of amplitudes and lead times. For two different lead times (6 and 12 days), and for a range of both positive and negative amplitudes, we find that application of the derived forcing shows a systematic tendency (in an ensemble mean sense) to reproduce the target pattern (with negative amplitude if the forcing is negative). We also verified the derived forcing using forward runs with a model linearised about climatology, again showing the tendency of the model to produce the target pattern. This is true both for forcing derived from a model linearised about climatology, and for forcing that is the average of sensitivities derived from a tangent linear model in which the trajectories are taken either from observations (projected on the model grid) or from a nonlinear model run with climatological forcing. It is clear from the results that the essence of the forcing sensitivities is captured by the case linearised about climatology, although using averaged sensitivities from time-evolving trajectories of either observations or the nonlinear model generally simplifies the forcing sensitivities (*e.g.* by reducing the forcing sensitivity over the Asian continent and Africa in part (a) of Figs. 4.4 to 4.6).

The optimal forcing we have derived indicates the importance of forcing from the tropical Indo-Pacific region, as in Lu *et al.* (2004), especially for the deepening trend of the Aleutian low, consistent with Hurrell *et al.* (2004) and Hoerling *et al.* (2004). The optimally derived forcing for the top level is also suggestive of forcing for the Northern Annular Mode (or Arctic Oscillation), related to influences from the stratosphere. By restricting the forcing to specific parts of the model domain, we are able to confirm the ability of forcing over the tropical Pacific region to force the North Pacific part of the trend. We also find that the annular mode-type forcing is effective at exciting the trend pattern in the Euro-Atlantic/Asian sector. It is particularly interesting that a nonlinear model run, with the perturbed forcing applied only to the top model level, excites an annular mode-type response of similar amplitude and of the right sign as the observed trend in the Euro-Atlantic/Asian sector, but of opposite sign over the North Pacific sector. This result lends support to Scaife *et al.* (2005) who have argued an important role for the stratosphere for explaining the observed trend over the Euro-Atlantic sector. Furthermore, it is possible that the stratospheric trend itself could be a consequence of the upward trend in tropical SST during the

last half of the 20th century, rather than being of internal stratospheric origin, an issue for further study. If this is the case, then the stratosphere could act as a "bridge" linking forcing in the tropical Indo-Pacific region to the Euro-Atlantic/Asian sectors.

Finally we note that the adjoint approach outlined in this chapter finds only the optimal forcing perturbation that gives a model response with a given projection on the target pattern. This means, for example, that forward model runs to which the derived forcing is applied are not guaranteed to reproduce the target pattern exactly, even when the forward model is linear (a good example can be seen by comparing Figure 4.8b with 4.8a). More importantly, the derived forcing perturbation need not be representative of the forcing perturbation that actually generated the target pattern in nature. For example, Gritsun and Branstator (2007) find that a diabatic heating anomaly over the Indian Ocean is important for driving the positive phase of the Northern Annular Mode in their model, a result that is consistent with the work of Hoerling *et al.* (2004). Yet such a diabatic heating anomaly is not extracted by our adjoint technique, suggesting that it is not "optimal". Nevertheless, we believe our work shows how a tangent linear adjoint can successfully be applied to the understanding of a climate response problem, even though the theoretical underpinning is linear with lead times of order 10 days.

# Chapter 5

# Overall summary and outlook

## 5.1 Summary

This work has demonstrated how gradients with respect to different model quantities, namely process parameters (section 3.2), a temperature relaxation field (section 3.3), and forcing fields (chapter 4), can be used for climate related problems. While the first two have their focus on the realisation of a Climate Prediction Data Assimilation System (CPDAS Kaminski et al., 2007), the third one is a demonstration of the application of an adjoint model as a diagnostic tool in an investigation of climate sensitivity.

In section 1.4 the principal problem of adjoint gradients for minimisations derived with long lead-times (*i.e.* climate-related), is outlined. Basically, systems with instabilities show exponential growth of the sensitivities with increasing lead-time. These steep gradients can be identified as the slopes of the sides of narrow secondary minima of the cost function. In the literature three methods are suggested to mitigate this problem for a given cost function. Firstly, using a coarse resolution model excludes, linearises (via parameterisations), or damps small scale processes which can have growth properties deteriorating an adjoint approach. This approach is followed in principle by using the T21 version of `PUMA` in all the later chapters. Secondly, averaging of the gradients over intermediate lead times is supposed to combine accurate local sensitivity information from different places of the model state space. The third approach, which is tracking the location of the minimum for successively increased lead-times, is discarded, since it cannot be guaranteed that such a minimum does not develop into a secondary minimum (*e.g.* Fig. 1.4). Some techniques which modify the cost function itself in order to reduce secondary minima were tested in section 3.2.4.

The good correspondence of finite differences and adjoint gradients of process parameters on timescales up to one year encourage the use of the relatively coarse resolution (T21) atmospheric model `PUMA` in a CPDAS, showing that the gradients do not degenerate on that timescale. Secondary minima of the cost function

which appear after tens of days are a concern, which call for the application of mitigation techniques. From the three suggested techniques (averaging, coarse resolution, minimum tracking; cf. section 3.2.5), a combination of the first two is successfully used for climate assimilation (section 3.3) and trend sensitivity diagnosis (chapter 4).

The assimilation of a climate into the model by means of an adjoint adjustment procedure for a relaxation temperature field in section 3.3, is a prototype for a CPDAS. Limitations for such a future coupled assimilation system would mainly arise from the short timescales of most atmospheric processes. Therefore, the successful demonstration with the atmospheric component has encouraging implications for the whole system. The experiment demonstrates that the combined information of model dynamics and a spacial distribution of the mean temperature can contain enough information to reconstruct main aspects of a historical climate, including second moments. On the technical side, the averaging of gradients over different realisations has proven successful to avoid secondary minima far away from the known solution. The remaining uncertainty reflects the internal fluctuations of the model climate. It remains a question for future studies whether comparable results can be achieved for a model of increased resolution.

A different perspective is the diagnostic value of adjoint sensitivities for climate related diagnosis. Chapter 4 demonstrates this for the example of the atmospheric trend in the northern hemisphere during the last half of the $20^{th}$ century. Sensitivity maps can help to identify important processes which have the potential to amplify small and regional changes. The presented method uses an ensemble of linearisations around observed trajectories (*i.e.* NCEP reanalysis, sequences of atmospheric states) in order to account for the time dependence of sensitivities. Moreover this ensemble adjoint approach ensures that nonlinear processes present in the observations can be captured to some degree. For the generation of sensitivity maps statistical models have been applied in the literature (*e.g.* Gritsun and Branstator, 2007, and references therein). The advantage of the presented adjoint approach is, apart from its computational efficiency, the combination of observed data with dynamical principles from the model equations. This drastically reduces the amount of data needed for the reliable diagnosis of a dynamical dependency.

With such applications in mind, appendix A shows how the adjoint modelling and diagnosis system built around `PUMA` in the course of this work (see appendix B.5 for details) can be used to determine sensitivities to Isentropic Potential Vorticity. This is a feature suggested before (Arbogast 1998; Romero *et al.* 2005 for Quasi-Geostrophic PV), but not previously realised for a Primitive Equations model.

## 5.2 Future improvements and outlook

Many aspects of this study lead to further questions for future investigation. For instance the dependence on resolution of the sensitivity growth with increasing lead time was rather assumed than demonstrated, merely justified from the literature (Köhl and Willebrand, 2002; McLay and Marotzke, 2008) or the suppression of non-linearity by increased viscosity and diffusivity used to bound adjoint gradients by Hoteit et al. (2005). Next to runs with higher resolutions, a model domain vertically extended to the stratosphere and inclusion of orography are further points on a wish list for subsequent studies. A severe limitation in the investigations of the trend in chapter 4 is the use of a flat bottom. A large fraction of the sensitivities had to remain uninterpreted since it was unclear whether they reflected the lack of orography in the model or an actual atmospheric mechanism. Also, for convenience only daily values were used in the reference trajectory which can be expected to reduce the detected influence of eddie fluxes to some extent. By careful comparison of available atmospheric re-analysis products, it is doubtful whether the choice of the NCEP re-analyses is optimal. Nonetheless it was apt to demonstrate the technical capabilities of the adjoint diagnostic with `PUMA` in combination with trajectories from a far more complex model. For experimental purposes, a mean state with orography from ERA-40 re-analyses (Uppala, 2003) was already successfully interpolated onto the model grid and used in the `PUMA` sensitivity software.

As elegant as the adjoint sensitivity calculations seem at first, we still ended up doing an ensemble of adjoint runs in chapter 4 as a consequence of the non-linearity of the problem. Nonetheless, the gain in effectivity compared to systematic sensitivity computations via perturbed forward runs is still substantial since the adjoint approach yields a full gradient vector in a single run, while a perturbed forward run of the non-linear model produces a single component of the gradient vector and would still require ensemble averaging in order to reflect the sensitivity of the system's climate rather than an instantaneous value. This raises the question of an estimate for the required size of an adjoint ensemble at a given lead time. This would be helpful for the layout of applications using ensemble adjoint sensitivities. To some degree confidence is tested by the hypothesis test applied to the sensitivities in section 4.3.1, showing that under the assumption of independence the chosen size was at least sufficient. A more instructive theoretical treatment of the link of predictability, Lyapunov exponents, local growth properties and sensitivities could be of value for this aim.

Initial state sensitivities reflect to a large degree the model's treatment of gravity waves and numerical phenomena. It has been demonstrated that the time step is influential on the computed sensitivities (not included). Therefore all adjoint runs in this work use a time step half as long as recommended for the forward model with identical resolution.

An idealised test case for the demonstration of the computation of sensitivity

to isentropic potential vorticity is still missing and is prerequisite to the application of this feature in future work.

Future development could be a stepwise extension of the assimilation system from simple to complex, building on earlier studies (*e.g.* Lee et al., 2000). Being the atmospheric component of the Planet Simulator (PlaSim, Fraedrich et al., 2005a), `PUMA` could be extended by adding component by component of the climate system. This would include coupling to ocean models of increasing complexity, for instance a slab ocean, a shallow water ocean, and ultimately the MIT ocean model, for which an adjoint version is maintained (Heimbach et al., 2005). Also, experiments will be required to understand the effect of simultaneously present slow and fast components in coupled experiments on sensitivities.

In contrast to assimilation in numerical weather prediction, the assimilation of a climate into a coupled system will need to find optimal values for model parameters from the parameterisations, which contain many variables which even for present day conditions cannot be measured in nature. While such initial conditions as albedo and ocean state will clearly be important to the simulations, the exact initial atmospheric state will, quite contrary to weather prediction purposes, be of secondary importance (Tziperman and Sirkes, 1997).

The use of adjoints as diagnostic tool in climate science also bears potential for future research. One option would be the application to conceptual studies of the dynamics of circulation patterns, for instance the link of tropospheric wave breaking, the North Atlantic Oscillation and the stratosphere (Scaife et al., 2005; Blessing et al., 2005; Kunz et al., 2008b, and references therein). Since the wave-breaking is conveniently shown in terms of isentropic potential vorticity maps, sensitivity with respect to this quantity could be particularly useful. Also other cases could be investigated in more realistic setting (using re-analysis data as reference trajectory) where a link between atmospheric phenomena and their potential precursors was suggested by other studies, *e.g.* sea surface temperatures and Rossby-waves (Hoskins and Karoly, 1981).

One of the known sensitivities of the ecosystem are so-called *hot spots* which are geographically small regions containing a large fraction of earth's current biodiversity. A coupled adjoint simulation system would call for an attempt to determine the origins of climatic changes which have strong impact on the *hot spots* in an adaption of the diagnostic technique outlined in chapter 4. Again, this can also be applied to model parameters and serve for the diagnosis of consequences of parameter uncertainties for climate and subsequent ecosystem change predictions which in turn could direct attempts for the reduction of these uncertainties to the most relevant and influential subset.

# Acknowledgements

The research for this work has been carried out in most parts in the research projects KiHZ and SFB 512, funded by the Deutsche Forschungsgemeinschaft. The interpolated NCAR/NCEP reanalysis data and the Hall-model forcing were provided by Dr. Hai Lin at McGill University in Montreal, Canada.
I am grateful for the continuous support of my supervisor Klaus Fraedrich. I am also indebted to Richard Greatbatch and the Canadian CLIVAR network whose encouragement and dedication had a great influence on the fate of this work. Another key factor are the many fruitful discussions with Frank Lunkeit. I also express my gratitude to Ron Errico for his dedication and for having published the answers to many of my questions, Ralf Giering and Thomas Kaminski from FastOpt for TAMC and their help and cooperation, Jian Lu for his cooperation with the Hall-model, Hai Lin for the interpolated NCAR/NCEP data, Michael Morgan for sharing ideas and Monty Alexander; Detlev Müller for repeated support, Christian Franzke and David Schröder; Xiaoming Zhai and Rick Danielson for helping with the IPA[1] and various other things, Pingping Rong for hospitality, Pierluigi Pantalone, Andrea Schneidereit and Frank Sienz for trips out of the building; my colleagues Torben Kunz, Frank Sielmann, Annika Jahnke-Bornemann, Martina Junge, Edilbert Kirk, and Stephan Lorenz; the Climate All Stars Stefanie Albert, Gerhard Peters, Sascha Nebel, and Richard Blender; Gregor Knorr for the sportive approach, Hans Langmarck for jelly bears, Alexandra Weiss and Beena Sarojini-Balaan for brightening the sky; Veronika Markshausen and Sabine Bartols for looking after "the ward", Juan Pedro Montavez Gomez and Jesus Fidel Gonzales Rouco for tapas. I am specifically grateful to the people outside the university who enriched my life in the past years and thus indirectly contributed.

[1] India Pale Ale

# Appendix A

# Sensitivity to Potential Vorticity

This appendix is the theoretical outline for an experimental feature incorporated in the code extensions to the adjoint `PUMA`. This feature is implemented as Fortran 90-*module* `arbogast` in the code described in appendix B for both balance conditions described in section A.3 below. They are chosen via a `cpp` switch at compile time. Nonetheless, the current state of the code is still experimental and no rigorous test has been applied.

## A.1 Purpose

In section 4.3.1, the quantity that is used to evaluate the relative contribution of the optimal forcings to the projection on the target pattern is their respective contribution to the energy. By using a projection with unit of energy, it is possible to break down this contribution by gridpoint and variable in the fashion described by Langland *et al.* (2002). The implementation of this mechanism is described in section B.4 of the appendix.

However, this energy perspective on the optimal forcing perturbations or, in other applications, state perturbations, is of limited value for the dynamical evaluation of the results. Therefore, another idea for the interpretation of sensitivities, is the generation of a derived quantity which depends on all state variables, is invertible at least to some degree, and describes the dynamical properties of the flow. A such quantity is Potential Vorticity (PV).

Sensitivity to potential vorticity combines sensitivity information from the flow field and the pressure and temperature variables into one quantity. A balance condition is used to ensure the uniqueness of the relationship. Therefore sensitivity to potential vorticity also shows the sensitivity to the balanced part of a perturbation. Interestingly, it appears that the same formalism can be applied to the balance condition, yielding the sensitivity to imbalance. There is not much experience with this measure and the role of the PV which enters the formalism in the same way as the balance equation is used for the computation of $PV^{\star}$ is

not yet well explained.
Potential vorticity is conserved on isentropic surfaces. Ertel's potential vorticity is defined as

$$\mathrm{PV} = \frac{1}{\rho}(\boldsymbol{f} + \boldsymbol{\zeta}_\theta)\frac{\partial\theta}{\partial p}, \tag{A.1}$$

where $\boldsymbol{f}$ is the Coriolis term, $\boldsymbol{\zeta}_\theta$ the relative vorticity component perpendicular to an isentropic surface and $\theta$ the potential temperature. The method described here follows the procedure of Arbogast (1998). Rather than constructing the adjoint of the inverse PV diagnosis operator, an iterative procedure is employed, which minimises a cost function using gradient information.

## A.2 Formalism

We start from the expressions for PV and the balance condition. Analysis of the main contributions in Eq. (A.1) lead to (cf. Montani and Thorpe 2002):

$$\mathrm{PV} \approx -g(\zeta + f)\frac{\partial\theta}{\partial p} \tag{A.2}$$

Linearising this with respect to $\vec{V}$ and $\theta$, as

$$\delta\mathrm{PV} = \mathcal{R}_V\delta\vec{V} + \mathcal{R}_\theta\delta\theta \tag{A.3}$$

we get for the $\mathcal{R}$-operators:

$$\mathcal{R}_\theta = \frac{\partial\mathrm{PV}}{\partial\theta} \tag{A.4}$$

$$\mathcal{R}_\theta = -g(\zeta + f)\frac{1}{p_s}\frac{\partial}{\partial\sigma} \tag{A.5}$$

$$\mathcal{R}_{\vec{V}} = \frac{\partial\mathrm{PV}}{\partial\vec{V}} \tag{A.6}$$

$$\mathcal{R}_u = gp_s\frac{\partial\theta}{\partial p}\frac{\partial}{\partial y} \tag{A.7}$$

$$\mathcal{R}_v = -gp_s\frac{\partial\theta}{\partial p}\frac{\partial}{\partial x}. \tag{A.8}$$

We need an additional condition which is equivalent to what is needed when potential vorticity is inverted. With this balance condition $\mathcal{B}$ (see sec. A.3) Equations (A.4) and (A.27) can be written as

$$\begin{pmatrix} \mathcal{R}_u & \mathcal{R}_v & \mathcal{R}_\theta \\ \mathcal{B}_u & \mathcal{B}_v & \mathcal{B}_\theta \end{pmatrix}\begin{pmatrix} \delta u \\ \delta v \\ \delta\theta \end{pmatrix} = \begin{pmatrix} \delta\mathrm{PV} \\ \delta\mathcal{B} \end{pmatrix}. \tag{A.9}$$

The adjoint equation consequently is

$$\begin{pmatrix} \mathcal{R}_u^\star & \mathcal{B}_u^\star \\ \mathcal{R}_v^\star & \mathcal{B}_v^\star \\ \mathcal{R}_\theta^\star & \mathcal{B}_\theta^\star \end{pmatrix} \begin{pmatrix} \mathrm{PV}^\star \\ \mathcal{B}^\star \end{pmatrix} = \begin{pmatrix} u^\star \\ v^\star \\ \theta^\star \end{pmatrix}. \tag{A.10}$$

Multiplying Eq. (A.10) from the left with

$$\begin{pmatrix} \mathcal{B}_\theta^\star & \mathcal{B}_\theta^\star & -(\mathcal{B}_u^\star + \mathcal{B}_v^\star) \\ \mathcal{R}_\theta^\star & \mathcal{R}_\theta^\star & -(\mathcal{R}_u^\star + \mathcal{R}_v^\star) \end{pmatrix} \tag{A.11}$$

yields,

$$\begin{pmatrix} \mathcal{S}_P & \mathcal{B}_\theta^\star(\mathcal{B}_u^\star + \mathcal{B}_v^\star) - (\mathcal{B}_u^\star + \mathcal{B}_v^\star)\mathcal{B}_\theta^\star \\ \mathcal{R}_\theta^\star(\mathcal{R}_u^\star + \mathcal{R}_v^\star) - (\mathcal{R}_u^\star + \mathcal{R}_v^\star)\mathcal{R}_\theta^\star & \mathcal{S}_B \end{pmatrix} \begin{pmatrix} \mathrm{PV}^\star \\ \mathcal{B}^\star \end{pmatrix} = \begin{pmatrix} \mathcal{U}_P \\ \mathcal{U}_B \end{pmatrix}. \tag{A.12}$$

The above symbols are defined as follows:

$$\mathcal{S}_P = \mathcal{B}_\theta^\star(\mathcal{R}_u^\star + \mathcal{R}_v^\star) - (\mathcal{B}_u^\star + \mathcal{B}_v^\star)\mathcal{R}_\theta^\star \tag{A.13}$$

$$\mathcal{S}_B = \mathcal{R}_\theta^\star(\mathcal{B}_u^\star + \mathcal{B}_v^\star) - (\mathcal{R}_u^\star + \mathcal{R}_v^\star)\mathcal{B}_\theta^\star \tag{A.14}$$

$$\mathcal{U}_P = \mathcal{B}_\theta^\star(u^\star + v^\star) - (\mathcal{B}_u^\star + \mathcal{B}_v^\star)\theta^\star \tag{A.15}$$

$$\mathcal{U}_B = \mathcal{R}_\theta^\star(u^\star + v^\star) - (\mathcal{R}_u^\star + \mathcal{R}_v^\star)\theta^\star. \tag{A.16}$$

If in equation (A.12) $\mathcal{B}_\theta^\star$ and $(\mathcal{R}_u^\star + \mathcal{R}_v^\star)$ commutate, then $\mathrm{PV}^\star$ and $\mathcal{B}^\star$ are separated and the first row can be solved independently. To this end a cost function is defined which, when minimised for potential vorticity, indicates the solution of the first row:

$$J = \frac{1}{2}(\mathcal{S}_P \mathrm{PV}^\star - \mathcal{U}_P)^2. \tag{A.17}$$

Its gradient with respect to $\mathrm{PV}^\star$ is given by

$$\nabla_{\mathrm{PV}^\star} J = \mathcal{S}_P^\star(\mathcal{S}_P \mathrm{PV}^\star - \mathcal{U}_P). \tag{A.18}$$

Equations (A.17) and (A.18) can be used in any minimisation algorithm that uses gradient information.
Equally the second row of Eq. (A.12) could be solved for $\mathcal{B}^\star$, if $\mathcal{R}_\theta^\star$ and $(\mathcal{B}_u^\star + \mathcal{B}_v^\star)$ commutate, giving the sensitivity to thermal wind imbalance, $\mathcal{W}^\star$, or using the second definition for $\mathcal{B}$, to divergence tendency, $\mathcal{I}^\star$. The cost function for this case is

$$K = \frac{1}{2}(\mathcal{S}_B \mathcal{B}^\star - \mathcal{U}_B)^2, \tag{A.19}$$

and its gradient with respect to $\mathcal{B}^\star$ is given by

$$\nabla_{\mathcal{B}^\star} K = \mathcal{S}_B^\star(\mathcal{S}_B \mathcal{B}^\star - \mathcal{U}_\mathcal{B}). \tag{A.20}$$

If this separation is not possible, as for the chosen wind balances in this chapter, Eq. (A.10) or (A.12), can still be solved for adjoint potential vorticity and adjoint balance together, using the same numerical approach as outlined above, but with a two-component vector as control variable, consisting of PV$^\star$ and $\mathcal{B}^\star$.

For the construction of the adjoints and the transformation of the model variables of the adjoint `PUMA` model the following relationships are required:

$$\vec{V}^\star = \begin{pmatrix} \partial_y & -\partial_x \\ -\partial_x & -\partial_y \end{pmatrix} \begin{pmatrix} \zeta^\star \\ D^\star \end{pmatrix}, \tag{A.21}$$

$$T = \theta \left( \frac{p}{p_{ref}} \right)^{R/c_p} = \theta \left( \frac{\sigma}{p_{ref}} \right)^{R/c_p} p_s^{R/c_p} \tag{A.22}$$

$$\theta^\star = p_s^{R/c_p} \left( \frac{\sigma}{p_{ref}} \right)^{R/c_p} T^\star - \frac{c_p}{R\theta} \left( \frac{T}{\theta} \right)^{c_p/R} \frac{p_{ref}}{\sigma} p_s^\star. \tag{A.23}$$

$$\tag{A.24}$$

## A.3 Balance conditions

Two balance conditions are available. In a first attempt thermal wind balance is assumed:

$$\frac{\partial \vec{V}}{\partial \ln p} = -\frac{R}{f} \nabla T. \tag{A.25}$$

To make this a scalar quantity $\mathcal{W}$ which measures the degree of imbalance, the divergence of Eq. (A.25) is taken:

$$\mathcal{W} = -\frac{\partial D}{\partial \ln p} - \frac{R}{f} \nabla^2 T. \tag{A.26}$$

Consequently we define:

$$\delta\mathcal{W} = \mathcal{W}_V \delta\vec{V} + \mathcal{W}_\theta \delta\theta \tag{A.27}$$

$$\mathcal{W}_\theta = -\frac{R}{f} \left( \sigma / p_{ref} \right)^{R/c_p} \left( 2\nabla p_s^{R/c_p} \nabla + p_s^{R/c_p} \nabla^2 + \nabla^2 p_s^{R/c_p} \right) \tag{A.28}$$

$$\mathcal{W}_u = -\frac{\partial^2}{\partial \ln p \, \partial x}; \; \mathcal{W}_v = -\frac{\partial^2}{\partial \ln p \, \partial y}. \tag{A.29}$$

In a second step it is required that the perturbations which contribute to the potential vorticity perturbation diagnosed by Eq. (A.3) do not cause a divergence tendency in the model. To this end Eq. (13) of Hoskins and Simmons (1975) is used as a measure $\mathcal{I}$ for $\mathcal{B}$, thus taking advantage of the already coded tangent-linear and adjoint versions of the non-linear divergence tendency contributions and ensuring an approach compatible with the semi-implicit numerics and the angular momentum conserving vertical scheme of Simmons and Burridge

1981 which are used in the PUMA model. Therefore this equation is not treated analytically. The commutativity of the adjoint operators $\mathcal{I}_\theta^\star$ and $\mathcal{I}_{\vec{V}}^\star$ is tested numerically. In the dimensionless notation of Hoskins and Simmons (1975) this balance condition becomes:

$$\mathcal{I} = \mathcal{D} - \nabla^2(\bar{\Phi}^t + \bar{\boldsymbol{T}}\overline{\ln p_s}^t). \tag{A.30}$$

Note that $\mathcal{D}$ contains contributions from the horizontally varying part of the temperature field which formally should be contained in the bracket in order to have separate terms for mass and wind field. $\overline{(\,)}^t$ denotes the current time step. Moreover $\mathcal{D}$ contains centrifugal force and horizontal and vertical advection of momentum.

# Appendix B

# The adjoint modelling environment

In order to embed the adjoint code of `PUMA` into a runnable program, some extensions were programmed which are described in this appendix. It is intended as a reference manual for people actually working with the program. The extensions to the `namelist` input of the regular `PUMA` are documented as well as the available options and formats for input and output to the program. Moreover some fundamental hints about the structure of the program are given in order to enable the reader to interfere with the code and to adapt or extend it to her own needs. For readers not familiar with the handling of `PUMA` and the theory of adjoint models this appendix is not a recommended read.

While the cost function used here is always a projection on some anomaly pattern, the way the gradients are computed offers possibilities which go beyond the applications described in this work. Also note that in the context of data assimilation the *anomaly pattern* is simply replaced by the prediction error. Also note that the applications from chapter 3 represent a different line of development which is not covered in this appendix but is sufficiently described in the respective sections.

All adjoint routines mentioned here are adjoint with respect to the Euclidian scalar product $\langle \cdot ; \cdot \rangle$. It is made heavy use of the definition of adjointness, $\langle \boldsymbol{x}; \mathbf{A}\boldsymbol{y} \rangle = \langle \mathbf{A}^\star \boldsymbol{x}; \boldsymbol{y} \rangle$, mostly for the special case of real matrices, and the relationship $(\mathbf{A} \circ \mathbf{B})^T = \mathbf{B}^T \circ \mathbf{A}^T$; $\mathbf{A}$ and $\mathbf{B}$ being real valued linear operators, and $\boldsymbol{x}$ and $\boldsymbol{y}$ vectors.

## B.1 Reference trajectory

Every tangent-linear and adjoint run requires a reference trajectory which is the basic state that is used for the linearisation. Three methods were implemented:

- a recalculation with PUMA,
- an externally given trajectory from a file,
- and a constant state from a file.

For the **recalculation** PUMA is run, starting from a restart file and the resulting trajectory is provided to the adjoint run in `direct access` scratch files. The advantage of this method is, that no large files have to be provided externally. On the other hand it is the computationally most expensive variant. These steps are taken care of automatically inside the program if the following `namelist` parameters are set:

```
nrestart=1,
 l_trajectory_in_file=.false., [default]
 l_trajectory_is_const=.false. [default]
```

The **externally given trajectory** is read from a file named "`TRAJECTORY.srv`" which has to be provided by the user. It is a binary file with 32 bit floating point precision in SERVICE[1] format. It contains for every time step and model level the fields of vorticity (code **138**, [$s^{-1}$]), divergence (code **155**, [$s^{-1}$]), temperature (code **130**, [K]), and logarithm of surface pressure (code **152**; only one level, [log Pa]). The following `namelist` parameters must be set:

```
nrestart=0, [default]
l_trajectory_in_file=.true.,
l_trajectory_is_const=.false. [default].
```

If the external trajectory does not exist for every time step, the `namelist` parameter **ntspd_t** must be set to the number of available time levels per day. This results in linear interpolation of the trajectory between the existing time levels. Depending on how integration period and time levels coincide it may be necessary to provide one extra time-level at the end of the integration period in order to have enough information for the interpolation. The **constant reference state** is also read from a file, named and formatted as above. The first time level in this file is used as the time constant reference state. In this way the model is not adjoint to the tangent-linear but to a linearised PUMA. This is the way to go

[1] Fortran-blocked binary file, with alternating header and data fields:

```
integer, dimension (8) ::  i_head !  code,level,date,time,nx,ny,dispo1,dispo2
real, dimension (nx,ny) ::  data !  data field with dimensions nx, ny
open (unit=10,file='data_file',form='UNFORMATTED',access='SEQUENTIAL')
write (10) i_head(:)
write (10) data(:,:)
```

when linearising about a time mean state or a balanced or resting non-evolving state. The following `namelist` parameters must be set:

`nrestart=0`, [default]
`l_trajectory_in_file=.true.`,
`l_trajectory_is_const=.true.`

## B.2 Adjoint Preprocessing

Due to the inverted time direction in the adjoint model, pre- and postprocessing of the adjoint fields requires special attention. Adjoint Preprocessing is used here to describe all steps necessary between the input of the program and the adjoint dynamical model (see Fig. B.1). Mathematically it is the computation of the derivative of the cost function (here a projection index) with respect to the model variables at target time. The target pattern is read from a `SERVICE`-formatted file named `TARGET.srv`. All variables in this file must be defined on the whole model grid on model levels (except for geopotential height, see below). Not all codes and levels need to be present, and some are mutually exclusive. The codes mostly are derived from the naming convention of the `pumaburner`. **Anomalies** or **perturbations** of a quantity have the code number of that quantity minus 100. These computations take place in `read_adj_target`. The program recognises the following codes as input for the target pattern of the total energy-weighted projection index (Eq. 4.5), some of which are mutually exclusive ("conflict") since they contain information which is either similar or hard to combine:

- **30** target temperature anomaly ([K])
- **31** target zonal velocity anomaly ([$ms^{-1}$], conflicts with codes **38**, **48**, and **55**)
- **32** target meridional velocity anomaly ([$ms^{-1}$], conflicts with codes **38**, **48**, and **55**)
- **34** target surface pressure anomaly ([Pa], conflicts with codes **51** and **52**)
- **38** target vorticity anomaly ([$s^{-1}$], conflicts with codes **31**, **32**, and **48**)
- **48** target streamfunction anomaly ([$m^2s^{-1}$], conflicts with codes **31**, **32**, and **38**)
- **51** target sea level pressure anomaly ([Pa], in the absence of orography, conflicts with codes **34** and **52**)
- **52** target logarithm-of-surface-pressure anomaly ([log Pa], conflicts with codes **34** and **51**)

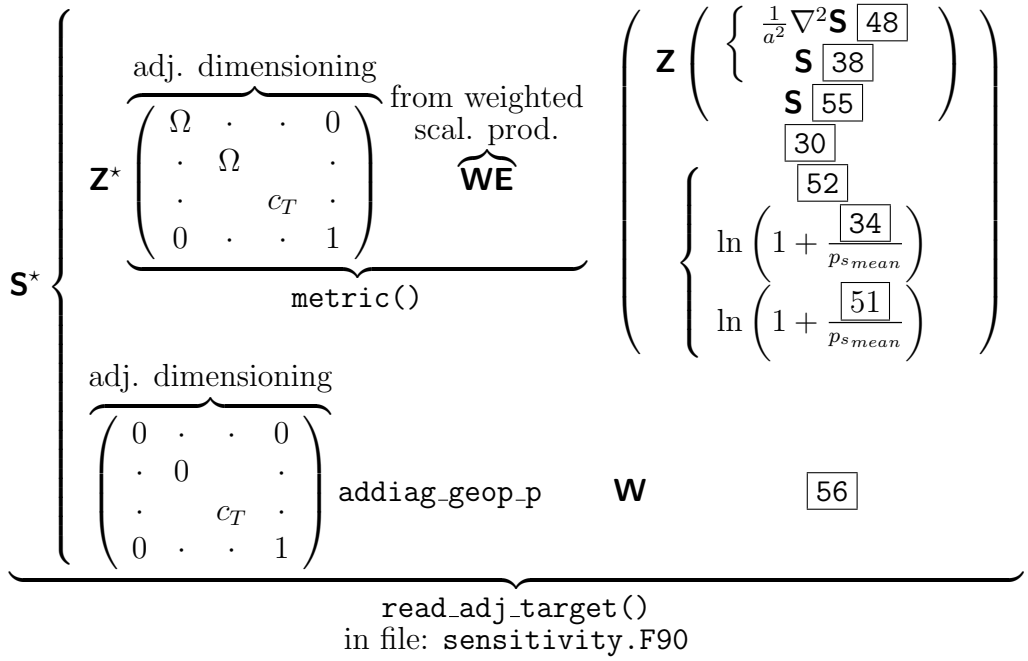


Figure B.1: Schematic overview of the **preprocessing** for the adjoint model run. Information flow is from right to left, describing the formation of a composed input vector $(\delta\zeta, \delta D, \delta T, \delta \ln p_s)^T$ for the adjoint spectral transform from the numbers in boxes, which are codes provided as input to the adjoint in file `TARGET.srv`. **S** (**S**$^\star$) is the (adjoint) spectral transform, **Z** (**Z**$^\star$) is the (adjoint) conversion of divergence and vorticity to velocities, and left braces mark alternative input. The name of the subroutine responsible for a specific step is given either in operator style (`addiag_geop_p`) or annotated with an underbrace (`metric`, `read_adj_target()`), while overbraces are plain remarks.

- **55** target divergence anomaly ([$s^{-1}$], conflicts with codes **31** and **32**)

Alternatively the geopotential height anomaly on one pressure level can be given (code **56** [m]). In this case the header of the `SERVICE`-file must contain the pressure in Pascal. Also the unit of the projection index changes from Joule to square meters in this case (cf. Eq. 4.14). Code **29** [$m^2 s^{-2}$] is also recognised as geopotential anomaly. If the pressure surface on which you provide the geopotential target anomaly does cut through the ground the program issues a warning. The adjoint temperature of the lowest model level will show sensitivity to such a target, since the temperature of the lowest model level would have been used in the extrapolation of such a sub-surface geopotential. The end of a target pattern in `TARGET.srv` is assumed when either the file ends or redundancy in the provided codes is detected.

## B.3 Adjoint integration

The program is set up to efficiently compute repeated adjoint integrations for overlapping pieces of one long reference trajectory. Therefore the `namelist` parameter `nrun` has changed its meaning. The following parameters control the integration:

- `nadvance`: Duration of one adjoint run in time steps.
- `nafter_ad`: Output interval in time steps for files `adoutgp_`$n$`_`$m$`.srv` and `g_ingp_`$n$`_`$m$`.srv`.
- `nrun`: The length of the trajectory to use in time steps. The number of performed integrations will be (`nrun-nadvance`)/`nafter_ad`+1, i.e. just as many as fit onto a trajectory of that length when the starting times are spaced with `nafter_ad`.

For a single integration of the adjoint model over 48 time steps with an output interval of 6 time steps, you must set the following values:

```
nadvance=48,
nafter_ad=6,
nrun=48.
```

For repeated integrations over 360 time steps along a trajectory of 2160 time steps and an output interval of 12 time steps, set:

```
nadvance=360,
nafter_ad=12,
nrun=2160.
```

The following diagram illustrates the described behaviour:

```
|--------------------NADVANCE------------------| run 1.1.
|-NAFTER_AD-|-NAFTER_AD-|-NAFTER_AD-|-NAFTER_AD-| output 1.1.
            |--------------------NADVANCE------------------| run 1.2.
            |-NAFTER_AD-|-NAFTER_AD-|-NAFTER_AD-|-NAFTER_AD-| output 1.2.
                        |--------------------NADVANCE------------------| run 1.3.
                        |-NAFTER_AD-|-NAFTER_AD-|-NAFTER_AD-|-NAFTER_AD-| output 1.3.
                                    |--------------------NADVANCE------------------| run 1.4.
                                    |-NAFTER_AD-|-NAFTER_AD-|-NAFTER_AD-|-NAFTER_AD-| output 1.4.

|-------------------------------------NRUN-----------------------------------------|
                          length of required trajectory
```

## B.4 Adjoint Postprocessing

Postprocessing of adjoint output is the adjoint of the preprocessing of a forward run. It means calculating the derivative with respect to a non-model quantity and requires, in general, the adjoint of the inverse diagnostic operator for that quantity. Such adjoint quantities, as well as the adjoint model variables, are denoted with $()^\star$. Their computation and output is implemented in the routines `adoutgp`, `adwritegp`, and `adwritegpgp`. All fields are transformed to sensitivities in grid-point space and stored in `SERVICE` format. Two output files are available, one giving the sensitivities, the other one giving the optimal perturbations, scaled to yield a unit change in the target function (see Eq. 4.9). As above, the codes mostly are derived from the naming convention of the `pumaburner`. **Sensitivities with respect to a quantity** have the code number of that quantity minus 100. **Sensitivities with respect to forcing** have 5400 added to the regular sensitivity code. The output is selected in the `namelist` via the variable **ncodes_in_adoutgp**. Up to 20 codes can be selected this way in a comma separated list. The output is written to a file named **adoutgp**_$n$_$m$**.srv**, with $n$ being the target time step and $m$ the length of the adjoint integration. This is meaningful for repeated sensitivity calculations for different sections of the same trajectory. Possible choices are (see also Fig. B.2):

- **30** adjoint temperature
- **31** adjoint $u$-wind
- **32** adjoint $v$-wind
- **38** adjoint vorticity
- **48** adjoint streamfunction
- **52** adjoint logarithm of surface pressure
- **55** adjoint divergence
- **60** adjoint potential vorticity (experimental!)
- **5430** adjoint temperature forcing
- **5431** adjoint $u$-wind forcing
- **5432** adjoint $v$-wind forcing
- **5438** adjoint vorticity forcing
- **5452** adjoint logarithm of surface pressure forcing
- **5455** adjoint divergence forcing.

| xx | **1**xx ref. value | xx sensitivity | **54**xx forc. sensitivity |
|---|---|---|---|
| **29** | $\Phi_s$ | - | - |
| **30** | $T$ | $T^\star$ | $f^\star_T$ |
| **31** | $u$ | $u^\star$ | $f^\star_u$ |
| **32** | $v$ | $v^\star$ | $f^\star_v$ |
| **38** | $\zeta$ | $\zeta^\star$ | $f^\star_\zeta$ |
| **48** | $\psi$ | $\psi^\star$ | - |
| **52** | $\ln p_s$ | $(\ln p_s)^\star$ | $f^\star_{(\ln p_s)}$ |
| **54** | $f_T$ [K/s](2) | (use **5430**) | - |
| **55** | $D$ | $D^\star$ | $f^\star_D$ |
| **60** | - | $PV^\star$ (*experim.*) | - |

Figure B.2: Possible choices for the values of the `namelist`-array `ncodes_in_adoutgp`.

The **optimal perturbations** are written to a file named `g_ingp`$\_n\_m$. Two additional quantities are available. They represent the initial energy distribution of the cost function response to the optimal perturbation (**4000**) and to the optimal forcing perturbation (**9400**). This concept stems from Eq. (6) of Langland *et al.* (2002). These quantities are useful to view all sensitivities at once, bundled into one quantity which has the unit of energy. Area weights are removed from the output of codes **40xx** and **94xx** in order to facilitate plotting. The selection is done via the `namelist` parameter `ncodes_in_g_ingp` in a comma separated list of up to 20 entries. Possible values are (see also Fig. B.3):

- **30** optimal temperature perturbation
- **31** optimal $u$-wind perturbation
- **32** optimal $v$-wind perturbation
- **52** optimal logarithm of surface pressure perturbation
- **4000** vertically integrated energy of optimal perturbation
- **4030** $u$-wind contribution to **4000**
- **4031** $v$-wind contribution to **4000**
- **4032** temperature contribution to **4000**
- **4052** $\ln p_s$ contribution to **4000**

[2]Caution! This code is often also used for the relaxation temperature with unit [K].

- **5430** optimal temperature forcing perturbation
- **5431** optimal $u$-wind forcing perturbation
- **5432** optimal $v$-wind forcing perturbation
- **5452** optimal logarithm of surface pressure forcing perturbation
- **9400** vertically integrated energy of optimal forcing perturbation
- **9430** temperature contribution to **9400**
- **9431** $u$-wind contribution to **9400**
- **9432** $v$-wind contribution to **9400**
- **9452** $\ln p_s$ contribution to **9400**

## B.5 Computational details

To illustrate the meaning of the postprocessing of the adjoint it may be helpful to derive it from the preprocessing of a tangent-linear forward run. The following is a detailed example for the case of sensitivity to streamfunction. The tangent-linear mapping of a streamfunction perturbation $\delta\psi(t_1)$ to streamfunction $\delta\psi(t_2)$ at a later time may be written as

$$\delta\psi(t_2) = \mathbf{model}_{tl}(\delta\psi(t_1)). \tag{B.1}$$

Since the tangent linear `PUMA` does not operate on grid point streamfunction the operator $\mathbf{model}_{tl}$ implicitly contains transformation from grid point- to spectral space ($\texttt{fc2sp} \circ \texttt{gp2fc}$)[3], de-dimensioning ($\frac{1}{\Omega R^2}$), the inverse Laplaceian operator ($\nabla^{-2}$), and the inverse operation of all the aforementioned. In order to avoid possible problems with the different time levels of the leap-frog-scheme used in `PUMA`, the perturbation is applied to both time levels and a few Euler steps (set by `nkits`) are carried out prior to the regular integration. Therefore $\mathbf{model}_{tl}$ from (B.1) can be rewritten as:

$$\begin{aligned}\mathbf{model}_{tl} \;=\; & \overbrace{\texttt{fc2gp} \circ \texttt{sp2fc} \circ \Omega R^2 \nabla^{-2}}^{\text{postprocessing}} \circ \\ & \texttt{PUMA}_{tl} \circ \\ & \underbrace{\texttt{Euler} - \texttt{steps}_{tl} \circ \begin{pmatrix} \mathbf{1} \\ \mathbf{1} \end{pmatrix} \circ \texttt{fs2sp} \circ \texttt{gp2fc} \circ \frac{1}{\Omega R^2} \nabla^2}_{\text{preprocessing}}\end{aligned}$$

[3]read as: f(ourier) c(oefficients)-to-sp(ectral) and g(rid)p(oint)-to-f(ourier) c(oefficients)

| | **1**xx | xx | **40**xx | **54**xx | **94**xx |
|---|---|---|---|---|---|
| xx | ref. value | opt. pert. | sens. energy | opt. forc. | forc. energy |
| **00** | - | - | $\mathbf{W}^{-1}\lambda\sum_{j,k}(\Psi^\star_{i,j,k}\,\mathbf{C}_k^{-1}\Psi^\star_{i,j,k})$ | - | $\mathbf{W}^{-1}\lambda\sum_{j,k}(f^\star_{\Psi_{i,j,k}}\,\mathbf{C}_k^{-1}f^\star_{\Psi_{i,j,k}})$ |
| **30** | $T$ | $\lambda\mathbf{C}^{-1}T^\star$ | $\mathbf{W}^{-1}\lambda T_i^\star\mathbf{C}_T^{-1}T_i^\star$ | $\lambda\mathbf{C}^{-1}f_T^\star$ | $\mathbf{W}^{-1}\lambda f_{T_i}^\star\mathbf{C}_T^{-1}f_{T_i}^\star$ |
| **31** | $u$ | $\lambda\mathbf{C}^{-1}u^\star$ | $\mathbf{W}^{-1}\lambda u_i^\star\mathbf{C}_u^{-1}u_i^\star$ | $\lambda\mathbf{C}^{-1}f_u^\star$ | $\mathbf{W}^{-1}\lambda f_{u_i}^\star\mathbf{C}_u^{-1}f_{u_i}^\star$ |
| **32** | $v$ | $\lambda\mathbf{C}^{-1}v^\star$ | $\mathbf{W}^{-1}\lambda v_i^\star\mathbf{C}_v^{-1}v_i^\star$ | $\lambda\mathbf{C}^{-1}f_v^\star$ | $\mathbf{W}^{-1}\lambda f_{v_i}^\star\mathbf{C}_v^{-1}f_{v_i}^\star$ |
| **38** | $\zeta$ | $\lambda\mathbf{C}^{-1}\zeta^\star$ | - | $\lambda\mathbf{C}^{-1}f_\zeta^\star$ | - |
| **52** | $\ln p_s$ | $\lambda\mathbf{C}^{-1}(\ln p_s)^\star$ | $\mathbf{W}^{-1}\lambda(\ln p_s)_i^\star\,\mathbf{C}^{-1}_{(\ln p_s)}(\ln p_s)_i^\star$ | $\lambda\mathbf{C}^{-1}f^\star_{(\ln p_s)}$ | $\mathbf{W}^{-1}\lambda f^\star_{(\ln p_s)_i}\,\mathbf{C}^{-1}_{(\ln p_s)}f^\star_{(\ln p_s)_i}$ |
| **55** | $D$ | $D^\star$ | - | $\lambda\mathbf{C}^{-1}f_D^\star$ | - |

Figure B.3: Possible choices for the values of the `namelist`-array `ncodes_in_g_ingp`. Index $i$ stands for grid points, summation $j$ is over model levels, and $k$ goes over variables $u$, $v$, $T$, and $(\ln p_s)$. $\mathbf{W}^{-1}$ is inverse area weighting to allow plotting of the energy contributions, $\mathbf{C}$ equals $\mathbf{WE}$ as defined in Eq. (4.6), and $\lambda$ is defined in Eq. (4.9).

The matrix $\begin{pmatrix}\mathbf{1}\\ \mathbf{1}\end{pmatrix}$ represents the perturbation of both time levels at once. $\mathbf{1}$ is the identity matrix with the rank of the number of spectral coefficients in `PUMA`. For the adjoint Operator $\mathbf{model}_{adj} = (\mathbf{model}_{tl})^*$ follows:

$$\mathbf{model}_{adj} = \overbrace{\underbrace{\nabla^{-2}\circ \texttt{adsp2fc}\circ\texttt{adfc2gp}\circ\Omega R^2}_{\text{adj. preprocessing}}\circ\ \texttt{PUMA}_{\texttt{adj}}\circ\ \texttt{adgp2fc}\circ\texttt{adfc2sp}\circ\frac{1}{\Omega R^2}\circ\nabla^2\circ\begin{pmatrix}\mathbf{1} & \mathbf{1}\end{pmatrix}\circ\texttt{Euler}-\texttt{steps}_{adj}\circ}^{\text{adj. postprocessing}}$$

*Adjoint Preprocessing:* Note that in Eq. (B.2) as well as in the actual implementation the order of the adjoint spectral to grid point transform and the adjoint dimensioning is reversed. This has only technical reasons and does not change the operation since the transform is linear and unaffected by other quantities. The adjoint transform into grid point space corresponds to the forward transform from grid point to spectral space, since this is one of the special cases where the inverse operation is also the adjoint. In `PUMA` it is split up into two steps, *transformation from grid point space to Fourier coefficients along the latitudes* (`gp2fc`) and the *transformation from Fourier to spectral space* (`fc2sp`) by projection onto spherical harmonics. This is one of the few cases where the inverse operation is also the adjoint. Due to a different scaling of forward and

backward transform, an interface routine `adsp2fc`[4] is called, which calls `fc2sp` in turn and adjusts the scaling.
The Laplaceian $\nabla^2$ in spectral space takes the form of a diagonal matrix and therefore is self-adjoint. The same is true for the inverse Laplaceian $\nabla^{-2}$ and its adjoint $\nabla^{-2^*}$.

*Adjoint Postprocessing:* Before outputting the adjoint variables have to be transformed back into grid point space. This is done in the subroutines `adfc2sp`[5] and `adgp2fc`[6]. As above, `adfc2sp` is an interface to `sp2fc`. On top of that the adjoint variables undergo adjoint de-dimensioning. This is self-adjoint and corresponds to de-dimensioning in the forward model.

[4]read as: ad(joint) sp(ectral)-to-f(ourier) c(oefficients)
[5]read as: ad(joint) f(ourier) c(oefficients)-to-sp(ectral)
[6]read as: ad(joint) f(ourier) c(oefficients)-to-sp(ectral)

# Bibliography


Arbogast, P., 1998: Sensitivity to potential vorticity. *Quart. J. Roy. Meteor. Soc.*, **124 (549)**, 1605 – 1615.

Bader, J. and M. Latif, 2003: The impact of decadal-scale Indian Ocean sea surface temperature anomalies on Sahelian rainfall and the North Atlantic Oscillation. *Geophys. Res. Lett.*, **30 (22)**, 2169–2172.

Bagliani, M., K. Fraedrich, J. von Hardenberg, F. Lunkeit, and A. Provencale, 2000: Lagrangian tracer homogenization and dispersion in a simplified atmospheric GCM. *Il Nuovo Cimento*, **23C**, 433–448.

Baldwin, M. P. and T. J. Dunkerton, 1999: Propagation of the Arctic Oscillation from the stratosphere to the troposphere. *J. Geophys. Res.*, **104**, 30 937–30 946.

Barkmeijer, J., T. Iversen, and T. N. Palmer, 2003: Forcing singular vectors and other sensitive model structures. *Quart. J. Roy. Meteor. Soc.*, **129**, 2401–2423, doi:10.1256/qj.02.210.

Blessing, S., 2000: Entwicklung und Anwendungen eines adjungierten globalen Zirkulationsmodells. Diplomarbeit, Meteorologisches Institut, Universität Hamburg.

Blessing, S., K. Fraedrich, M. M. Junge, T. Kunz, and F. Lunkeit, 2005: Daily North-Atlantic Oscillation (NAO) index: Statistics and its stratospheric polar vortex dependence. *Meteor. Z.*, **14 (6)**, 763–769.

Blessing, S., K. Fraedrich, and F. Lunkeit, 2004: Climate diagnostics by adjoint modelling: A feasibility study. *The KIHZ project: Towards a synthesis of Holocene Proxy Data and Climate Models*, Fischer, H., T. Kumke, G. Lohmann, G. Flöser, H. Miller, H. von Storch, and J. F. W. Negendank, Eds., Springer, Berlin Heidelberg New York, 383–396, URL `http://www.mi.uni-hamburg.de/fileadmin/files/forschung/theomet/docs/pdf/blefraelun04.pdf`.

Blessing, S., R. Greatbatch, K. Fraedrich, and F. Lunkeit, 2008: Interpreting the atmospheric circulation trend during the last half of the 20th century: Application of an adjoint model. *J. Climate*, doi:10.1175/2008JCLI1990.1, accepted.

Boenisch, G., S. Harrison, I. Prentice, and Biome 6000 members, 2001: *BIOME 6000 Data Release 1.* Data Contribution Series No 2001-046, IGBP PAGES/World Data Center for Paleoclimatology, NOAA/NGDC Paleoclimatology Program, Boulder, Boulder CO, USA.

Bordi, I., K. Fraedrich, F. Lunkeit, and A. Sutera, 2007: Tropospheric double jets, meridional cells, and eddies: A case study and idealized simulations. *Mon. Wea. Rev.*, **135 (9)**, 3118 – 3133.

Branstator, G., 1985: Analysis of general circulation model sea-surface temperature anomaly simulations using a linear model. Part i: Forced solutions. *J. Atmos. Sci.*, **42 (21)**, 2225–2241.

Bücker, H. M., G. F. Corliss, P. Hovland, U. Naumann, and B. Norris, (Eds.) , 2005: *Automatic Differentiation: Applications, Theory, and Implementations*, Lecture Notes in Computational Science and Engineering, Vol. 50. Springer, New York, NY, 367 pp.

Buizza, R., J. Tribbia, F. Molteni, and T. Palmer, 1993: Computation of optimal unstable structures for a numerical weather prediction model. *Tellus*, **45A**, 388–407.

Cacuci, D. G., 1981a: Sensitivity theory for nonlinear systems. i: Nonlinear functional analysis of responses. *J. Math. Phys.*, **22**, 2794–2802.

———, 1981b: Sensitivity theory for nonlinear systems. ii: Extension to additional classes of responses. *J. Math. Phys.*, **22**, 2803–2812.

Charlton, A. J., A. O'Neill, W. A. Lahoz, and A. C. Massacand, 2004: Sensitivity of tropospheric forecasts to stratospheric initial conditions. *Quart. J. Roy. Meteor. Soc.*, **130**, 1771–1792.

Corti, S., F. Molteni, and T. N. Palmer, 1999: Signature of recent climate change in frequencies of natural atmospheric circulation regimes. *Nature*, **398 (6730)**, 799 – 802.

Corti, S. and T. N. Palmer, 1997: Sensitivity analysis of atmospheric low-frequency variability. *Quart. J. Roy. Meteor. Soc.*, **123 (544)**, 2425 – 2447.

Courtier, P., J.-N. Thépaut, and A. Hollingsworth, 1994: A strategy for operational implementation of 4-D-VAR using an incremental approach. *Quart. J. Roy. Meteor. Soc.*, **120**, 1367–1387.

Cubasch, U., G. Meehl, G. Boer, R. Stouffer, M. Dix, A. Noda, C. Senior, S. Raper, and K. Yap, 2001: Projections of future climate change. *Climate Change 2001: The Scientific basis*, Houghton, J. T., Y. Ding, D. J. Griggs,

M. Noguer, P. J. van der Linden, X. Dai, K. Maskell, and C. A. Johnson, Eds., Cambridge University Press, Cambridge, U.K., chap. 9, 525–582.

Deser, C., A. S. Phillips, and J. W. Hurrell, 2004: Pacific interdecadal climate variability: Linkages between the tropics and the North Pacific during boreal winter since 1900. *J. Climate*, **17**, 3109–3124.

Errico, R. M., 2000: Interpretations of the total energy and rotational energy norms applied to determination of singular vectors. *Quart. J. Roy. Meteor. Soc.*, **126**, 1581–1599.

Eyink, G. L., T. W. N. Haine, and D. J. Lea, 2004: Ruelle's linear response formula, ensemble adjoint schemes and Lévy flights. *Nonlinearity*, **17**, 1867–1889, doi:10.1088/0951-7715/17/5/016.

Feldstein, S., 2002: The recent trend and variance increase of the annular mode. *J. Climate*, **15 (1)**, 88 – 94.

Fletcher, R. and M. Powell, 1963: A rapidly convergent descent method for minimization. *Computer Journal*, **6 (2)**, 163–168.

Fraedrich, K., S. Blessing, E. Kirk, T. Kunz, U. Luksch, F. Lunkeit, and F. Sielmann, 2007: *PUMA User's Guide*. Universität Hamburg, Meteorologisches Institut, URL `http://www.mi.uni-hamburg.de/fileadmin/files/forschung/theomet/planet_simulator/downloads/PUMA_UsersGuide.pdf`.

Fraedrich, K., H. Jansen, E. Kirk, U. Luksch, and F. Lunkeit, 2005a: The planet simulator: Towards a user friendly model. *Meteor. Z.*, **14 (3)**, 299 – 304.

Fraedrich, K., H. Jansen, E. Kirk, and F. Lunkeit, 2005b: The planet simulator: Green planet and desert world. *Meteor. Z.*, **14 (3)**, 305 – 314.

Fraedrich, K., E. Kirk, U. Luksch, and F. Lunkeit, 2005c: The Portable University Model of the Atmosphere (PUMA): Storm track dynamics and low-frequency variability. *Meteor. Z.*, **14 (6)**, 735–745, URL `http://www.mi.uni-hamburg.de/PUMA.215.0.html`.

Fraedrich, K., E. Kirk, and F. Lunkeit, 1998: Portable University Model of the Atmosphere. Tech. Rep. **16**, DKRZ.

Franzke, C., K. Fraedrich, and F. Lunkeit, 2000: Low frequency variability in a simplified atmospheric global circulation model: Storm track induced 'spatial resonance'. *Quart. J. Roy. Meteor. Soc.*, **126**, 2691–2708.

———, 2001: Teleconnections and low-frequency variability in idealized experiments with two storm tracks. *Quart. J. Roy. Meteor. Soc.*, **127 (574)**, 1321 – 1339.

Frederiksen, J. S., 2000: Singular vectors, finite-time normal modes, and error growth during blocking. *J. Atmos. Sci.*, **57 (2)**, 312 – 333.

Frisius, T., F. Lunkeit, K. Fraedrich, and I. N. James, 1998: Storm-track organization and variability in a simplified atmospheric global circulation model. *Quart. J. Roy. Meteor. Soc.*, **124 (548)**, 1019 – 1043.

Galanti, E., E. Tziperman, M. Harrison, A. Rosati, R. Giering, and Z. Sirkes, 2002: The equatorial thermocline outcropping - a seasonal control on the tropical pacific ocean-atmosphere instability. *J. Climate*, **15 (19)**, 2721–2739, doi: 10.1175/1520-0442(2002)015⟨2721:TETOAS⟩2.0.CO;2.

Giering, R. and T. Kaminski, 1998: Recipes for adjoint code construction. *ACM Trans. on Math. Software*, **24 (4)**, 437–474, doi:10.1145/293686.293695.

Giering, R., T. Kaminski, M. Scholze, P. Rayner, W. Knorr, H. Widmann, R. Todling, and S.-J. Lin, 2003: An overview on adjoint applications in earth system modelling. Presentation at International Conference on Earth System Modelling, Hamburg, URL `http://www.FastOpt.com/papers/gieringal03-hh-final.pdf`.

Giering, R., T. Kaminski, R. Todling, R. Errico, R. Gelaro, and N. Winslow, 2005: Generating tangent linear and adjoint versions of NASA/GMAO's Fortran-90 global weather forecast model. Bücker et al. (2005), 273–282.

Gillett, N. P., H. F. Graf, and T. J. Osborn, 2003: Climate change and the North Atlantic Oscillation. *The North Atlantic Oscillation: Climate Significance and Environmental Impact*, Hurrell, J., Y. Kushnir, G. Ottersen, and M. Visbeck, Eds., Amer. Geophys. Union, Washington, DC, USA, Geophysical Monograph Series, Vol. 134, chap. 9, 193–209.

Gillett, N. P. and D. W. J. Thompson, 2003: Simulation of recent Southern Hemisphere climate change. *Science*, **302**, 273–275.

Golub, G. H. and C. E. van Loan, 1983: *Matrix Computations*. North Oxford Academic Publ. Co. Ltd., xiv+476 pp.

Greatbatch, R. J., 2000: The North Atlantic Oscillation. *Stoch. Environ. Res. Risk Assess.*, **14 (4-5)**, 213 – 242.

Greatbatch, R. J. and T. Jung, 2007: Local versus tropical diabatic heating and the winter North Atlantic Oscillation. *J. Climate*, **20 (10)**, 2058–2075, doi:10.1175/jcli4125.1.

Grieger, B., J. Segschneider, H. U. Keller, A. Rodin, F. Lunkeit, E. Kirk, and K. Fraedrich, 2004: Simulating Titan's tropospheric circulation with the

Portable University Model of the Atmosphere. *Advances in Space Res.*, **34**, 1650–1654.

Gritsun, A. and G. Branstator, 2007: Climate response using a three-dimensionl operator based on the fluctuation dissipation theorem. *J. Atmos. Sci.*, **64**, 2558–2575.

Hall, N. M. J., 2000: A simple GCM based on dry dynamics and constant forcing. *J. Atmos. Sci.*, **57**, 1557–1572.

Heimbach, P., C. Hill, and R. Giering, 2002: Automatic generation of efficient adjoint code for a parallel Navier-Stokes solver. *Computational Science – ICCS 2002, Proceedings of the International Conference on Computational Science, Amsterdam, The Netherlands, April 21–24, 2002. Part II*, Sloot, P. M. A., C. J. K. Tan, J. J. Dongarra, and A. G. Hoekstra, Eds., Springer, Berlin, Lecture Notes in Computer Science, Vol. 2330, 1019–1028.

———, 2005: An efficient exact adjoint of the parallel MIT general circulation model, generated via automatic differentiation. *Future Generation Computer Systems*, **21 (8)**, 1356–1371, URL `http://dx.doi.org/10.1016/j.future.2004.11.010`.

Held, I. M. and M. J. Suarez, 1994: A proposal for the intercomparison of the dynamical cores of atmospheric general circulation models. *Bull. Amer. Meteor. Soc.*, **75 (10)**, 1825–1830.

Hoerling, M. P., J. W. Hurrell, T. Xu, G. T. Bates, and A. S. Philips, 2004: Twentieth century North Atlantic climate change. Part II: Understanding the effect of Indian Ocean warming. *Clim. Dyn.*, **23 (3-4)**, 391–405.

Hoerling, M. P., J. W. Hurrell, and T. Y. Xu, 2001: Tropical origins for recent North Atlantic climate change. *Science*, **292**, 90–92.

Hoskins, B. J. and D. J. Karoly, 1981: The steady linear response of a spherical atmosphere to thermal and orographic forcing. *J. Atmos. Sci.*, **38 (6)**, 1179–1196.

Hoskins, B. J. and A. J. Simmons, 1975: A multi-layer spectral model and the semi-implicit method. *Quart. J. Roy. Meteor. Soc.*, **101**, 637–655.

Hoteit, I., B. Cornuelle, A. Köhl, and D. Stammer, 2005: Treating strong adjoint sensitivities in tropical eddy-permitting variational data assimilation. *Quart. J. Roy. Meteor. Soc.*, **131 (613)**, 3659–3682.

Hurrell, J., Y. Kushnir, M. Visbeck, and G. Ottersen, 2003: An overview of the North Atlantic Oscillation. *The North Atlantic Oscillation: Climate Significance and Environmental Impact*, Hurrell, J., Y. Kushnir, G. Ottersen, and

M. Visbeck, Eds., Amer. Geophys. Union, Washington, DC, USA, Geophysical Monograph Series, Vol. 134, chap. 1, 1–35.

Hurrell, J. W., 1996: Influence of variations in extratropical wintertime teleconnections on Northern Hemisphere temperature. *Geophys. Res. Lett.*, **23**, 665–668.

Hurrell, J. W., M. P. Hoerling, A. S. Phillips, and T. Xu, 2004: Twentieth century North Atlantic climate change. Part I: Assessing determinism. *Clim. Dyn.*, **23 (3-4)**, 371–389.

Iversen, T., J. Kristiansen, T. Jung, and J. Barkmeijer, 2008: Optimal atmospheric forcing perturbations for the Cold Ocean Warm Land pattern. *Tellus*, **60 (3)**, 528–546, doi:10.1111/j.1600-0870.2008.00310.x.

Jones, C., J. Gregory, R. Thorpe, P. Cox, J. Murphy, D. Sexton, and P. Valdes, 2005: Systematic optimisation and climate simulation of FAMOUS, a fast version of HadCM3. *Climate Dynamics*, **25 (2)**, 189–204.

Jung, T. and J. Barkmeijer, 2006: Sensitivity of the tropospheric circulation to changes in the strength of the stratospheric polar vortex. *Mon. Wea. Rev.*, **134**, 2191–2207.

Junge, M. M. and K. Fraedrich, 2007: Temperature anomalies in the northeastern North Atlantic: Subpolar and subtropical precursors on multiannual time scales. *J. Climate*, **20**, 1976–1990.

Junge, M. M. and T. Haine, 2001: Mechanisms of North Atlantic wintertime Sea Surface Temperature Anomalies. *J. Climate*, **14**, 4560–4572.

Kalnay, E., 2003: *Atmospheric Modelling, Data Assimilation and Predictability.* Cambridge University Press, xxii+341 pp., doi:10.1256/00359000360683511.

Kaminski, T., S. Blessing, R. Giering, M. Scholze, and M. Voßbeck, 2007: Testing the use of adjoints for estimation of GCM parameters on climate time-scales. *Meteor. Z.*, **16 (6)**, 643–652, doi:10.1127/0941-2948/2007/0259.

Kleidon, A., K. Fraedrich, E. Kirk, and F. Lunkeit, 2006: Maximum entropy production and the strength of boundary layer exchange in an atmospheric general circulation model. *Geophys. Res. Lett.*, **33 (6)**, 1627 – 1643.

Kleidon, A., K. Fraedrich, T. Kunz, and F. Lunkeit, 2003: The atmospheric circulation and states of maximum entropy production. *Geophys. Res. Lett.*, **30 (23)**, 2223(4 p.), doi:10.1029/2003GL0183632.

Kleist, D. T. and M. Morgan, 2005: Interpretation of the structure and evolution of adjoint-derived forecast sensitivity gradients. *Mon. Wea. Rev.*, **133**, 466–484.

Köhl, A. and J. Willebrand, 2002: An adjoint method for the assimilation of statistical characteristics into eddy-resolving ocean models. *Tellus*, **54A**, 406–425.

Kucharski, F., F. Molteni, and A. Bracco, 2006: Decadal interactions between the western tropical Pacific and the North Atlantic Oscillation. *Clim. Dyn.*, **26**, 79–91, doi:10.1007/s00382-005-0085-5.

Kunz, T., 2003: Eine Bewertungsfunktion zur Parameteroptimierung in globalen atmosphärischen Zirkulationsmodellen. Diplomarbeit, Meteorologisches Institut, Universität Hamburg.

Kunz, T., K. Fraedrich, and E. Kirk, 2008a: Optimisation of simplified GCMs using circulation indices and maximum entropy production. *Clim. Dyn.*, **30 (7-8)**, 803–813, doi:10.1007/s00382-007-0325-y, URL `http://www.mi.uni-hamburg.de/fileadmin/files/forschung/theomet/docs/pdf/2007-kunzfraekirk.pdf`.

Kunz, T., L. Fraedrich, and F. Lunkeit, 2008b: Synoptic scale wave breaking in an SGCM and its potential to drive NAO-like circulation dipoles. *J. Atmos. Sci.*, submitted.

Langland, R., M. A. Shapiro, and R. Gelaro, 2002: Initial condition sensitivity and error growth in forecasts of the 25 January 2000 east coast snowstorm. *Mon. Wea. Rev.*, **130**, 957–974.

Lea, D. J., M. R. Allen, and T. W. N. Haine, 2000: Sensitivity analysis of the climate of a chaotic system. *Tellus*, **52A**, 523 – 532.

Lea, D. J., T. W. N. Haine, and J. A. Hansen, 2002: Sensitivity analysis of the climate of a chaotic ocean circulation model. *Quart. J. Roy. Meteor. Soc.*, **128**, 2587–2605, doi:10.1256/qj.01.180.

Lee, T., J.-P. Boulanger, A. Foo, L.-L. Fu, and R. Giering, 2000: Data assimilation into an intermediate coupled ocean-atmosphere model: application to the 1997-98 El Nino. *J. Geophys. Res.*, **105 (C11)**, 26,063–26,088.

Liakka, J., 2006: Validation of the dynamical core of the Portable University Model of the Atmosphere (PUMA). Master's thesis, Inst. of Meteor. and Geophys., U. of Innsbruck and Uppsala Universitet, URL `http://www.mi.uni-hamburg.de/fileadmin/files/forschung/theomet/planet_simulator/downloads/Johan_Liakka.pdf`, iSSN 1650-6553 Nr. 130.

Lions, J.-L., 1971: *Optimal Control of Systems Governed by Partial Differential Equations*. Springer Verlag, Berlin, 396 pp., original title: Contrôle optimale de systèmes gouvernés par des équations aux dérivés partielles.

Lohmann, G., M. Butzin, K. Grosfeld, G. Knorr, A. Paul, M. Prange, V. Romanova, , and S. Schubert, 2003: Bremen Earth System Model of Intermediate Complexity (BREMIC) designed for long-term climate studies. Model description, climatology, and applications. Technical report, The University of Bremen, Germany.

Lorenc, A. C., 2006: 4D-Var and the Butterfly Effect. Statistical 4D-Var for a wide range of scales. Tech. Rep. FRTR481, Meteorological Office, Bracknell, UK.

Lorenz, E. N., 1963: Deterministic nonperiodic flow. *J. Atmos. Sci.*, **20**, 130–141.

———, 1965: A study of the predicability of a 28-variable atmospheric model. *Tellus*, **XVII**, 321–333.

Lu, J., R. J. Greatbatch, and K. A. Peterson, 2004: Trend in Northern Hemisphere winter atmospheric circulation during the last half of the twentieth century. *J. Climate*, **17**, 3745–3760.

Lunkeit, F., 2001: Synchronization experiments with an atmospheric global circulation model. *Chaos*, **11 (1)**, 47–51.

Lunkeit, F., K. Fraedrich, and S. E. Bauer, 1998: Strom tracks in a warmer climate: Sensitivity studies with a simplified global circulation model. *Climate Dynamics*, Springer-Verlag, Vol. 14, 813–826.

Marchuk, G. I., 1974: *Numerical Solution of Problems in Atmospheric and Oceanic Dynamics*. Gidrometeoizdat, Leningrad, 304 pp., (in Russian).

Marotzke, J., R. Giering, Q. K. Zhang, D. Stammer, C. N. Hill, and T. Lee, 1999: Construction of the adjoint MIT ocean general circulation model and application to Atlantic heat transport sensitivity. *J. Geophys. Res.*, **104**, 29,529 – 29,548, URL `http://www.agu.org/journals/jc/jc9912/jc104_12.html`.

Marshall, J. and F. Molteni, 1993: Toward a dynamical understanding of planetary-scale flow regimes. *J. Atmos. Sci.*, **50 (12)**, 1792–1818.

McLay, F. and J. Marotzke, 2008: Limitation to the use of adjoint methods with eddy-resolving ocean general circulation models. *Ocean Modelling*, submitted.

Montani, A. and A. J. Thorpe, 2002: Mechanisms leading to singular-vector growth for FASTEX cyclones. *Quart. J. Roy. Meteor. Soc.*, **128 (579)**, 131 – 148.

Müller, W., R. Blender, and K. Fraedrich, 2002: Low frequency variability in idealised GCM experiments with circumpolar and localised storm tracks. *Nonlinear Processes Geophys.*, **9**, 37–49.

Murphy, J. M., D. M. H. Sexton, D. N. Barnett, G. S. Jones, M. J. Webb, M. Collins, and D. A. Stainforth, 2004: Quantification of modelling uncertainties in a large ensemble of climate change simulations. *Nature*, **430**, 768–772.

Nehrkorn, T., G. D. Modica, M. Cemiglia, F. H. Ruggiero, J. G. Michalakes, and X. Zou, 2002: 4DVAR Development Using an Automatic Code Generator: Application to MM5v3. *Proceedings of Twelfth PSU/NCAR Mesoscale Model Users' Workshop*, National Center for Atmospheric Research, Boulder, California, USA, URL `http://www.mmm.ucar.edu/mm5/mm5-home.html`.

Penenko, V. V. and N. N. Obraztsov, 1976: A variational initialization method for the fields of the meteorological elements. *Meteorol. Gidrol. (Soviet Meteorol. Hydrol.)*, **11**, 1–11, (Englische übersetzung).

Penland, C., 1989: Random forcing and forecasting using principal oscillation pattern analysis. *Mon. Wea. Rev.*, **117**, 2165–2185.

Perez-Munuzuri, V., M. Lorenzo, P. Montero, K. Fraedrich, E. Kirk, and F. Lunkeit, 2003: Response of a global atmospheric circulation model to spatio-temporal stochastic forcing: ensemble statistics. *Nonlin. Proc. in Geophys.*, **10 (6)**, 453 – 461.

Pires, C., R. Vautard, and O. Talagrand, 1996: On extending the limits of variational assimilation in nonlinear chaotic systems. *Tellus*, **48A**, 96–121, doi: 10.1034/j.1600-0870.1996.00006.x.

Polvani, L. M. and P. J. Kushner, 2002: Tropospheric response to stratospheric perturbations in a relatively simple general circulation model. *Geophys. Res. Lett.*, **29**, doi:10.1029/2001GL014284.

Prentice, I. C., G. D. Farquhar, M. J. R. Fasham, M. L. Goulden, M. Heimann, V. J. Jaramillo, H. S. Kheshgi, C. Le Quéré, R. J. Scholes, and D. W. R. Wallace, 2001: The carbon cycle and atmospheric carbon dioxide. *Climate Change 2001: The Scientific basis*, Houghton, J. T., Y. Ding, D. J. Griggs, M. Noguer, P. J. van der Linden, X. Dai, K. Maskell, and C. A. Johnson, Eds., Cambridge University Press, Cambridge, U.K., chap. 3, 183–237.

Rayleigh, Lord, 1916: On convective currents in a horizontal layer of fluid when the higher temperature is on the under side. *Phil. Mag.*, **32**, 529–546.

Rayner, P., M. Scholze, W. Knorr, T. Kaminski, R. Giering, and H. Widmann, 2005: Two decades of terrestrial Carbon fluxes from a Carbon Cycle Data Assimilation System (CCDAS). *Global Biogeochemical Cycles*, **19**, doi:10.1029/2004GB002 254.

Romero, R., A. Martín, V. Homar, S. Alonso, and C. Ramis, 2005: Predictability of prototype flash flood events in the Western Mediterranean under uncertainties of the precursor upper-level disturbance: the HYDROPTIMET case studies. *Natural Hazards and Earth System Sciences*, **5**, 505–525, sRef-ID: 1684-9981/nhess/2005-5-505.

Sardeshmukh, P. and B. J. Hoskins, 1988: The generation of global rotational flow by steady, idealised tropical divergence. *J. Atmos. Sci.*, **45**, 1228–1251.

Sardeshmukh, P. and P. Sura, 2007: Multiscale impacts of variable heating in climate. *J. Climate*, **20 (23)**, 5677 – 5695.

Scaife, A. A., J. R. Knight, G. K. Vallis, and C. K. Folland, 2005: A stratospheric influence on the winter NAO and North Atlantic surface climate. *Geophys. Res. Lett.*, **32 (18)**, L18 715, doi:10.1029/2005GL023226.

Scholze, M., 2003: Model studies on the response of the terrestrial carbon cycle on climate change and variability. Examensarbeit, Max-Planck-Institut für Meteorologie, Hamburg, Germany, URL `http://www.mpimet.mpg.de/fileadmin/publikationen/Ex90.pdf`.

Scholze, M., T. Kaminski, P. Rayner, W. Knorr, and R. Giering, 2007: Propagating uncertainty through prognostic carbon cycle data assimilation system simulations. *J. Geophys. Res.*, **112**, D17 305, doi:10.1029/2007JD008642.

Segschneider, J., B. Grieger, H. Keller, F. Lunkeit, E. Kirk, K. Fraedrich, A. Rodin, and R. Greve, 2005: Response of the intermediate complexity mars climate simulator to different obliquity angles. *Planetary and Space Science*, **53 (6)**, 659 – 670.

Seiffert, R., R. Blender, and K. Fraedrich, 2006: Subscale forcing in a global atmospheric circulation model and stochastic parametrization. *Quart. J. Roy. Meteor. Soc.*, **132 (618)**, 1627 – 1643.

Simmons, A. J. and D. M. Burridge, 1981: An energy and angular-momentum conserving vertical finite-difference scheme and hybrid vertical coordinates. *Mon. Wea. Rev.*, **109**, 758–766.

Sirkes, Z. and E. Tziperman, 1997: Finite difference of adjoint or adjoint of finite difference? *Mon. Wea. Rev.*, **125 (12)**, 3373–3378.

Stainforth, D. A., T. Aina, C. Christensen, M. Collins, N. Faull, D. J. Frame, J. A. Kettleborough, S. Knight, A. Martin, J. M. Murphy, C. Piani, D. Sexton, R. A. S. L. A. Smith and, A. J. Thorpe, and M. R. Allen, 2005: Uncertainty in predictions of the climate response to rising levels of greenhouse gases. *Nature*, **433**, 403–406.

Stammer, D., C. Wunsch, R. Giering, C. Eckert, P. Heimbach, J. Marotzke, A. Adcroft, C. N. Hill, and J. Marshall, 2002: The global ocean circulation during 1992-1997, estimated from ocean observations and a general circulation model. *J. Geophys. Res.*, **107 (C9)**, doi:10.1029/2001JC000 888, URL `http://www.ecco-group.org/publications.html`.

Szunyogh, I., E. Kalnay, and Z. Toth, 1997: A comparison of lyapunov and optimal vectors in a low-resolution GCM. *Tellus*, **49A**, 200–227.

Taguchi, M. and D. L. Hartmann, 2006: Increased occurrence of stratospheric sudden warmings during El Niño as simulated by WACCM. *J. Climate*, **19**, 324–332.

Talagrand, O., 1991: The use of adjoint equations in numerical modeling of the atmospheric circulation. *Automatic Differentiation of Algorithms: Theory, Implementation, and Application*, Griewank, A. and G. Corlies, Eds., SIAM, 169–180.

Tanguay, M., P. Bartello, and P. Gauthier, 1995: Four-dimensional data assimilation with a wide range of scales. *Tellus Series A*, **47**, 974–997, doi:10.1034/j.1600-0870.1995.00204.x.

Thompson, D. W. J. and J. M. Wallace, 2000: Annular modes in the extratropical circulation. Part I: Month-to-month variability. *J. Climate*, **13**, 1000–1016.

Thompson, D. W. J., J. M. Wallace, and G. C. Hegerl, 2000: Annular modes in the extratropical circulation. Part II: Trends. *J. Climate*, **13**, 1018–1036.

Trenberth, K. E., 1981: Seasonal variations in global sea level pressure and the total mass of the atmosphere. *J. Geophys. Res.*, **86 (C6)**, 5238–5246.

Trenberth, K. E., J. M. Caron, D. P. Stepaniak, and S. Worley, 2002: Evolution of El Niño-Southern Oscillation and global atmospheric surface temperatures. *J. Geophys. Res.*, **107 (D7-8)**, AAC5.1–AAC5.19, doi:10.1029/2000JD000298.

Trenberth, K. E. and L. Smith, 2005: The mass of the atmosphere: A constraint on global analyses. *J. Climate*, **18**, 864–875, doi:10.1175/JCLI-3299.1.

Trevisan, A. and R. Legnani, 1995: Transient error growth and local predictability: A study in the Lorenz system. *Tellus*, **47A**, 103–117.

Tziperman, E. and Z. Sirkes, 1997: Using the adjoint method with the ocean component of coupled ocean-atmosphere models. *J. Meteorol. Soc. Jap.*, **75 (1B)**, 463–470.

Uppala, S., 2003: ERA40_ML00_MM (Monthly mean analyses on 60 model levels). Tech. rep., CERA-DB "ERA40_ML00_MM", URL http://cera-www.dkrz.de/WDCC/ui/Compact.jsp?acronym=ERA40_ML00_MM.

van Oldenborgh, G., G. Burgers, S. Venzke, C. Eckert, and R. Giering, 1999: Tracking down the delayed ENSO oscillator with an adjoint OGCM. *Mon. Wea. Rev.*, **127**, 1477–1495, URL http://www.knmi.nl/onderzk/oceano/publ/oldenbor/oldenbor01.html.

Wallace, J. M. and D. S. Gutzler, 1981: Teleconnections in the geopotential height field during the northern hemisphere winter. *Mon. Wea. Rev.*, **109 (4)**, 784–812.

Wallace, J. M., Y. Zhang, and L. Bajuk, 1996: Interpretation of decadal trends in Northern Hemisphere surface air temperature. *J. Climate*, **9**, 249–259.

Walter, K., U. Luksch, and K. Fraedrich, 2001: A response climatology of idealised midlatitude SST anomaly experiments with and without stormtrack. *J. Climate*, **14**, 467–484.

Wu, Q. and D. M. Straus, 2004: AO, COWL and observed climate trends. *J. Climate*, **17**, 2139–2156.

Wunsch, C., 1999: The interpretation of short climate records, with comments on the North Atlantic and Southern Oscillations. *Bull. Amer. Meteor. Soc.*, **80**, 245–255.

Xiao, Q., Z. Ma, W. Huang, X. Huang, D. Barker, Y. Kuo, and J. G. Michalakes, 2005a: Development of the WRF Tangent Linear and Adjoint Models:. Nonlinear and Linear Evolution of Initial Perturbations and. Adjoint Sensitivity Analysis at high-southern latitudes. *Proceedings of 6th WRF / 15th MM5 Users' Workshop*, National Center for Atmospheric Research, Boulder, California, USA, 4, URL http://www.mmm.ucar.edu/wrf/users/workshops/WS2005/abstracts/Session10/6-Xiao.pdf.

Xiao, Y., M. Xue, W. Martin, and J. Gao, 2005b: Development of Adjoint for a Complex Atmospheric Model, the ARPS, using TAF. Bücker et al. (2005), 263–272.

Zupanski, M., 1995: An iterative approximation to the sensitivity in calculus of variations. *Mon. Wea. Rev.*, **123**, 3590–3604.

*A note on the* doi: References for which a *digital object identifier* (doi) is given can be located online using the following URL: http://dx.doi.org/

# Index


**30**
adjoint, 102
opt. pert., 103
target, 99
**31**
adjoint, 102
opt. pert., 103
target, 99
**32**
adjoint, 102
opt. pert., 103
target, 99
**34**
target, 99
**38**
adjoint, 102
target, 99
**48**
adjoint, 102
target, 99
**51**
target, 99
**52**
adjoint, 102
opt. pert., 103
target, 99
**55**
adjoint, 102
target, 100
**56**
target, 100
**60**
adjoint, 102
**130**
ref. traj., 98
**138**
ref. traj., 98
**152**
ref. traj., 98
**155**
ref. traj., 98
**4000**, 103
**4030**
opt. pert., 103
**4031**
opt. pert., 103
**4032**
opt. pert., 103
**4052**
opt. pert., 103
**5430**
adjoint, 102
opt. pert., 103, 104
**5431**
adjoint, 102
opt. pert., 104
**5432**
adjoint, 102
opt. pert., 104
**5438**
adjoint, 102
**5452**
adjoint, 102
opt. pert., 104
**5455**
adjoint, 102
**9400**, 103
**9430**
opt. pert., 104
**9431**

opt. pert., 104
**9432**
opt. pert., 104
**9452**
opt. pert., 104

adfc2gp, 105
adfc2sp, 105, 106
adgp2fc, 105, 106
adjoint postprocessing, 102
adjoint preprocessing, 99
adoutgp
file, 102
subroutine, 102
adoutgp_$n$_$m$.srv, 102
adsp2fc, 105
adwritegp, 102
adwritegpgp, 102
anomaly, 99

breeding, 7

earth
angular velocity, 23
radius, 23
error
growth, 7
matrix, 8
Euler
time step, 104

fc2gp, 104
fc2sp, 104–106

gas constant
dry air, 23
gp2fc, 104

inverse, 9

l_trajectory_in_file, 98
l_trajectory_is_const, 98
Lyapunov exponent
local, 8

metric
matrix, 8

nadvance, 101
nafter_ad, 101
namelist, 98, 99, 102, 103
parameters
nrestart, 98
l_trajectory_in_file, 98
l_trajectory_is_const, 98
nadvance, 101
nafter_ad, 101
ncodes_in_adoutgp, 102
ncodes_in_g_ingp, 103
nkits, 104
nrun, 101
ntspd_t, 98
ncodes_in_adoutgp, 102
ncodes_in_g_ingp, 103
nkits, 104
normal modes, 7
normal-modes
finite time, 7
finite time adjoint, 7
nrestart, 98
nrun, 101
ntspd_tntspd_t, 98

perturbation, 99
fastest growing, 7
postprocessing
adjoint, 102
preprocessing
adjoint, 99
PUMA, 21
test of adj., 28

read_adj_target, 99
reference trajectory, 97

SERVICE
file format, 98
Singular Value Decomposition
of propagator, 8
sp2fc, 104, 106

SVD
    of propagator, 8

tangent-linear, 6
`TARGET.srv`, 99
time step
    semi implicit, 22
trajectory, 97
    constant, 98
    `namelist` parameters
      `l_trajectory_in_file`, 98
      `l_trajectory_is_const`, 98
      `nadvance`, 101
      `nafter_ad`, 101
      `nrun`, 101
`TRAJECTORY.srv`, 98

unitary, 8, 24